LRP 635/99 June 1999

Papers presented at the

26th EPS CONFERENCE ON CONTROLLED FUSION AND PLASMA PHYSICS

Maastricht, The Netherlands
June 14th - 18th, 1999

available in colour on the web at
crppwww.epfl.ch/crppabout/documents/conferences/EPS99

ISSN 0458-5895

LIST OF CONTENTS

Recent Results from the TCV Tokamak

R. A. Pitts*, S. Alberti, C. Angioni, K. Appert, R. Behn, P. Blanchard, P.Bosshard, R.Chavan,
S. Coda, B. P. Duval, D. Fasel, A. Favre, I. Furno, T. Goodman, P. Gorgerat,
M. Henderson, F. Hofmann, J.-P. Hogge, P.-F. Isoz, B. Joye, N. Kirneva[1], P. Lavanchy,
J. B. Lister, X. Llobet, J.-C. Magnin, P. Mandrin, A. Manini, B. Marletaz,
Ph. Marmillod, Y. Martin, J.-M. Mayor, J. Mlynar, J.-M. Moret, Ch. Nieswand,
P. Paris, A. Perez, Y. Peysson[2], A. Pietrzyk, A. Pochelon, G. Pochon,
F. Porcelli[3], A. Refke, H. Reimerdes, J. Rommers, O. Sauter, E. Scavino, A. Sushkov[1],
G. Tonetti, M. Q. Tran, F. Troyon, W. van Toledo, P. Vyas, H. Weisen

Centre de Recherches en Physique des Plasmas
Association EURATOM - Confédération Suisse
École Polytechnique Fédérale de Lausanne, CH-1015 Lausanne, Switzerland
**Presenting author, [1]Institute of Nuclear Fusion, RRC Kurchatov, 123 182 Moscow, Russia*
[2]CEA Cadarache, F-13108 Saint-Paul-lez-Durance, France
[3]INFMDE, Politecnico di Torino, I-10129 Torino, Italy,

INTRODUCTION The TCV tokamak (B_T<1.5 T, R≈0.89 m, a<0.25 m, I_p<1.2 MA) has produced a wide variety of plasma configurations, both limited and diverted, with elongations, κ in the range 0.9 → 2.58 and triangularities, δ from -0.7 → 1.0. A few recently produced plasma equilibria are shown in Fig.1. Three gyrotrons at 82.7 GHz and 0.5 MW each are presently installed and have been used in the second harmonic X-mode (X2) for the ECH and ECCD experiments described in this paper. These sources are capable of a pulse length of 2 s, with the microwaves being delivered to the plasma by poloidally and toroidally steerable mirror systems for flexible power deposition and current drive. The implementation of another six gyrotrons (a further three for X2 and three for X3 at 118 GHz) is in progress. The in-vessel graphite armour has recently been upgraded for high power ECH experiments, with new tiles on the central column and low-field-side wall of the vacuum vessel providing almost 90% internal surface coverage.

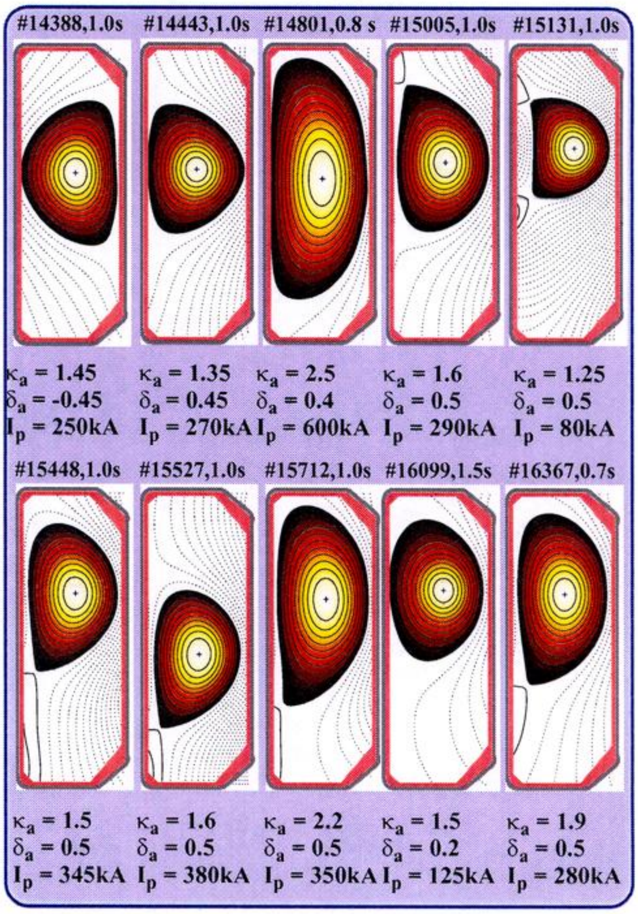

Figure 1: *Illustrating the flexibility of TCV for plasma shape experiments. The equilibria above are representative of the range of shapes used in the experiments described in this paper.*

TOKAMAK OPERATION AT HIGH ELONGATION Elongations up to 2.2 in single null (SN) divertor configurations and up to 2.58 in limited plasmas have been obtained on TCV. The highest elongations (κ>2.2) are only possible for q_{95}<3 and require the use of fast feedback coils inside the vessel. They correspond to stability margins $m_s \geq 0.08$ (computed using a variant of the rigid current distribution model) and growth rates up to 2000 s^{-1}[1]. Crossing q_{95}=3 during discharge formation is not observed to be associated with increased disruptivity provided that a modest

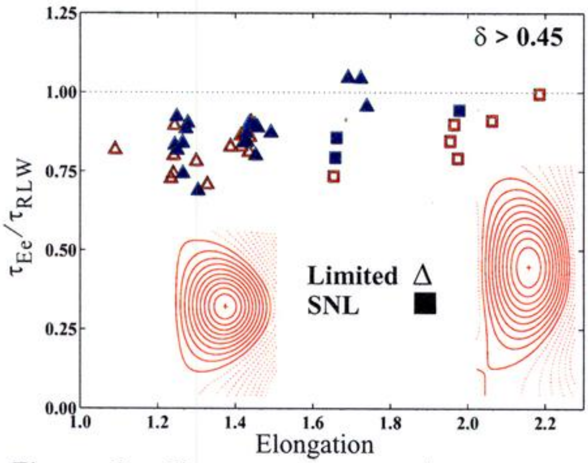

Figure 2: *Electron energy confinement time normalized to RLW scaling for highly elongated SNL discharges compared with limited equilibria of similar triangularity (ohmic L-mode only). Open symbols, $q_{95}>3$, closed symbols, $q_{95}<3$.*

amount of shaping is already present (typically $\kappa=1.4, \delta=0.3$ [2]).

A series of SN diverted discharges with $1.6 \leq \kappa \leq 2.2$, $2.5 < q_{95} < 3.5$ and $\delta > 0.45$ has been developed with the goal of assessing their confinement properties. For ohmic heating alone and sufficiently high values of plasma current and density, these discharges undergo H-mode transitions [3]. The latter are invariably followed by ELM-free H-modes (especially for favourable ion ∇B drift direction), rapidly terminated by a disruption. Confinement data in stationary conditions are therefore available only in ohmic L-mode, as shown for the electrons in Fig. 2. In comparison with limited discharges, there are clearly no major differences in confinement time at high elongation and low q_{95} in SN equlibria.

DIVERTOR DETACHMENT Despite its small size, the possibility for plasma shape variation in TCV permits the creation of magnetic equilibria allowing the detached divertor state to be accessed, even in completely open geometries [4]. Long midplane to target connection lengths, L_c, can be generated in SN configurations with the interesting feature that most of L_c appears in the poloidal distance between X-point and target and not between midplane and X-point as in more conventional geometries. Two examples are shown in Fig. 3 where, for fixed plasma current, the X-point height is varied for fixed main plasma parameters, reducing L_c near the separatrix from 20 m to 13 m, of which only ≈5 m is above the X-point. Detachment at the outer target is clearly seen in both cases (reduction of ion current, j_{sat}) with simultaneous increase in divertor D_α intensity. For higher L_c, detachment occurs at lower densities and the absolute particle flux is lower than for shorter connection length. In each case, the electron temperature in the divertor reaches low values (≈5 eV) at detachment and, at high L_c, the divertor is already in the high recycling regime, even when $\bar{n}_e$ is low at the start of the discharge.

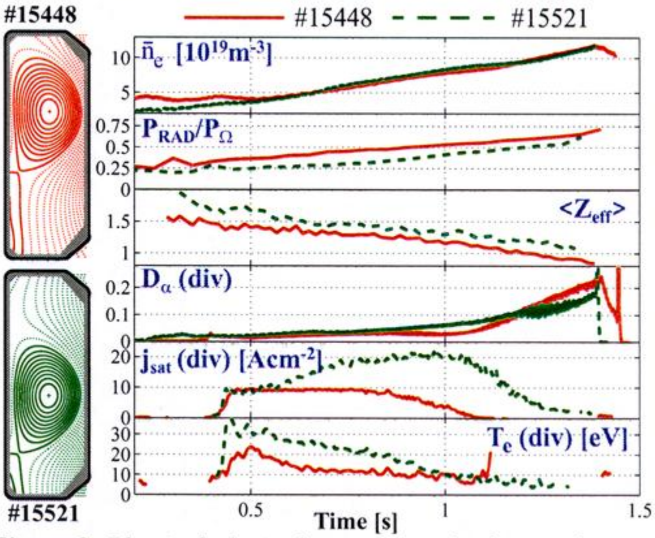

Figure 3: *Identical ohmic density ramp discharges for two equilibria with varying X-point height and thus connection length. Both have radiation fractions approaching 75% and low Z_{eff} at the highest densities. I_p = 340 kA in each case.*

H-MODE TRANSITIONS WITH ECRH Below a density of $\bar{n}_e = 3.5\times10^{19}$ m^{-3} for the ion ∇B drift direction towards the X-point and elongation in the range $1.5<\kappa\leq2$, ohmic H-mode transitions are not obtained in TCV. Recent experiments [3] using ECRH (for which cut-off occurs at a local density of $\bar{n}_e = 4.3\times10^{19}$ m^{-3}) have shown that this threshold density is significantly reduced in the presence of heating. Figure 4 shows that transitions do not occur for $\bar{n}_e < 2.5\times10^{19}$ m^{-3} with the 1.5 MW of power currently available. No systematic dependence of threshold power, P_{thr}, on elongation has been observed in these preliminary experiments. In ECH plasmas, P_{thr} increases sharply as the density is reduced, in contrast with the scaling ($P_{thr} \propto \bar{n}_e^{0.7}$ approximately [5]) generally observed with heating systems other than ECRH. The decoupling of the ion population from the electrons at low density and high electron temperature may be the cause of this behaviour.

ECCD EXPERIMENTS The ability to change both the poloidal (real time) and toroidal (between discharges) angles at which ECH power is injected permits a wide variety of experiments aimed at investigating both pure ECRH and ECCD. In one such study, the toroidal launching angle, φ, has been varied from -35° to +35° with a total of 1.5 MW of power being injected near the plasma center (the 0° case corresponding to pure ECH). Figure 5 shows the φ dependence of the fast-electron bremsstrahlung emission from the plasma centre in the photon energy range $40<E_{ph}<50$ keV measured using a multichannel hard X-ray camera on loan from the Tore Supra tokamak [6]. For $\varphi \approx 0°$, there is no measurable suprathermal population and the photon energy spectra are consistent with a Maxwellian distribution at a temperature close to that measured by Thomson scattering. During ECCD, photon count rates increase with increasing φ in both co- and counter-ECCD directions. The highest values of T_e ever measured on TCV ($T_{e0}\approx 11$ keV) [7] were obtained with counter-ECCD at φ = -7° and -14°, for which electron energy confinement times up to twice RLW are obtained, indicating that improved confinement related to shear modification is occurring in the plasma centre under these conditions.

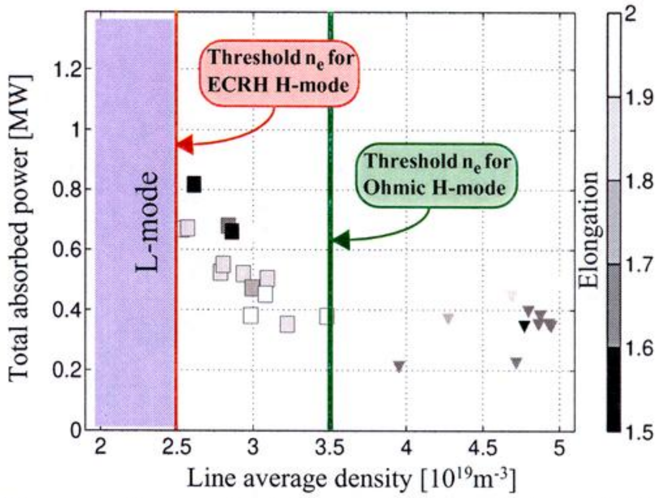

***Figure 4**: Power at the L-H transition for ohmic and ECR heated SN diverted plasmas of varying elongation and the ion ∇B drift towards the X-point.* ▼: *Ω–H transitions,* ■: *L-H transitions*

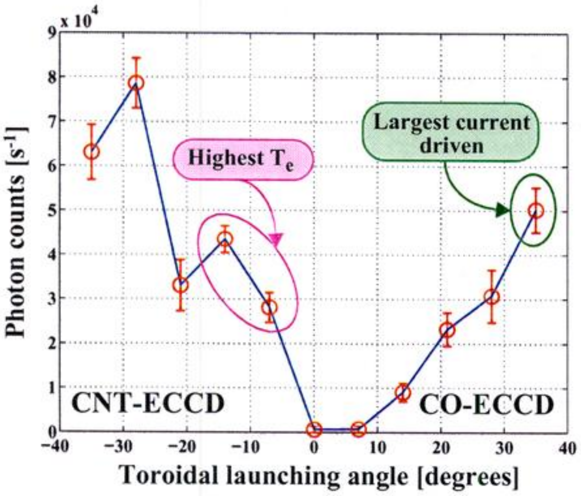

***Figure 5:** Toroidal angle variation of the hard X-ray emission from the plasma centre in the energy range 40-50 keV during a shot-to-shot angle scan at constant I_p = 170 kA, κ = 1.3, δ = 0.3 and n_{e0}=2-2.5x10^{19} m^{-3}.*

As also shown in Fig. 5, the highest current drive efficiencies have been measured for φ = +35°. Under these conditions, stationary, full current replacement has been achieved, sustaining nearly 125 kA for 1.9 s, limited only by the gyrotron pulse length [8]. Figure 6 shows how the ohmic transformer current reaches a constant value almost immediately after switch-on of 1.5 MW of co-ECCD yielding a current drive efficiency of $\gamma_{CD20} \approx 0.01$ AW^{-1} m^{-2} for $n_{e0} = 1.5\text{x}10^{19}$ m^{-3}, T_{e0} = 3.5 keV and R = 0.88 m. Although full non-inductive current drive occurs rapidly after the application of heating, the time variation of the plasma inductance and elongation included in Fig. 6 demonstrates that the current profile requires about 500 ms to relax. These stationary conditions are obtained only if the power deposition of the three available sources is distributed carefully over the minor radius, leading to broader current and pressure profiles and avoiding the generation of MHD modes. The latter are at the origin of disruptions in alternative scenarios in which on-axis co-ECCD of all three sources produces higher current drive efficiencies at the expense of very peaked profiles and susbsequent rapid loss of confinement. A number of experiments have also been performed demonstrating that even in

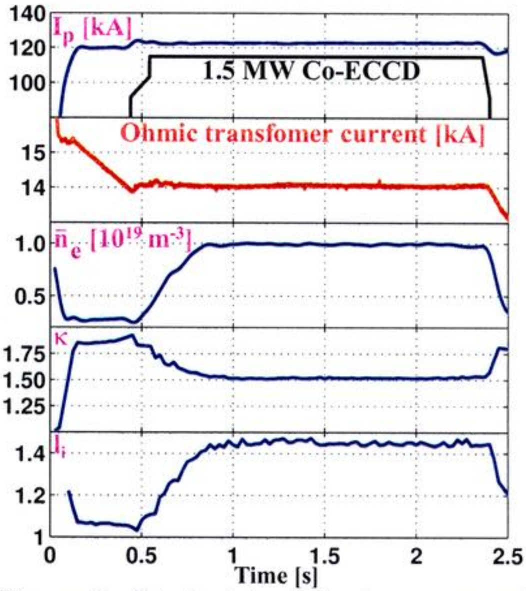

Figure 6: *Steady-state, full plasma current replacement for 1.9 s with 1.5 MW of co-ECCD distributed over the minor radius in a limited plasma with $\delta=0.3$ and I_p = 125 kA.*

the case of pure ECH, sweeping the power deposition location off-axis can have considerable effect on MHD activity, notably sawtooth periods and amplitudes [9]. This is a result of local heat deposition and finite current drive components due to a non-zero projection of the parallel wave vector onto the local field when moving off-axis. The degree to which sawteeth behaviour is modified depends on the direction of this current drive, itself dependent on the toroidal field direction and deposition location (above or below the magnetic axis). With increasing central ECH power deposition, positive triangularity and low elongation have a stabilising effect on sawteeth leading to longer sawtooth periods and higher crash amplitudes, in qualitative agreement with the effect of triangularity on Mercier and resistive MHD stability [10]. High κ or negative δ would therefore appear to be attractive for the reduction of heat pulses and seed islands which can follow high power sawtooth crashes. There is also evidence for a marginal increase in electron energy confinement time with negative triangularity at absorbed ECH powers of up to 1.4 MW [10].

CONCLUSIONS The traditional capacity of TCV for creation of a wide range of plasma shapes has led to a large database of equilibria showing that, for stability margins of current interest, there should be no difficulty with plasma control using external coils only. In addition, at least in L-mode, SN discharges with $\kappa>2$ and low q_{95} appear to have similar confinement to limited equilibria at lower elongation. Divertor detachment is now regularly obtained in TCV and its characteristics are being studied, in particular with respect to variable and extremely open magnetic geometries. With the addition of the first third of an eventual 4.5 MW of ECH, important new ECRH and ECCD studies are now being pursued. The high degree of flexibility in toroidal and poloidal launching position and high power density has revealed interesting features in the plasma response to off-axis deposition, yielded new results regarding the characteristics of ECCD at high toroidal angles and produced the highest electron temperatures so far observed in TCV ($T_e > 10$ keV). Steady-state, full current replacement of 125 kA has been demonstrated for 1.9 s using co-ECCD distributed over the minor radius. This corresponds to more than 400 energy confinement times and 4 current diffusion times.

ACKNOWLEDGEMENT

This work was partly supported by the Swiss National Science Foundation.

REFERENCES

[1] J. B. Lister et al., this conference
[2] Y. Martin et al., Proc. Joint ICPP 1998 & 25th EPS Conf. Contr. Fusion and Plasma Physics, Prague, Czech Republic, ECA Vol **22C** (1998) 695
[3] Y. Martin et al., this conference
[4] R. A. Pitts et al., this conference
[5] K. Thomsen et al., IAEA 1998, IAEA-F1-CN-69/ITERP1/07
[6] S. Coda et al., this conference
[7] R. Behn et al., this conference
[8] O Sauter et al., this conference
[9] T. Goodman et al., this conference
[10] A. Pochelon et al., this conference

Evolution of T_e and n_e Profiles during ECH and ECCD in TCV

R. Behn, Z.A. Pietrzyk, J.R. Rommers, C. Angioni, S. Coda, I. Furno,
T.P. Goodman, M.A. Henderson, J.-Ph. Hogge, Y. Martin,
Ch. Nieswand, A. Pochelon, H. Weisen, F. Porcelli[1], E. Rossi[1]
Centre de Recherches en Physique des Plasmas
Association EURATOM - Confédération Suisse
École Polytechnique Fédérale de Lausanne, CH-1015 Lausanne, Switzerland
[1]*Istituto Nazionale Fisica della Materia & Dipartimento di Energetica, Politecnico di Torino, I-10129, Torino, Italy*

INTRODUCTION

The use of electron cyclotron waves for plasma heating (ECH) and non-inductive current drive (ECCD) has the advantage of local power deposition determined by the location of a resonance layer in the plasma and the orientation of the microwave beams. Localized deposition of heating power can be used as a means to modify the shape of temperature and pressure profiles and their gradients with substantial consequences on the current distribution as well as on heat and particle transport. Local non-inductive generation of current provides a tool to optimize the shape of the q-profile with the aim of reaching regimes of improved confinement.

Depending on the exact location of the power deposition with respect to the rational q-surfaces of the plasma (in particular q=1), different types of sawtooth oscillations have been observed on the signals from soft X-ray emission. These lead to transient perturbations in the millisecond time scale of the electron temperature (T_e) and density (n_e) profiles. In the following, measurements by Thomson scattering are used to investigate these characteristic changes in the spatial and temporal variation of T_e and n_e during different scenarios of EC-heating and EC-current drive.

THE THOMSON SCATTERING SYSTEM ON TCV

Using a laser beam, which passes the TCV vessel in vertical direction at the position of its major radius, and 35 viewing chords distributed on 3 horizontal ports, the system provides measurements of T_e and n_e profiles with a spatial resolution of about 40mm along the laser beam and 3mm in toroidal and radial directions. Recently the system has been upgraded and now comprises 3 high-power Nd:YAG lasers. By combining the beams of these lasers in a fan and focusing them to a common spot inside the plasma, the system permits us to measure profiles at sampling intervals which can be varied via delayed triggering of the individual lasers. The minimum time interval between laser pulses is 0.4ms, limited by the data acquisition system.

T_e AND n_e PROFILES DURING ECH AND ECCD

Apart from sweeps in the direction of the microwave beams or variations of the toroidal magnetic field strength, the location of power deposition in TCV can also be changed by moving the plasma in the vertical direction during a shot. This method has been used in the cases presented here, in order to investigate the effects of central or off-axis power deposition. The parameters of the plasma and the heating system were the following :

I_p=170kA, line-integrated $n_e \geq 1.10^{19}m^{-2}$, q_{edge}= 4.4, $\kappa = 1.25$, P_{EC} = 1.5 MW (3 beams), 82.7GHz (second harmonic), X-mode.

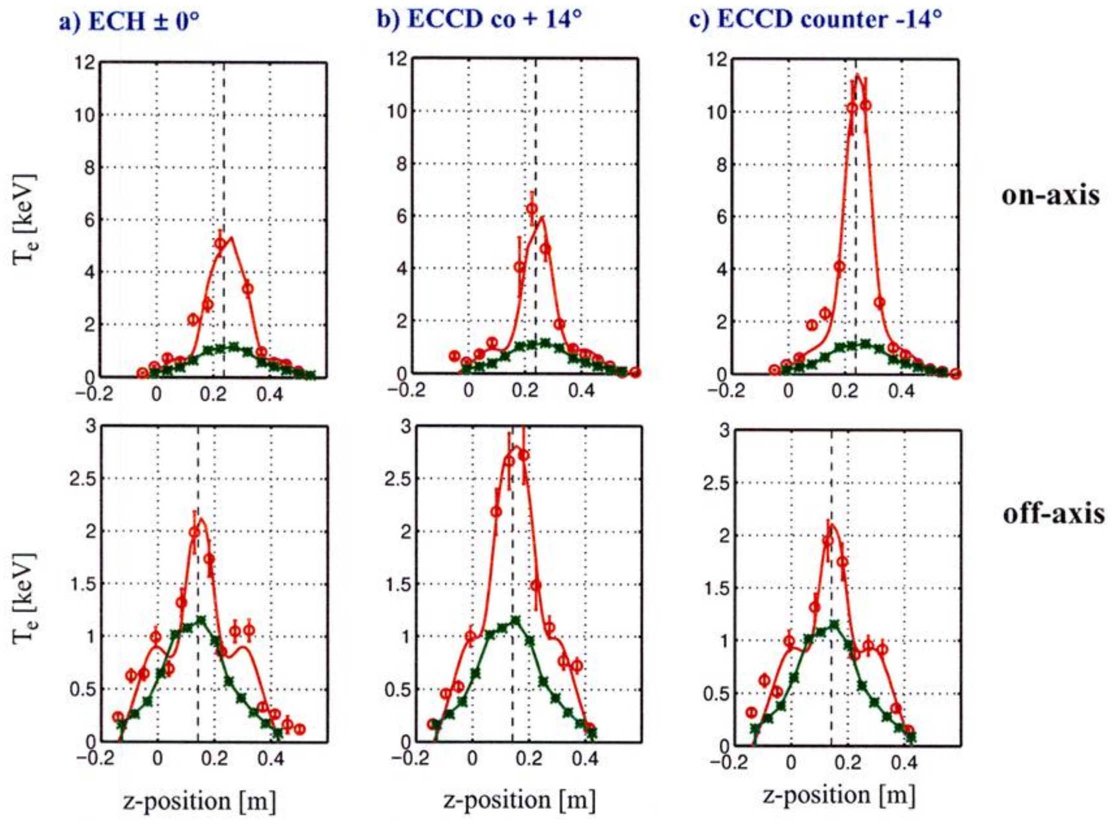

Fig. 1 *T_e -profiles measured by Thomson scattering for different conditions of EC-heating and -current drive total injected power using 3 beams : P_{inj} =1.5MW*
*a) **ECH** (inject. at 0°); b) **co-ECCD** (inject. at +14°); c) **cntr-ECCD** (inject. at -14°)*
top row : power deposition on-axis; bottom row : off-axis (near q=1 surface).
The fitted curves (in red) assume constant T_e on flux surfaces.
*The T_e -profiles of an ohmically heated plasma with the same parameters are given for reference (curves in green, labeled by *). The dashed vertical line marks the z-position of the magnetic axis.*

The power deposition in the centre and near the q=1 surface (off-axis), respectively, is confirmed by calculations using the TORAY code, which predicts full absorption in both cases.

In the case of perpendicalur injection (**EC**, fig. 1a), the T_e and n_e profiles measured by Thomson scattering at different time steps during the two phases show a clear trend : high central temperatures and peaked profiles for central power deposition and a significant broadening of the profiles in the off-axis phase. This can be quantified by a variation of the profile peaking factor (defined as $T_e(0)$ / $T_e(avg)$), which drops from about 6 to values below 4. The region of central heating is delimited by sharp gradients in the vicinity of the location of the q=1 surface. During the phase with off-axis deposition local minima and side lobes appear on the profiles. These structures vary with time and seem to be located close to the q=1 surface, which suggests the presence of islands. Compared to the very pronounced changes of the T_e profiles, there is only little change in the n_e profiles, which remain fairly flat (peaking factor around 1.7).

In a similar scenario and starting from the same target plasma, two cases of non-inductive current drive (**ECCD**) have been investigated (figs 1b,c). In the first case, the toroidal angle (14°) was adjusted to produce current drive in the co-direction, whereas the second case refers to a counter-orientation.

For co-injection aiming at the plasma centre, there still is significant heating and peaked T_e-profiles are observed with the central value reaching that of the pure heating case ($T_e(0)$> 5keV, see fig. 1b). The phase with off-axis deposition is again characterized by lower central temperatures and smaller peaking factors. The density profiles do not show any significant change (peaking factors varying around 1.5).

It is regularly observed on TCV that launching conditions with counter injection lead to the highest central electron temperatures. For the case shown in fig.1c, the central T_e reaches 10 to 12keV during the phase with on-axis power deposition. This results in extremly peaked T_e-profiles and an electron energy content close to 6kJ . Again, during the phase with off-axis deposition the central temperature is lower and hardly exceeds the ohmic reference value by more than a factor of 2. During this phase slightly hollow T_e-profiles have also been observed. The behaviour of the electron density is similar to the case with co-ECCD.

Table 1 summarizes the results of these measurements.

Table 1:

TCV-shot	type	**on axis**			**off axis**		
#		$T_e(0)$ [keV]	T_e-prof. peaking	W_e [kJ]	$T_e(0)$ [keV]	T_e-prof. peaking	W_e [kJ]
15'853	ECH, ± 0°	5 - 6	6 -7	4.5 - 5	2.2 - 2.7	3 - 4	3.0 - 3.2
15'854	ECCD-co, +14°	5 - 6	7 - 8	4 - 5	2 - 3	3 - 4	3 - 4
15'855	ECCD-cntr, -14°	8 - 12	9 - 11	5 - 6.4	2 - 3	3 - 3.5	3.5 - 4.5

INFLUENCE OF SAWTOOTHING ACTIVITIES ON T_e AND n_e PROFILES

Under conditions of local deposition of auxiliary heating power, which is typical for EC-heating and EC-current drive experiments, the appearance of the sawtooth oscillations changes significantly [1]. Apart from the ordinary triangular shaped sawteeth the oscillations can take the form of saturated or inverted sawteeth or features with a more sinusoidal variation interrupted by a short crash (so-called "humpbacks").

Although observation of the soft X-ray emissivity provides essential information for investigations of these phenomena, measurements based on other diagnostic methods are required for interpretation. Thomson scattering offers the advantage of local measurements and a clear separation of the contributions from different plasma parameters (T_e, n_e, etc). Until recently, the limitations in sampling rate usually did not permit us to follow the evolution on the time scale of a sawtooth period. Valuable information could still be obtained in quasi-stationary cases where repetitive measurements at a lower frequency produced samples at different phases in the sawtooth cycle.

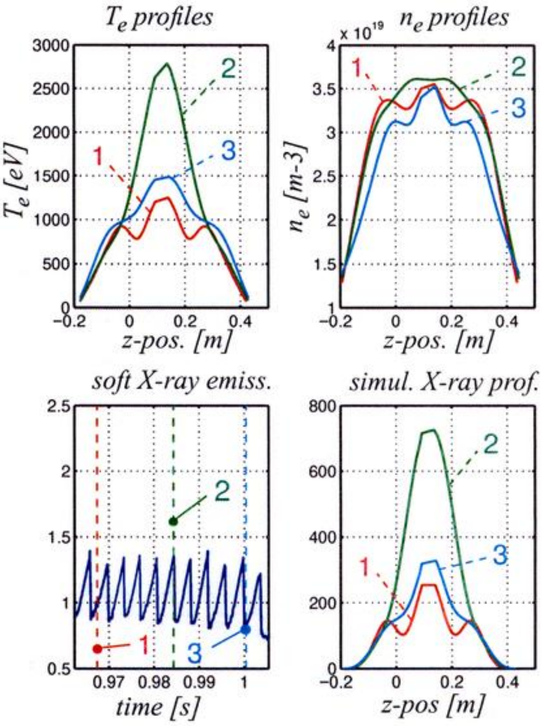

Fig. 2
Top: measured profiles of T_e and n_e at different times during a sawtooth cycle.
Bottom : recorded soft X-ray emission and simulated emissivity profile (using T_e and n_e data as input).

The data of fig.2 refer to an EC-heated plasma with power deposition inside the q=1 surface and a prolonged phase of large regular sawteeth. The crash in the soft X-ray emissivity is clearly identified as a collapse of the central part of the T_e profile, which in this case reaches an amplitude of more than 1keV. Variations on the n_e profile are small and within the uncertainty of the measurement. For comparison with the soft X-ray emissivity, measured approximately along the same chord, expected emissivity profiles have been calculated using T_e and n_e data as input (fig.2 bottom right). Integration of these profiles along z produces a data set, which has been superposed on the signal of the measured soft X-ray emission (labeled 1,2,3) to compare the tendency of the temporal variation.

Due to the recent upgrade of the Thomson scattering system, it is now possible to take a series of measurements within a single sawtooth cycle. Fig. 3 shows a set of profiles measured within a 2ms time interval before and after a sawtooth crash. This type of sawteeth has been observed for EC power deposition close to the q=1 surface. They are characterized by an unusually large variation of the central density and fairly rapid reheating after the crash. At the start of the reheating phase hollow profiles have been measured by Thomson scattering and soft X-ray tomography.

During "humpback"-type relaxation oscillations, the short crash in the soft X-ray emissivity is followed by a rapid recovery (see fig.4). The measurement closest to the crash reveals a clear drop of the central T_e, whereas the density profile remains almost unaffected. In this particular case, the rise in the soft X-ray emissivity after the crash is larger than would be expected from the measured increase in temperature. However, the T_e profiles during "humpbacks" show fluctuations which make it difficult to establish a clear trend.

This work was partly supported by the Swiss National Science Foundation.

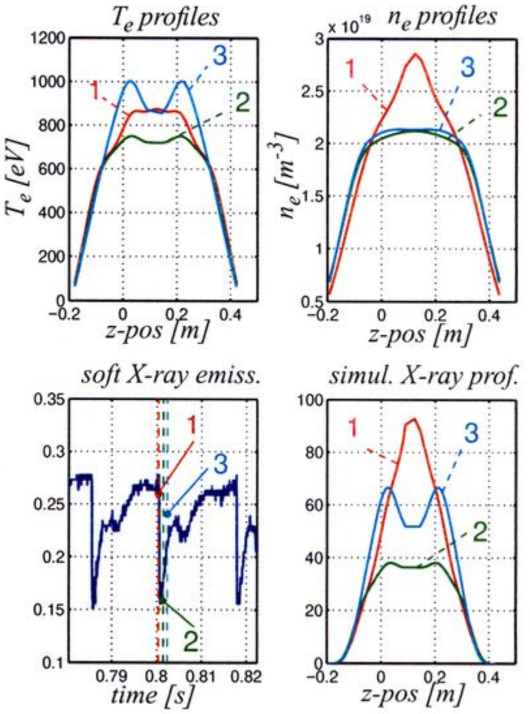

Fig 3
Profile evolution during the cycle of a "partially saturated sawtooth"

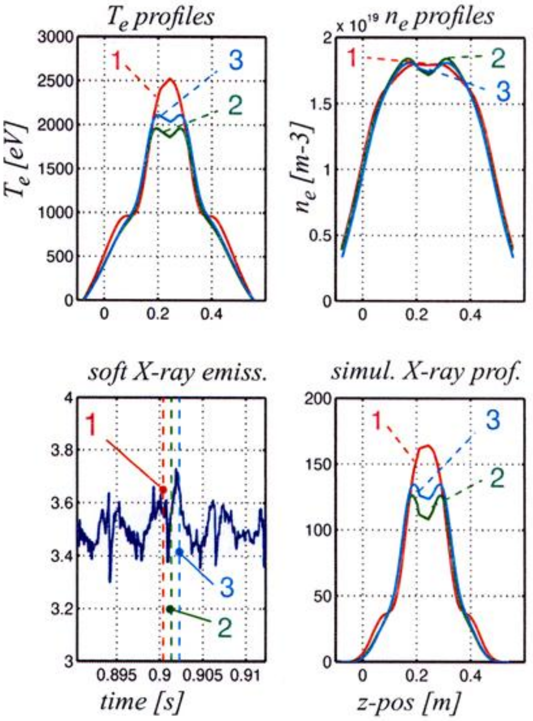

Fig 4
Profile evolution during the cycle of a "humpback"

REFERENCE

[1] *Z.A. Pietrzyk et al.*
*Nucl.Fusion **39**(5), p.587ff, 1999*

Measurements of Hard X–Ray Emission Profiles in the TCV Tokamak during Electron Cyclotron Heating and Current Drive

S. Coda, Y. Peysson,† L. Delpech,† T.P. Goodman,
M.A. Henderson, J.-P. Hogge, X. Llobet, B. Marlétaz,
Z.A. Pietrzyk, A. Pochelon, G. Pochon, O. Sauter, H. Weisen.

Centre de Recherches en Physique des Plasmas,
Association EURATOM – Confédération Suisse,
Ecole Polytechnique Fédérale de Lausanne, CH–1015 Lausanne, Switzerland

†Département de Recherches sur la Fusion Contrôlée, Association EURATOM–CEA,
CEA/Cadarache, 13108 Saint Paul-lez-Durance Cédex, France

1. Introduction

A multichannel hard X–ray (HXR) diagnostic system developed for the Tore Supra tokamak [1] has been employed on the TCV tokamak with the aim of characterising the spectral and spatial distribution of fast-electron bremsstrahlung emission during electron cyclotron heating (ECH) and current drive (ECCD). The system consists of a vertically viewing pinhole camera equipped with an array of CdTe detectors. CdTe technology was chosen for this system in order to satisfy the combined requirements of good temporal and spatial resolution, of efficient γ–ray rejection and of compactness. On TCV, 14 partially overlapped viewing chords span the entire outer minor radius of the plasma, with a radial resolution of $\sim$2 cm on the midplane (Fig. 1). The intrinsic energy resolution is $\sim$5–7 keV. After amplification, each signal is distributed to 8 discriminator-counter chains, generating spectra in the range 10–150 keV. Count rates up to 1.5×10^5 s^{-1} can be detected before the onset of pileup. The time resolution, determined by the requirement of a relative statistical noise $<$10%, is in the order of 1–5 ms.

Fig. 1 *Geometry of hard X-ray camera viewing chords for a typical EC-heated TCV plasma (R = 88 cm, a = 23 cm). The chords are partially overlapped.*

The ECH and ECCD experiments described in this paper have been carried out with up to three 0.5 MW gyrotrons, operating in X-mode at the second harmonic (82.7 GHz) [2]. The launching mirrors can be independently rotated in both the poloidal and the toroidal direction, providing great flexibility in the choice of heating locations and parallel wave numbers. The HXR camera constitutes a crucial tool for investigating the location of the power deposition and the distribution and dynamics of suprathermal electrons. Initial results are presented in this paper.

2. Suprathermal electron population during ECH and ECCD

The parallel wave number of the electron cyclotron (EC) wave was scanned in a set of similar discharges by varying the toroidal launching angle Φ from -35° to +35° (this angle is defined at the launcher, the 0° case corresponding to pure ECH). In these discharges the plasma current was 170 kA, the toroidal field 1.4 T, the peak density 2–2.5×10^{13} cm^{-3}, the plasma elongation 1.3 and the triangularity +0.3. A total power of 1.5 MW was injected near the plasma center.

The intensity of hard X-ray bremsstrahlung emission increases with $|\Phi|$, in both the co- and counter-ECCD directions (Fig. 2). In the co-ECCD case the current-drive efficiency has also been found to increase with Φ, and the largest non-inductive currents in TCV to date have been generated at the maximum toroidal angle explored in this scan (35°). This is somewhat in contrast with code predictions, which have generally placed the optimum angle between 25 and 30° [3]. This scan has proven fruitful also in allowing us to identify a range of angles (5–15°) in the counter-ECCD direction in which very high central electron temperatures (up to ~10 keV) are obtained.

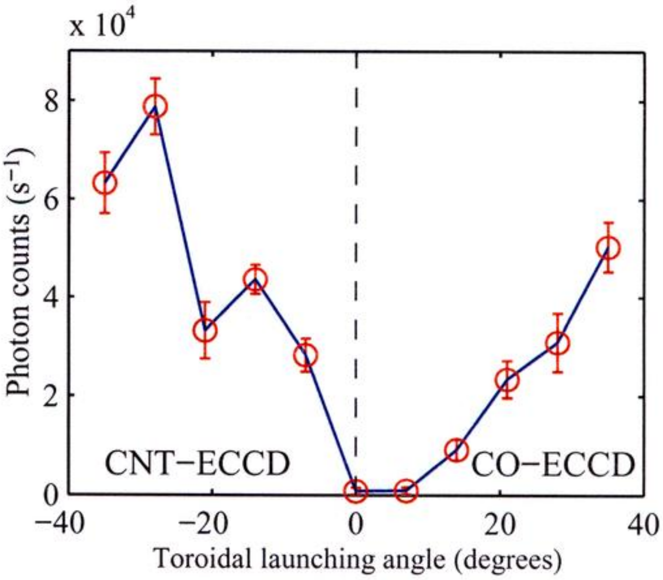

Fig. 2 *Hard X-ray emission from the plasma center in the range 40–50 keV as a function of the toroidal launching angle, at constant current, density and plasma shape (central heating, 1.5 MW).*

In the pure ECH case the shape of the measured spectrum is consistent with the emission from a Maxwellian plasma of temperature equal to that measured by the Thomson scattering diagnostic; this comparison can be quantified by calculating an effective photon temperature through an exponential fit to the spectrum: an example is shown in Fig. 3. Rough analytical estimates of the expected absolute photon emission from a Maxwellian plasma are also in good agreement with the measurement.

In the ECCD cases, not only is the intensity considerably higher than in the ECH case at all energies, but the effective photon temperature is typically in the range from 20 to 60 keV (see Fig. 4), clearly revealing the presence of a suprathermal tail in the electron velocity distribution.

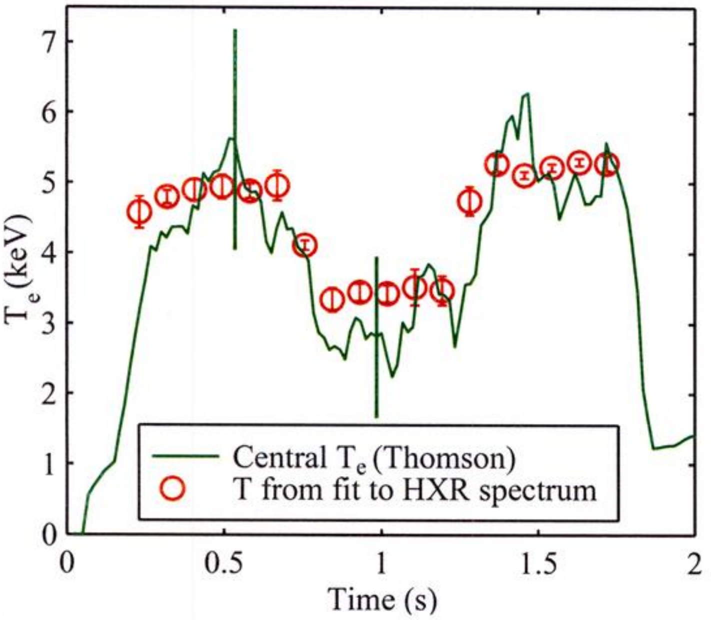

Fig. 3 *Comparison between central electron temperature measured by Thomson scattering (solid line) and effective temperature obtained by a 3-point exponential fit to the hard X-ray spectrum from the plasma center (circles), with 1.5 MW of EC heating (off-axis in the middle part of the discharge, on-axis elsewhere).*

The dissimilarity between the ECH and ECCD cases, further seen in the integrated spatial profiles in Fig. 5, is in qualitative agreement with numerical simulations carried out with the CQL3D Fokker–Planck code [4]. In the pure heating case the effect of the EC wave is to increase the temperature of the bulk plasma without appreciable modification of the shape of the distribution function, owing to rapid thermalisation of the heated electrons. By contrast, the preferential heating of suprathermal electrons on the low-field side of the resonance in the ECCD case permits the generation and sustainment of a non-Maxwellian tail, which carries the non-inductive current.

3. Investigation of fast electron dynamics

Studies of fast electron dynamics in large tokamaks have generally indicated [5,6] that collisional slowing-down (momentum destruction and pitch-angle scattering) is the dominant relaxation mechanism, whereas radial diffusion plays only a secondary role.

In the TCV tokamak the characteristic times for these phenomena are comparable with the temporal resolution of the HXR camera. In order to study the response and relaxation phenomena in detail, we have carried out an experiment with modulated EC power. Under stable plasma conditions, the excellent repeatability and localisation of EC-wave–plasma coupling have allowed a substantial enhancement of the effective time resolution (down to ~300 μs) through summation of the photon counts over multiple modulation periods. The modulation period must of course be a multiple of the sampling interval for the HXR diagnostic. In the example shown in Fig. 6, 1 MW of ECCD power was modulated at 100% with a period of 9.36 ms; the HXR sampling time was 585 μs and the counts were then summed over 10 periods. The resulting signal is shown in Fig. 6 for a central chord and four different energy levels. The relaxation dynamics at turn-on and turn-off are clearly adequately resolved.

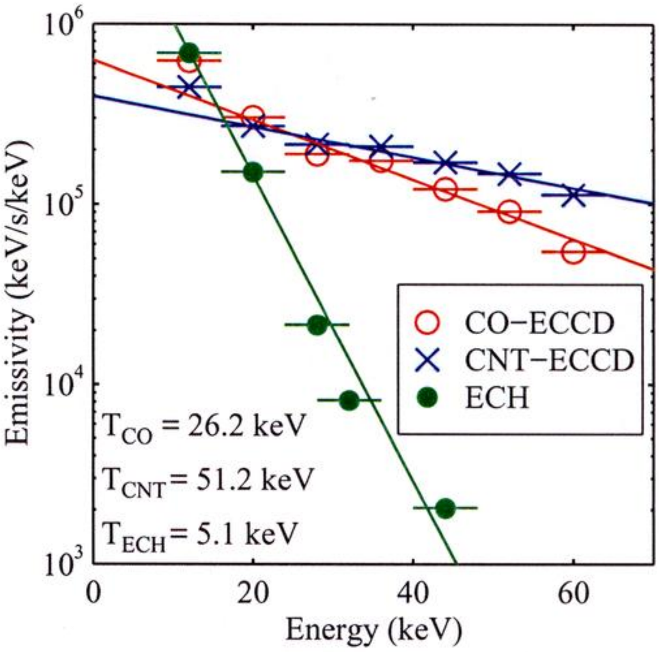

Fig. 4 *Central hard X-ray emissivity for similar shots with co-ECCD (Φ = 21°), counter-ECCD (Φ = 21°), and pure ECH, respectively (central heating, 1.5 MW). In the exponential fits in the ECCD cases the lowest energy point was ignored, as it is influenced by the bulk Maxwellian distribution.*

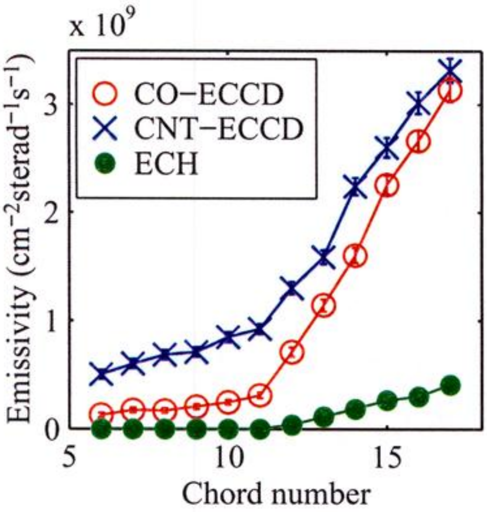

Fig. 5 *Spatial profiles of line-integrated hard X-ray emissivity (24–32 keV), for the same conditions as in Fig. 4. The chords are numbered from the plasma edge to the center, with a radial separation of ~2 cm.*

To extract the essential physics of the suprathermal electron dynamics, we have employed a simple model consisting of a source (the localised

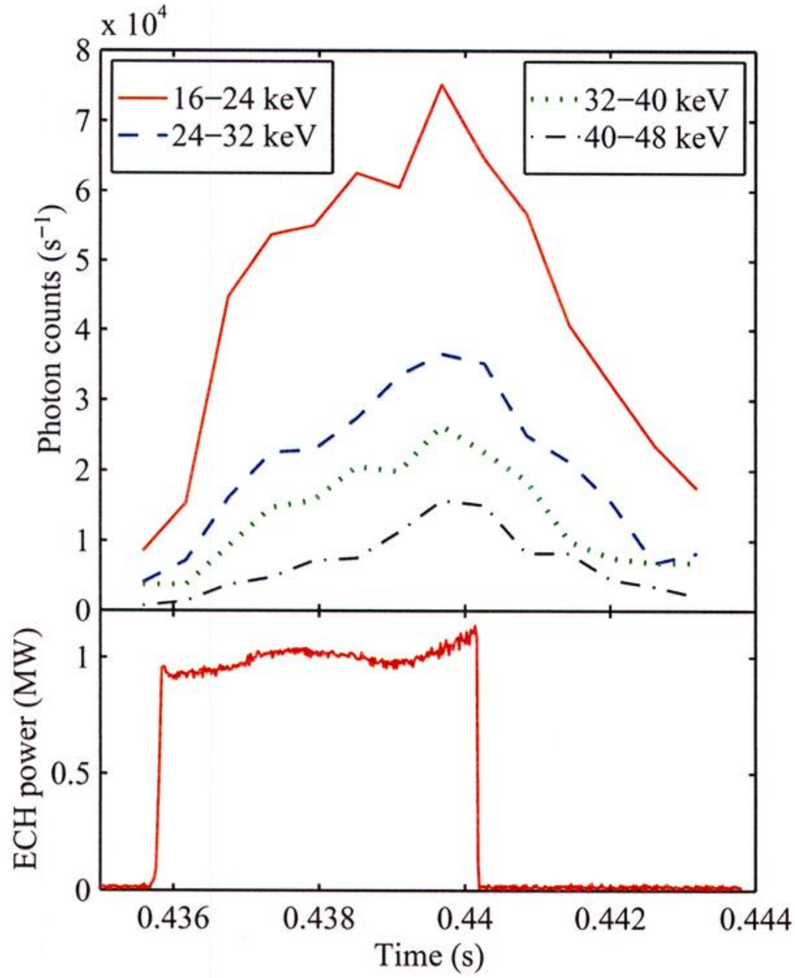

Fig. 6 Hard X-ray emission from the plasma center, for four different energies, and EC power vs. time (central co-ECCD, $\Phi = 21°$). The photon counts are summed over 10 successive EC modulation periods.

EC power), a Krook collision operator, and a radial diffusivity. The characteristic times are varied to simulate the time history of the experimental HXR emissivity. In a preliminary comparison, we have found that satisfactory agreement is obtained only when the collisional term is dominant, with characteristic relaxation times of the order of 1–3 ms: these values are consistent with the collisional slowing-down time for the energy range under consideration.

Under these conditions, the spatial distribution of the HXR emissivity can be taken as a good measure of the EC power deposition profile. More detailed studies are currently in progress. Comparisons between the experimental local (Abel-inverted) emissivity profile and the power deposition profile calculated by ray tracing are also underway.

Acknowledgments

We wish to thank the CEA for the loan of the HXR camera and associated electronics to the CRPP. We are also grateful to the entire TCV team for their invaluable role in executing the experiments described in this paper. This research was partly supported by the Swiss National Science Foundation.

References

[1] Y. Peysson and R. Arslanbekov, Nucl. Instr. and Methods, **380** (1996) 423.
[2] T.P. Goodman, S. Alberti, M.A. Henderson, A. Pochelon, M.Q. Tran, Proc. 19th SOFT, Lisbon (1996), 565.
[3] A. Pochelon, S. Alberti, M. Bourqui, et al., Bull. Am. Phys. Soc. **41** (1996) 1514.
[4] R.W. Harvey and M.G. McCoy, in Proc. IAEA TCM/Advances in Simulation and Modeling in Thermonuclear Plasmas, Montreal (1992).
[5] Y. Peysson, Plasma Phys. Control. Fusion, **35** (1993) B253.
[6] S.E. Jones, J. Kesner, S. Luckhardt, et al., Phys. Plasmas, **2** (1995) 1548.

Three-dimensional toroidal magnetic fields with islands: analytical examples and numerical model with scalar functions

W.A. Cooper[1], R. Gruber[2], A.A. Martynov[3], S.Yu. Medvedev[3],
V.D. Shafranov[4], L. Villard[1]

[1]*CRPP Euratom-Confédération Suisse, EPFL, Switzerland*
[2]*Service Informatique Central, EPFL, Switzerland*
[3]*Keldysh Institute of Applied Mathematics, RAS, Moscow, Russia*
[4]*Institute of Nuclear Fusion, RRC "Kurchatov Institute", Moscow, Russia*

1. Analytical examples of 3D toroidal magnetic fields. Analytic 3D plasma equilibrium configurations with the current density $\mathbf{j} = \lambda\mathbf{B}$, $\lambda = constant$ can be obtained as a superposition of several 2D magnetic fields with one coordinate of symmetry (planar, axial or helical). Each of them is given by the following "mixed" representation of the magnetic field:

$$2\pi\mathbf{B} = \nabla\Psi \times \mathbf{b} + F\mathbf{b}, \quad F = F(\Psi) \tag{1}$$

where for specific force free configurations $F = \lambda\Psi$, the base vector $\mathbf{b}$ and the exact solution Ψ of the corresponding Grad-Shafranov equation are known.

In particular, for axisymmetric force-free configurations, $\mathbf{B} = \mathbf{B}_{ax}(r,z), \mathbf{b} = \mathbf{b}_{ax} = \nabla\phi$, the following partial solution can be obtained for the poloidal flux function $\Psi = \Psi_{ax}$:

$$\Psi_{ax}(r,z) = rJ_1(\lambda_2 r)\cos(\lambda_1 z), \quad \lambda_1^2 + \lambda_2^2 = \lambda^2. \tag{2}$$

The up-down symmetric system of isolines of the function (2) has a set of "o-points" (magnetic axes) in equatorial planes $\lambda_1 z = 0, \pm\pi, \pm 2\pi, \ldots$ with r satisfying $J_0(\lambda_2 r) = 0$. The elongation of the magnetic surfaces near the axes is $E = |\lambda_2/\lambda_1|$. An example of the axisymmetric configurations generated by (2) for the values $\lambda = 0.95, \lambda_1 = \lambda_2$ is presented in Fig. 1. For this equilibrium the safety factor q decreases from $q_0 = 0.58$ at the magnetic axis with a resonant surface $q = 0.5$ somewhere inside.

More complex combinations of the exact solutions allow to model more sophisticated configurations including, for instance, doublets. Fig. 2 demonstrates such an example corresponding to the following Ψ_{ax} function

$$\Psi_{ax}(r,z) = rJ_1(\lambda_2 r)\cos(\lambda_1 z) - 0.6rJ_1(\lambda_{2s} r)\sin(\lambda_{1s} z) \tag{3}$$

with the same $\lambda = 0.95$, $\lambda_1 = \lambda_2$ and $\lambda_{2s} = 1.2\lambda_2$, $\lambda_1^2 + \lambda_2^2 = \lambda_{1s}^2 + \lambda_{2s}^2 = \lambda^2$.

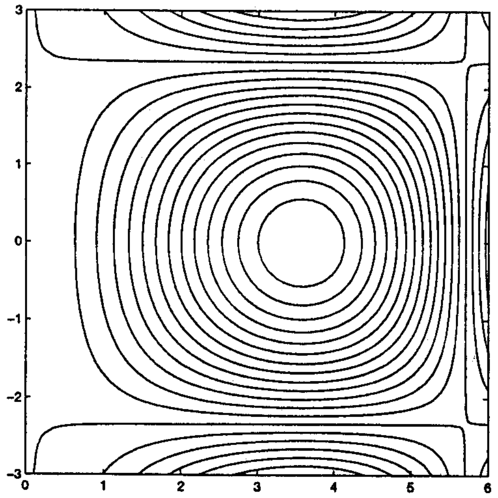

Fig. 1 Magnetic surfaces for an axisymmetric analytic equilibrium from Eq. (2).

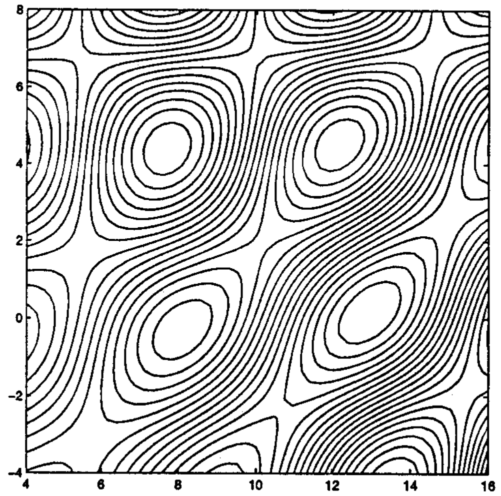

Fig. 2 Magnetic surfaces for an axisymmetric analytic equilibrium with a "figure eight" separatrix from Eq. (3).

2. Scalar function model for 3D MHD equilibrium. The same representation (1) of the magnetic field as in a symmetric case was proposed earlier [1] as a basis for the description of three-dimensional MHD equilibria with "good" (but not necessary nested) magnetic surfaces. The model includes the equations corresponding to basic properties of magnetic field $\operatorname{div}\mathbf{B} = 0, \mathbf{B}\cdot\nabla\Psi = 0, \operatorname{div}(\mathbf{B}\times\nabla\Psi) = 0,$ and the following 3D Ψ-equation

$$\operatorname{div}(b^2\nabla\Psi) + \operatorname{rot}\mathbf{b}\cdot\mathbf{b}\times\nabla\Psi = F\mathbf{b}\cdot\operatorname{rot}\mathbf{b} - 2\pi\mathbf{j}\cdot\mathbf{b} \qquad (5)$$

with a few possible variants for the representation of the current projection term $\mathbf{j}\cdot\mathbf{b}$ taking into account the force balance equation $\nabla p = \mathbf{j}\times\mathbf{B}$, $p = p(\Psi)$. In the general case, this term can be represented as follows

$$2\pi\mathbf{j}\cdot\mathbf{b} = 4\pi^2 p' + b^2F(F' + \alpha), \qquad (6)$$

the function α satisfies the magnetic differential equation: $\mathbf{B}\cdot\nabla\alpha = 2\pi p'\mathbf{q}\cdot\nabla(\ln B^2)$, $\mathbf{q} = \mathbf{b}/b^2$. In the particular case of force free equilibria considered, the term $\mathbf{j}\cdot\mathbf{b}$ in (5) takes the form $2\pi\mathbf{j}\cdot\mathbf{b} = \lambda b^2 F$.

3. Numerical experiments for force free equilibria. The determination of the magnetic flux function given a known magnetic field can be considered as a step in a 3D equilibrium solution. A formulation and numerical solution of this problem is a nontrivial task especially in the case with islands. Moreover in this case, it is not obvious what magnetic flux could be used for the magnetic field description. In a more general formulation, any scalar function Ψ satisfying the condition $\mathbf{B}\cdot\nabla\Psi = 0$ (label function) can be searched for. Together with an arbitrary choice of the function $F(\Psi)$ allowed, it leads to a violation of the closure condition for the base vector $\mathbf{b}$ that was assumed originally [1].

Equation (5) can naturally be considered as an equation for the label function Ψ assuming that the base vector $\mathbf{b}$ that satisfies the basic properties of the magnetic field is known (exactly or approximately). Corresponding numerical experiments were performed for the force free equilibrium magnetic fields described above.

In all computations, the base vector field $\mathbf{b}$ was assumed to be prescribed inside the computational domain. When the magnetic field $\mathbf{B}$ and some approximate label function Ψ_0 are known, then the vector $\mathbf{b}$ can be found from the following representation

$$\mathbf{b} = 2\pi\frac{\mathbf{B}\times\nabla\Psi_0 + F\mathbf{B}}{|\nabla\Psi_0|^2 + F^2}, \qquad (7)$$

which is equivalent to (1) if $\mathbf{b}\cdot\nabla\Psi_0 = 0$. Different label functions Ψ_0 and the same function $F = \mathit{constant} = 1$ were mostly used in the experiments undertaken. The scalar label function Ψ can represent magnetic surfaces with its isosurfaces only if $|\nabla\Psi| = 0$ at the island magnetic axis (similar to the helical flux function). So the input label function with a small gradient at the position of the magnetic island was specified.

The following choices of input function were used in experiments gradually approaching the exact island structure:

- helical flux extrapolated from an axisymmetric configuration;
- helical flux taken from the VMEC approximation with nested surfaces;
- the VMEC helical flux modulated with a simple analytic 3D function to produce an island structure in Ψ_0;
- a "hand-made" label function produced with magnetic field line tracing on a finite grid.

The force-free 3D configuration with a big $m/n = 1/2$ island (Fig. 3) was mostly used for modeling.

All these 3D calculations demonstrate a more or less strong "sausage" effect: one (or several, in general) local extrema of the solution (with spherical isosurface topology instead of toroidal one) appear in place of a magnetic island.

The most adequate result was obtained in the last approach mentioned when the input label function was directly generated in the process of magnetic field line tracing (the "hand made" label). Fig. 5 presents the result of the use of this approach to provide the input label for the Ψ-equation. The solution isosurfaces look in this case rather close to

Helically symmetric magnetic fields $\mathbf{B}_{hel}$ with the current density $\mathbf{j} = \lambda\mathbf{B}$ are described by the representation (1) with $\mathbf{b} = \mathbf{b}_{hel} = (-n/k\nabla z + r^2\nabla\phi)/(n^2/k^2 + r^2)$, $k = n_z/R$, where $2\pi R$ is a helicity period length, n and n_z are helicity numbers in ϕ and z directions respectively. The solution of the corresponding Grad-Shafranov type equation $\Psi = \Psi_{hel}$ is a function of r and $\zeta = n\phi + kz$. One of the partial solutions is the following function

$$\Psi_{hel}(r,\zeta) = \left(\frac{1}{\sqrt{|k^2-\lambda^2|}} r I_n'(y) + \frac{n\lambda}{k(k^2-\lambda^2)} I_n(y)\right)\cos\zeta, \quad y = \sqrt{|k^2-\lambda^2|}\,r \qquad (4)$$

when $k^2 > \lambda^2$. For the case of opposite inequality, the modified Bessel function I_n in (4) should be replaced by J_n. The function (4) was used for testing the PIES code [2].

Due to the linear character of the problem considered, any linear combination of the magnetic fields $\mathbf{B}_{ax}, \mathbf{B}_{hel}$ with the same value of λ is also an equilibrium field. A lot of three-dimensional configurations can be generated in this way. By means of magnetic field line tracing one can easily examine 3D effects on the topology of magnetic surfaces.

For example, adding a small amount of $\mathbf{B}_{hel}$ to $\mathbf{B}_{ax}$ leads to three-dimensional configurations with closed surfaces: $\mathbf{B}_{3Dtor} = \mathbf{B}_{ax} + w_{hel}\mathbf{B}_{hel}$.

Fig. 3 demonstrates the results of such a superposition of the magnetic field shown in Fig. 1 and a $\mathbf{B}_{hel}$ corresponding to the flux function (4) with a weight coefficient $w_{hel} = 0.008$ and $R = 1, n = -1, n_z = 1$. The cross-sections at several toroidal angle values show the 1/2 island generated on the resonant surface $q = 0.5$. No evidence of field line stochastization was found in the region considered.

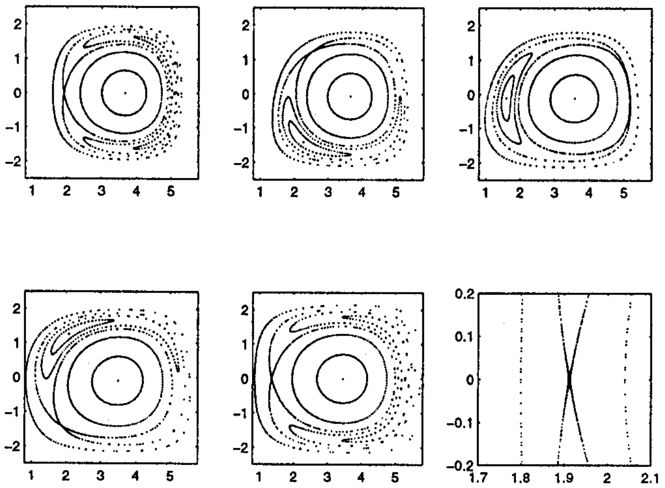

Fig. 3 Poincaré plot of the 3D toroidal magnetic field generated by a helical perturbation of the axisymmetric configuration in Fig. 1. The toroidal cross sections $\phi = 0, \pi/4, \pi/2, 3\pi/4, \pi$ and a zoom of the cross section $\phi = 0$ near the x-point are shown.

The 3D effect of stochastization of a "figure-eight" axisymmetric separatrix is presented in Fig. 4. This is a result of adding $\mathbf{B}_{hel}$ with $w_{hel} = 0.00005, n/n_z = -1/1$ to the "doublet" magnetic field from Fig. 2.

The configurations presented can be used as nontrivial tests for 3D equilibrium codes.

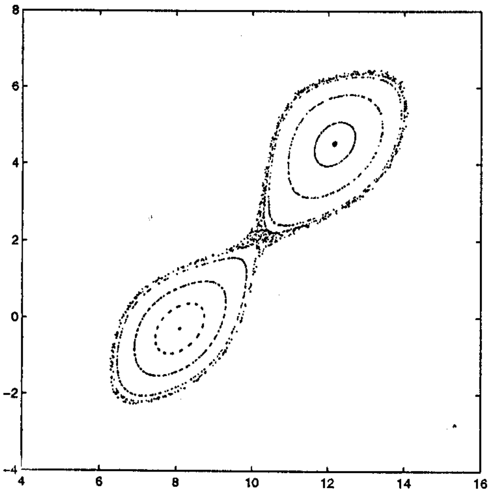

Fig. 4 Poincaré plot of the 3D toroidal magnetic field generated by a helical perturbation of the axisymmetric configuration in Fig. 2. The toroidal cross section $\phi = 0$ is shown.

the exact magnetic surfaces (Fig. 3). The result can be considered as a consistency check for the numerical technique applied and shows that the solution of the 3D Ψ-equation can in principle reproduce the magnetic surface label sufficiently close to the exact one. Moreover the numerical procedure tolerates input label functions that may not necessary be very smooth.

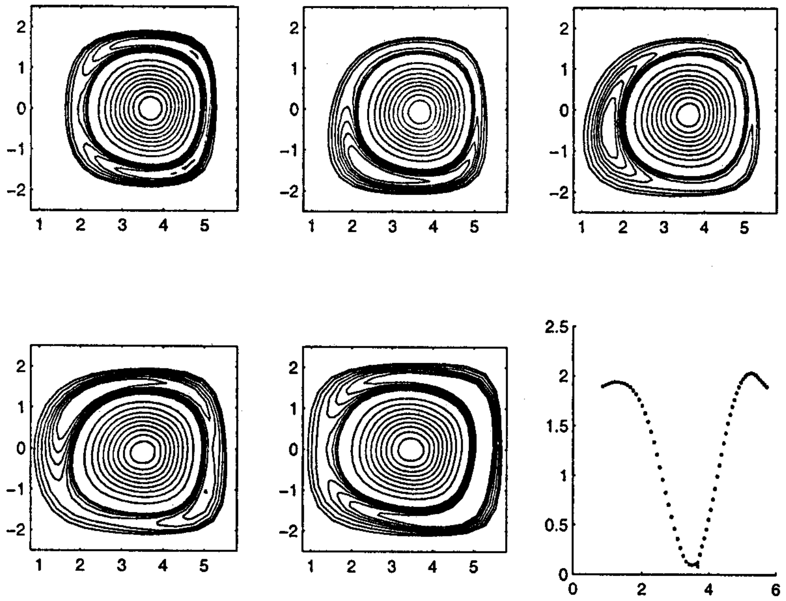

Fig. 5 Isosurfaces of the numerical solution for Ψ-equation (5) when a "hand made" label function is used as the initial one. The isosurfaces (their distribution in the vicinity of the island and the main magnetic axis is varied for the sake of clarity) are shown at the toroidal cross sections $\phi = 0, \pi/4, \pi/2, 3\pi/4, \pi$. The solution values at the $\phi = 0$ equatorial plane are also shown.

The procedure for the "b-vector prescription"/"Ψ-equation solution" can be continued using the output label function as an input for the next iteration. If such iterations converge, then the final converged solution Ψ would actually be a label of magnetic surfaces, i.e. a partial numerical solution of the equation $\mathbf{B} \cdot \nabla\Psi = 0$.

It can hardly be expected that such simple iterative process converges. Moreover the problem of magnetic surface label determination is very ill-posed: it has many solutions if it has one. Even in an axisymmetric case with a poloidal flux function as input, the label function keeps changing from iteration to iteration. However the geometry of the label function level lines does not change considerably. The situation gets worse in the case with islands when incorrect "sausage" topology isosurfaces appear.

One of the possible ways to make the problem well-posed is to prescribe an additional flux function which should effectively fix the label function distribution over the magnetic surfaces. In the case of nested flux surfaces, this could be a fixed label function distribution along any ray emerging out of the magnetic axis.

4. Discussion. The correct formulation of the magnetic surface label determination problem is needed in the general case. This is connected with a large freedom in the magnetic field representation if no closure condition is applied to the base vector **b**. Provided with such a formulation, the procedure for magnetic surface label determination in cases with islands can be developed. This procedure is useful by itself as it can provide selective magnetic island mapping with possible regularization for equilibrium magnetic fields. It can be an essential step for the self-consistent 3D equilibrium problem formulation on the basis of scalar functions.

References

[1] R. Gruber et al. Plasma Physics Reports. **22**, No.3, 186-194 (1996).

[2] A.H.Reiman and H.S.Greenside, J. Comp. Phys. **87**, 349 (1990).

Acknowledgments

The authors thank Drs M. Isaev, M. Mikhailov and A. Subbotin for their help in VMEC calculations and discussions and Dr.S. Hirshman for the use of this code. The CRPP authors were supported in part by the Swiss National Science Foundation.

X-Ray Tomography of Sawtooth Activity During Intense Electron Cyclotron Heating Experiments on TCV

I. Furno, C. Angioni, R. Behn, P. Blanchard, T. Goodman, M. Henderson,
X. Llobet, A. Pietrzyk, C. Nieswand, A. Pochelon, F. Porcelli[1],
H. Reimerdes, E. Rossi[1] and H. Weisen

Centre de Recherches en Physique des plasmas
Association EURATOM - Confédération Suisse
Ecole Polytechnique Fédérale de Lausanne, CH-1015 Lausanne EPFL, Switzerland
[1]Istituto Nazionale Fisica della Materia and Dipartimento di Energetica,
Politecnico di Torino, I-10129 Torino, Italy

INTRODUCTION

Although sawtooth (ST) instabilities have been observed and studied for many years in all tokamaks, the understanding of the underlying physical mechanism is still incomplete. Furthermore, recent experiments have shown that the usual, triangular shaped, Ohmic sawteeth can exhibit a range of shapes during auxiliary Electron Cyclotron Resonance Heating (ECRH). Different types of sawtooth shapes have been observed on TCV (Tokamak à Configuration Variable) with ECRH depending on the plasma and ECRH launching configuration and parameters [1].

The TCV is currently equipped with 3 second harmonic gyrotrons (82.7GHz, 500kW each). Both the poloidal and toroidal mirror angles can be swept for EC heating and non-inductive current drive. This system, together with the unique ability of TCV to produce a wide variety of plasma shapes, allows a detailed study of the influence of various heating scenarios on sawteeth. High temporal resolution is required to resolve the dynamics of the ST collapse phase which, in TCV plasmas, can be faster than 100μs. The TCV soft X-ray tomographic system, which consists of ten 20 channel pinhole cameras, (47μm Be filter), placed in a single poloidal plane, has been recently upgraded with a fast acquisition system with 13μs time resolution. This diagnostic, together with 4 toroidally equispaced Si photodiodes (50μm Be filter, 250kHz time resolution), is used to monitor the poloidal structure of the soft X-ray emission and to determine the toroidal mode number (n = 1, 2). MHD activity is also monitored by toroidal and poloidal arrays of Mirnov coils, with sampling rate up to 1MHz.

In this paper, we report observations of non-standard sawtooth behaviour during ECRH obtained with these high temporal resolution diagnostics. A tentative interpretation of the results is presented on the basis of a recently developed theoretical model [2].

SAWTOOTH BEHAVIOUR RESPONSE TO ECRH POWER DEPOSITION

The soft X-ray and electron density response to a sweep of the EC injection angle are shown in Fig. 1. Plasma parameters are: $\delta_{95} = 0.15$, $\kappa_{95} = 1.28$, $I_p = 192\text{kA}$, $P_{ECRH} = 500\text{kW}$. The EC resonance position is moved through the plasma along a vertical direction with a velocity of 3.5cm / 100ms with a constant plasma shape, albeit with a varying resonance incidence angle and beam width.

The sawtooth shape and period are seen to depend on the sweep position with the longest sawtooth period obtained with power deposition close to the q = 1 surface. The EC resonance location is calculate using the TORAY ray tracing code, while the position of the q = 1 surface is obtained from the TCV magnetic equilibrium reconstruction. A large difference in both the sawtooth period and shape is observed between heating on the q = 1 surface either above or below the magnetic axis. This up-down asymmetry can be attributed to the difference in the local ECRH power density near the q =1 surface caused by the wave beam divergence [3].

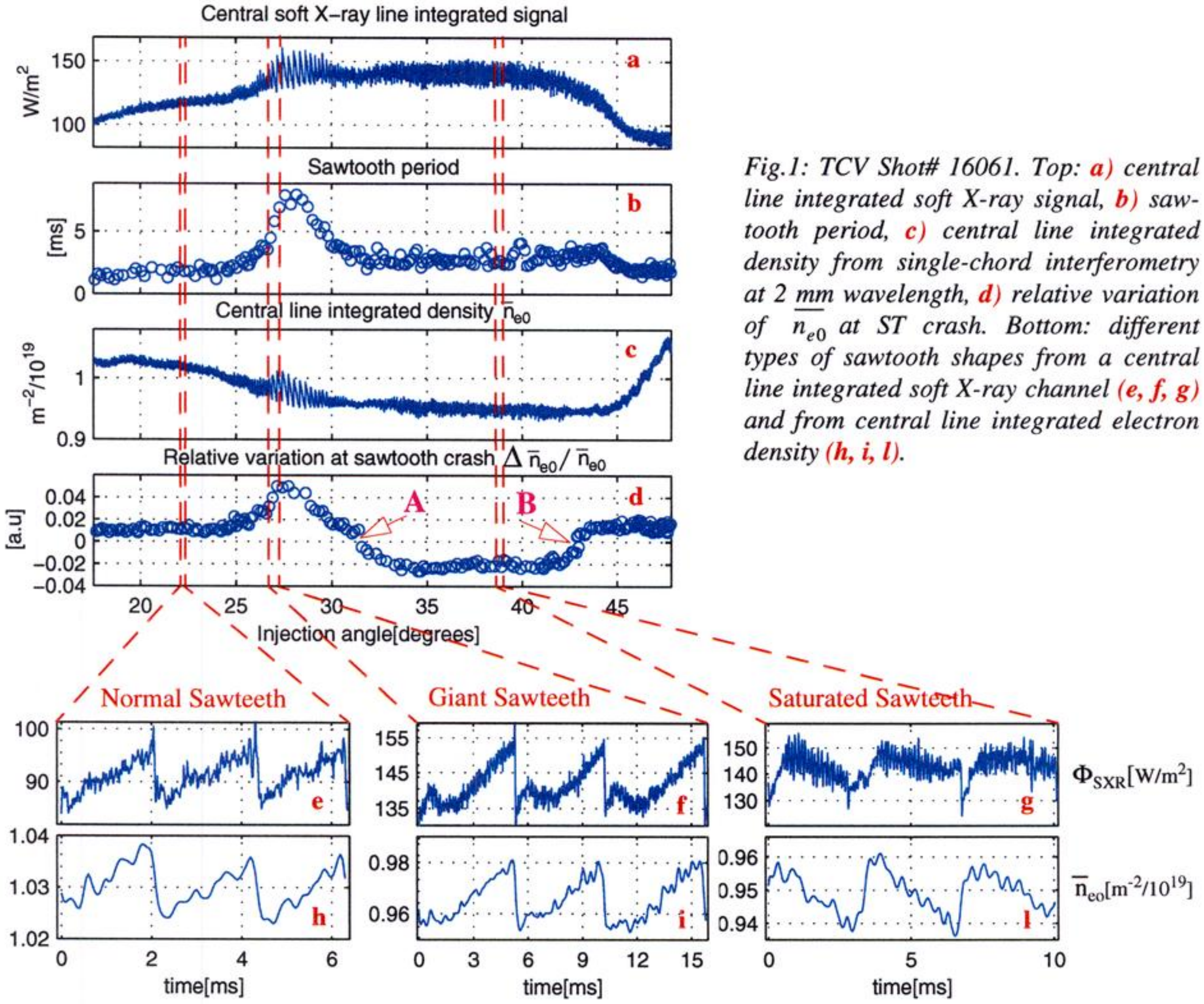

Fig.1: TCV Shot# 16061. Top: ***a)*** *central line integrated soft X-ray signal,* ***b)*** *saw-tooth period,* ***c)*** *central line integrated density from single-chord interferometry at 2 mm wavelength,* ***d)*** *relative variation of* $\overline{n_{e0}}$ *at ST crash. Bottom: different types of sawtooth shapes from a central line integrated soft X-ray channel* ***(e, f, g)*** *and from central line integrated electron density* ***(h, i, l)****.*

The time behaviour of the central line integrated electron density $\overline{n_{e0}}$ (monitored by a 2 mm single-chord interferometer) strongly depends on the EC resonance position. For injection angles in the interval **[A,B]** on Fig. 1.d, corresponding, within experimental uncertainties, to power deposition inside the ST inversion radius, $\overline{n_{e0}}$ decreases between two subsequent ST crashes (Fig. 1.l), resulting in central line-integrated soft X-ray traces which show partial, or even inverted, ST behaviour. The decrease of $\overline{n_{e0}}$ results from a flattening of the electron density profile, which is measured by multichord FIR interferometer. With ECRH power deposition outside the ST inversion radius, $\overline{n_{e0}}$ shows normal (i.e. triangular) sawtooth behaviour.

MHD activity is different when heating either inside or outside the q = 1 surface. With central ECRH, partially saturated, saturated and inverted sawteeth are observed on the soft X-ray traces. For these sawteeth, the reheating ramp can be partially or completely interrupted by a phase of oscillations which show frequency doubling on some photodiode channels. These oscillations are caused by a m/n = 1/1 mode, rotating in the electron diamagnetic drift direction at a frequency of ~6kHz (Fig. 2, SVD-Topos# 2, 3), coupled to a m/n = 2/2 structure (Fig. 2, SVD-Topos# 4, 5), resulting in the frequency doubling. During the saturated phase, coupled $m \geq 2$, n=1 modes are also seen by the Mirnov coils. With ECRH power deposition outside the

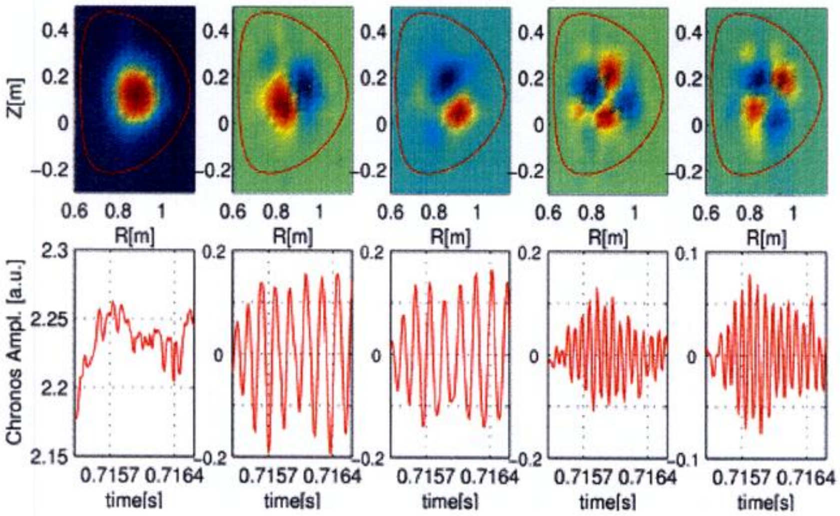

Fig. 2: TCV Shot# 14386. Shot parameters: $\delta_{95} = 0.34$, $\kappa_{95} = 1.33$, $q_{95} = 3.4$, $n_{e0} = 1.1*10^{19}$ m^{-2}, P_{ECRH} *= 500 kW (on-axis heating). SVD analysis of tomographically reconstructed soft X-ray emissivity distribution during the saturated phase. The figure shows the Topos with the LCFS (top) and the corresponding Chronos (bottom).* SVD-*Topos# 2, 3 show the m/n = 1/1 mode, while SVD-Topos# 4, 5 show the coupled m/n = 2/2 rotating structure.*

q = 1, mode activity consists of brief m/n = 1/1 precursors or postcursors of the ST crash, which are not observed during the sawtooth reheating ramp.

Highly peaked soft X-ray emissivity profiles at the end of the ST ramp have been observed with on-axis ECRH power deposition (Fig. 3.a). Here, the fast relaxation phase is preceded by a m/n = 1/1 precursor which typically grows over several hundreds microseconds. At the sawtooth crash, the soft X-ray emissivity peak moves outwards (Fig. 3.c) and tends to redistribute forming a hot ring localized near the inversion radius (Fig. 3.f).

The formation of a hot ring, and the subsequent hollow emissivity profiles, can be sustained during the sawtooth ramp with very localized ECRH power deposition near the q = 1 surface, as shown in Fig. 4 for TCV Shot# 15278. In this experiment the EC resonance is placed near the high field side of the q=1 surface which results in the highest ECRH power density. The hollow emissivity profile following the ST crash is maintained for ~3ms until a slow m/n = 1/1 instability develops.

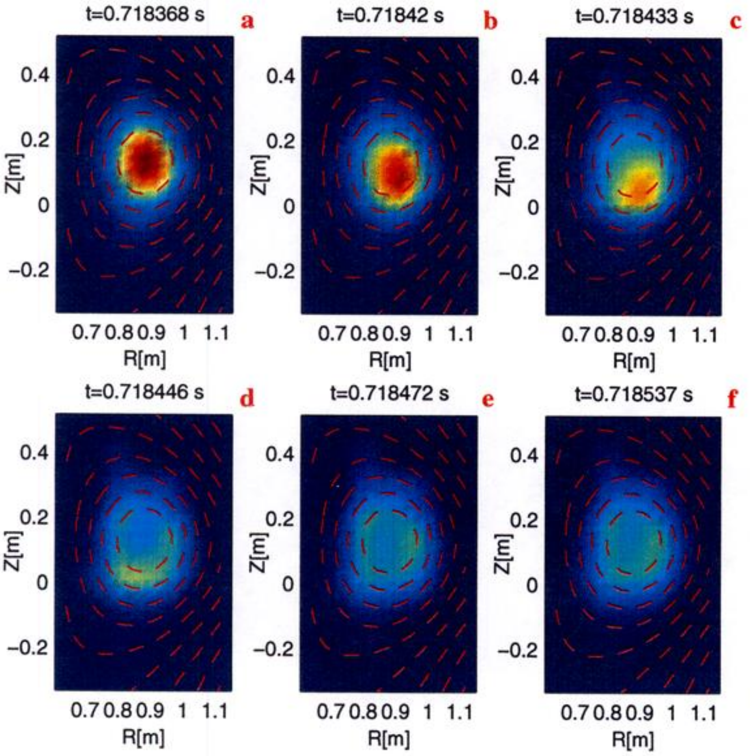

Fig. 3: For the same TCV shot of Fig. 2 an expanded view of the sawtooth relaxation phase. The soft X-ray emissivity is shown together with flux surfaces (in red).

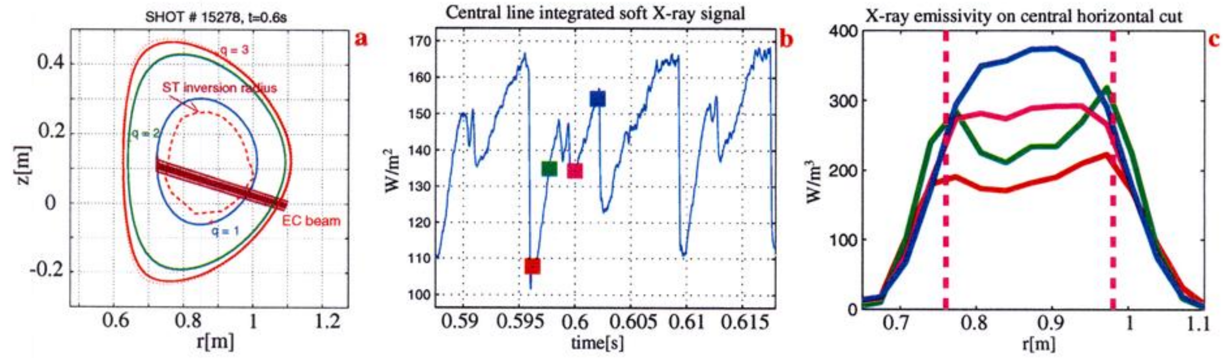

*Fig. 4: TCV Shot# 15278. Shot parameters: $\delta_{95} = 0.4$, $\kappa_{95} = 1.42$, $q_{95} = 2.5$, $n_{e0} = 0.9*10^{19}\mathrm{m}^{-2}$, P_{ECRH} = 500kW. **a)** Rational flux surfaces with EC resonance position and ST inversion radius. **b)** Giant sawteeth on a central soft X-ray channel. **c)** Reconstructed emissivity profiles along horizontal cut at different times.*

This instability appears to mix the plasma close to the q = 1 surface with the plasma core, resulting in a peaking of the soft X-ray emissivity profile, whilst the electron temperature profile remains flat [4].

SAWTOOTH MODELLING

A numerical code, based on a theoretical model recently developed [2], has been used to simulate the different ST behaviours. The combined effects of a m/n = 1/1 magnetic island dynamics, a localised heat source, a large parallel heat diffusivity and plasma rotation are included. Non-standard ST features, like the formation of a hot ring near the q = 1 surface and frequency doubling, are reproduced by the model, in qualitative agreement with the experimental data.

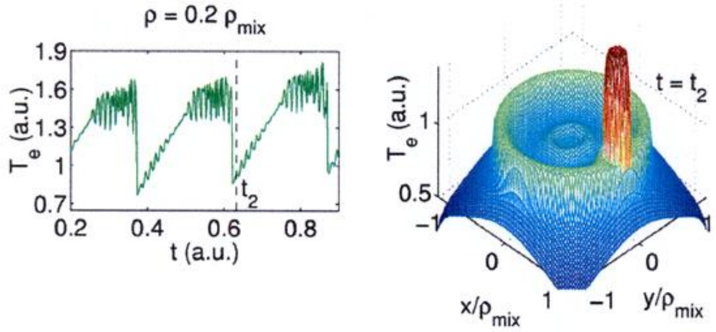

Fig. 5: Simulation of saturated partially sawteeth with central ECRH power deposition [5]. Right: temporal evolution of the central electron temperature. Left:2D temperature profile after the ST crash.

Acknowledgments

This work was partly funded by the Swiss National Science Foundation.

References

[1] Z. A. PIETRZYK et al., Nuclear Fusion **39** (1999), 587

[2] F. PORCELLI, E. ROSSI, G. CIMA and A. WOOTTON, Phys. Rev. Lett. **82**, (1999) 1458

[3] T. GOODMAN et al., this conference

[4] R. BEHN et al., this conference

[5] A. POCHELON et al., accepted for publication in Nuclear Fusion, IAEA 1998 Yokohama Special Issue

Poloidally Asymmetric Plasma Response during ECH Experiments in TCV

T.P.Goodman, M.A.Henderson, J.-Ph.Hogge, Z.A.Pietrzyk, A.Pochelon,
O.Sauter

*Centre de Recherches en Physique des Plasmas, Ecole Polytechnique Fédérale de Lausanne,
Association EURATOM-Confédération Suisse, CH-1015 Lausanne EPFL, Switzerland*

Introduction: Plasma experiments using absorption of radiation in the range of the electron cyclotron frequency are often grouped under two separate headings: electron cyclotron heating (ECH) or electron cyclotron current drive (ECCD). The division is based, roughly, on the toroidal angle-of-incidence between the beam and the toroidal magnetic field direction. In practice, ECH experiments are those in which there is no projection of the k-vector on the toroidal field, $\mathbf{B}_\phi$. For the flexible launching systems of present day tokamaks, this rough division is not strictly correct; although, for the purpose of indicating the intent of an experiment it may still be valid.

Due to the presence of the poloidal field, a beam launched with no toroidal angle can nevertheless have a non-negligible projection of it's **k**-vector along the total field and thereby produce Doppler-shifted absorption leading to ECCD; that is, a so-called ECH experiment can produce ECCD when absorption is off-axis. The direction (co/counter) and quantity of ECCD will depend on the absorption location, launch direction (HFS versus LFS) and toroidal field direction but not the plasma current direction. Both the poloidal field and the plasma current producing the poloidal field, change direction at the same time therefore simply reversing the plasma current will not change the relative direction of the ECCD (e.g. co-ECCD will remain co-ECCD). The toroidal field must be reversed. Because it is the poloidal field that creates the asymmetry, the effects are seen only during off-axis absorption.

Previous experiments on TCV have produced poloidally asymmetric plasma responses during so-called ECH experiments[1]. Here, we give experimental evidence that the asymmetry is due to the presence of ECCD.

Experimental setup: Up to 1.5 MW second harmonic heating (X2, 82.7 GHz) from three 0.5MW gyrotrons was directed to the plasma by three independent launching antennas (launchers). One launcher is mounted in an equatorial port (L1) and two launchers (L2 and L3) are mounted in upper lateral ports. Each launcher has 2 degrees of freedom, one of which provides steering of the beam in a fixed plane during a shot; the other allows that plane to be rotated about the TCV major radius (pointing out through the center of the launcher port) between shots. Each gyrotron can be independently switched to the torus or to a calorimetric load from shot to shot, such that power can be delivered from any possible combination of three launchers for a given shot.

The TCV vacuum vessel can accommodate various plasma shapes and elongations; however, these experiments were performed on low density ($2*10^{-19}$ m^{-3}), low elongation ($\kappa\approx1.3$), moderate q_a (≈4) plasmas centered between the equatorial and upper lateral ports. This provides geometric symmetry. The beam was swept through a stationary plasma so that all external conditions remain constant (e.g. location of plasma on the limiter, geometric configuration between diagnostics and the plasma, induced currents required to move the plasma, etc.) and only absorption-induced plasma changes are produced. Sweeps allow comparison of heating at different locations in the same plasma during a single shot. Experiments were performed for both toroidal field directions and with various combinations of launchers to allow any systematic asymmetries (e.g. gyrotron output power, beam power density, etc.) to be clarified.

Optimum coupling of the beam to the plasma would require modification of the polarization during such sweeps since the location at which the beam enters the plasma changes in time; however, with the proper choice of a constant polarization the coupling can remain acceptably high (e.g. >95% X-mode) and symmetric at all times.

As expected, TORAY [2] X-mode ray-tracing calculation with injection in the poloidal plane (no toroidal injection) show linear current drive efficiencies which change sign when heating above or below the plasma midplane: purely perpendicular incidence on the field line at the resonance cannot be assured for all poloidal angles. Previous ECCD experiments [3] have demonstrated that the X-ray tomography diagnostic shows clear differences in sawtooth shape and period suggesting that a signature for co- and counter-ECCD exists even at low ECCD efficiencies like those calculated by TORAY for no toroidal injection. Ray-tracing shows that refraction may make it difficult to superimpose different beams at the same height in the plasma; therefore, launch angles were preprogrammed to sweep the refracted beams vertically along the resonance at a constant rate.

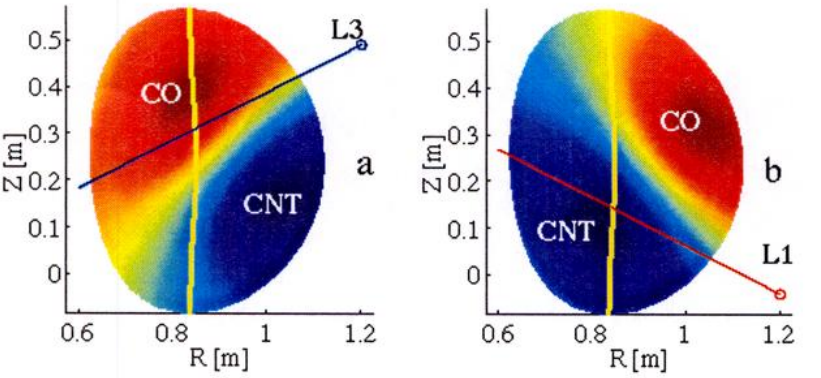

Figure 1. Poloidal cross-section showing the $k_{//}$ contours for a so-called ECH experiment (shot 16053, t=1.189s). Red indicates co-ECCD and blue indicates counter-ECCD. Both launcher L3 (a) and launcher L1 (b) produce co-ECCD above midplane and counter-ECCD below, although of different magnitudes, when the beams (L3-blue and L1-red lines) are swept along the resonance (yellow line).

A general understanding of the potential for ECCD is gained by calculating the projection of the k-vector on the field, since it is the Doppler shifted absorption by electrons streaming along the field that is ultimately responsible for the current drive. This is shown in Figure 1 for the plasma-beam configuration used in these experiments and a given toroidal field direction (recall that the sign of the driven current depends on the sign of $\mathbf{B}_\phi$, only). It is important to remember that the figure pertains to the k-vector in the poloidal plane of the tokamak (zero toroidal injection angle).

Experimental results: Sweeps of each launcher individually show that when crossing the q=1 surface, *a)* density pump-out occurs and central temperature rises sharply such that line-integrated X-ray emission, as seen on the central X-ray tomography channels, increases significantly, *b)* the sawtooth period and amplitude increases at the transition from outside to inside, *c)* the change in period and amplitude is much larger on the side nearer the launcher than on the opposite side, *d)* the width of the transition region is larger when passing from inside to outside (rather than outside to inside) the q=1 surface, *e)* the amplitude of the peak in sawtooth period increases with co-ECCD and decreases with counter-ECCD (produced by intentionally introducing small toroidal angles) and *f)* the width of the transition region is of the order of the free-space beam width projected on the resonance at the heating location (~3cm). Since the experiments perturb the density *(a)* and the transition region is small *(f)*, it is very difficult to superimpose beams even with preprogramming. On the other hand, this region is a highly localized,

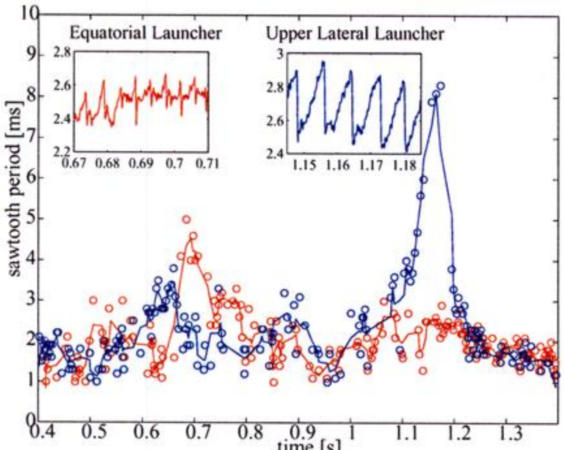

Figure 2 Sawtooth period variation during sweeps of L1 (red) and L3 (blue) separately from below to above mid-plane (dz/dt=0.35m/s). The peaks correspond to the lower and upper q=1 regions. The sawtooth shape is seen in the insets. Note that the peak is clearly larger on the side nearer the corresponding launcher.

easily recognizable target location in the plasma and can be used as a diagnostic for in situ testing of the relative alignment between launchers.

The transition region is of particular interest because it allows the confirmation that ECCD is responsible for the non-axisymmetric plasma response. Figure 2 shows the plasma response when heating with either an upper lateral (L3) or equatorial (L1) gyrotron alone ($\mathbf{B}_\phi>0$). Large more-or-less triangular sawteeth appear *only* when heating near the upper q=1 surface with L3 and not with L1. Non-triangular, but nevertheless large, sawteeth occur when heating near the lower q=1 surface with L1 and not L3. When $\mathbf{B}_\phi$ is reversed, these results are reversed as well, with L1 playing the role of L3 and vice versa. Therefore, we can conclude that for the same launcher, *a)* the near-side sawtooth shape depends on the driven current direction and *b)* similar sawteeth changes cannot be produced on the opposite side of the plasma. Taking the large regular sawteeth, the fact that the roles of an upper lateral and equatorial launcher are reversed when the field is reversed, suggests that it is either *a*) the current driven (proportional to the power density) or, *b)* the beam width, that determines whether or not these sawteeth can be created. By fixing the beam absorption on the transition region and varying the beam power, we keep the beam width constant and vary the power density. Sawteeth do not change shape but become larger with power density. This suggests that in the case of heating on the opposite side of the q=1 surface (i.e. far side transition region for a given launcher), the beam width plays the dominant role in determining the sawtooth shape (Note: the *sign* of the ECCD for the far-side transition region for a given launcher is the same as for the opposing launcher's near-side transition region when $\mathbf{B}_\phi$ is reversed).

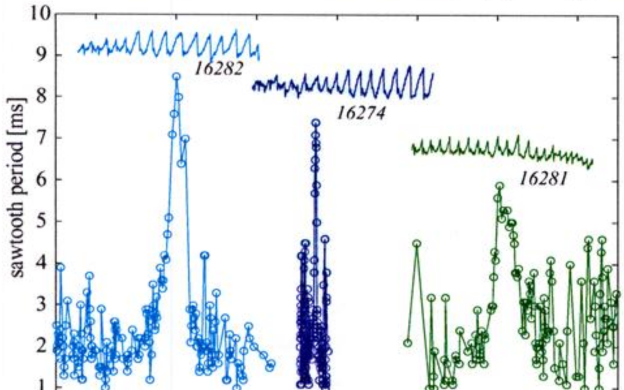

Figure 3 Elimination of co-ECCD component at near-side transition region for L1 with B_ϕ reversed. Shot 16281 is pure ECH at the sawtooth period peak. The beam is swept over the same range as in Figure 2 passing through both the near and far side transition regions. The plane of sweep is rotated by +/- 8° relative to the poloidal plane of the tokamak. (Insets have equal scales).

For the near side transition using L1 with $\mathbf{B}_\phi$ reversed, the co-ECCD Doppler component which exists at resonance for launch in the poloidal plane can be eliminated or enhanced by intentionally adding a toroidal angle to the launched beam. The resulting peaks in sawtooth period as well as the sawtooth shapes are shown in Figure 3. Positive angles decrease the ECCD component: +4° corresponds to pure ECH. For each shot, the same mirror range was swept and the beam passes through both the upper and lower transition regions. However, since the beam lies in a plane which is rotated about the major radius passing through the launcher ports, the sweep range in toroidal angle increases as the plane is tilted more relative to the poloidal plane of the tokamak. The time at which the beam crosses the near-side transition region will change by less that one sawtooth period. Large triangular sawteeth only occur with a co-ECCD component and when the absorption occurs over a narrow extent in minor radius (near-side). Similarly, large triangular sawteeth can be created by over-compensating the inherent counter-ECCD offset on the near-side with the standard $\mathbf{B}_\phi$, leading to co-ECCD

The narrow range over which the large regular sawteeth occur allows the determination of the beam absorption location if one admits that there exists a correlation with some yet-to-be-determined but physically relevant location in the plasma. If this location can be proven to be tied to a physical relevant location of interest such as the q=1 radius by simultaneous measurements of q, for example using the MSE diagnostic on DIII-D, it could provide a tool for testing and refining the details of models describing the sawtooth instability [4]. Tokamaks with ECH but not equipped to measure the q-profile could then find this location by sweeping the heating location and constrain equilibrium reconstruction codes accordingly.

In any case, without specifying the exact location, *a)* differences of heating location of 10mm (~2.5% of plasma radius) are easily measured based on these transitions even though most diagnostics have a spatial resolution of ~3-4cm, *b)* individual beam-plasma aiming is confirmed to be reproducible to 0.2° (±3mm at resonance near the middle of the launcher's angular range) and *c)* the two upper lateral launchers are confirmed to heat the same location within this reproducibility for the same angle settings, producing large sawteeth. However, refraction limits the ability of aiming an upper lateral and an equatorial launcher with the necessary accuracy to cause reliable beam overlap at a given height even though attempts were made to correct for refraction a priori. In this heating scenario, the large sawteeth become less regular, perhaps beam-width dominated.

Conclusion: Poloidally asymmetric plasma responses, particularly sawtooth shape and amplitude, have been shown to be consistent with the presence of ECCD during sweeps of the heating location in the poloidal plane of a tokamak plasma. Large regular sawteeth are produced over a very narrow spatial range, provided the beam absorption width is narrow and some co-ECCD is present. Broad absorption appears to perturb the triangular sawtooth shape.

It seems reasonable to expect that local ECCD applied at the q=1 surface lowers the shear so as to produce sawtooth stabilization, extending the period and increasing the amplitude. The one dimensional code PRETOR has simulated the effect of pure ECH. The sawtooth period increases when passing inside the q=1 radius, but shows no peaking of the sawtooth period near the q=1 radius [5]. Simultaneous measurement of the q-profile and heating location would help to clarify the physical mechanisms at work in producing different sawtooth shapes: for example, a precise knowledge of the heating location relative to q=1 is necessary to allow direct comparison between experiments and the 2D model of sawtooth dynamics recently proposed by Porcelli [4].

Ackowledgements: This work was partially supported by Swiss National Science Foundation.

References

[1]T.P. Goodman et al., Proc. of Joint ICPP (1998) and 25th EPS Conf. on Cont. Fusion and Plasma Physics, Praha 1998, ECA **22c** (1998) 1324.

[2] G.R. Smith, et al., in Proc. of the 9th Joint Workshop on ECE and ECRH at Borrego Springs, California (January, 1995), Editor World Scientific (1995) 651.

[3] T.P. Goodman et al., 2nd EPS Conf. on Radio Freq. Heat. and CD of Fus. Dev. Brussels **22A** (1998) 245.

[4] F. Porcelli, E. Rossi, G. Cima and A. Wootton, Phys. Rev. Lett. **82** (1999) 1458.

[5] O. Sauter et al., Proc. of the Theory of Fusion Plasmas workshop,Varenna 1998, Editrice Compositori, J.W. Connor, E. Sindoni and J. Vaclavik (Eds.), Bologna (1999) 403.

FIRST GLOBAL LINEAR GYROKINETIC SIMULATIONS IN 3D MAGNETIC CONFIGURATIONS

G. Jost, T.M. Tran, L.Villard, W.A. Cooper, K. Appert
Centre de Recherches en Physique des Plasmas
Association Euratom - Confédération Suisse
Ecole Polytechnique Fédérale de Lausanne

Introduction : In the recent past, the neoclassical theory has been the main focus of transport studies in alternative magnetic confinement devices. Today it is quite well developed and has served to identify configurations with enhanced neoclassical transport properties. On the other hand, the effects of microinstabilities on transport, though extensively investigated in tokamaks, have received little attention in 3D configurations. In a previous work [1], we presented a code aimed at the investigation of Ion Temperature Gradient (ITG) modes for such 3D magnetic configurations. This code has been successfully validated in axisymmetric configurations, but the computational time required by this version becomes prohibitive for full 3D cases. The code we present here is a modified version of this 3D code improved by the implementation of the extraction of the fast spatial variation [2]. The code meanwhile ported on a CRAY T3E is benchmarked against the helical version of the GYGLES code [3]. Results in a 3D configuration, namely a tokamak with a helical boundary deformation, are also presented.

Model and Implementation : The plasma is modeled by gyrokinetic ions and adiabatic electrons, and the code follows the time evolution of quasi-neutral electrostatic perturbations of the local Maxwellian distribution function f_0 [1]. The MHD equilibrium code VMEC provides the magnetic configurations [4]. We write the electrostatic potential as

$$\phi(s,\theta^*,\varphi,t) = Re\left(\tilde{\phi}(s,\theta^*,\varphi,t)e^{iS(s,\theta^*,\varphi)}\right),\ S(s,\theta^*,\varphi) = m_0\theta^* + n_0\varphi$$

where (s,θ^*,φ) are the PEST-1 coordinates, $s = \Phi/\Phi_0$ where $2\pi\Phi$ is the toroidal flux, θ^* a poloidal angle which makes the field lines straight, φ is the geometric toroidal angle, $\tilde{\phi}$ is the extracted potential, S is the fast spatial phase, m_0 and n_0 are integer numbers which are both input parameters of the code. The ITG driven modes being aligned with the magnetic lines, i.e. $k_{\|} << k_{\perp}$, we choose $m_0 \approx n_0 q(s_0)$, with $q(s_0)$ the safety factor at $s = s_0$ where the ion temperature gradient peaks.

Using the same transformation for the perturbed ion distribution function f, the code now solves the following system of equations :

$$\frac{d\vec{R}}{dt} = v_{\|}\vec{h} + \frac{v_{\|}^2 + v_{\perp}^2/2}{\Omega}\vec{h} \times \frac{\vec{\nabla}B}{B},\ \frac{dv_{\|}}{dt} = \frac{1}{2}v_{\perp}^2\vec{\nabla}\cdot\vec{h},\ \frac{d\mu}{dt} = 0,$$

$$\frac{en_0}{T_e}\tilde{\phi}(\vec{x}) - (i\nabla_{\perp}S + \nabla_{\perp})\cdot\left[\frac{n_0}{B\Omega}(i\nabla_{\perp}S + \nabla_{\perp})\tilde{\phi}(\vec{x})\right] = \tilde{n}_i(\vec{x}),$$

$$\tilde{n}_i(\vec{x}) = \int \tilde{f}(\vec{R}, v_{\|}, v_{\perp})\delta^3(\vec{R} - \vec{x} + \vec{\rho})e^{i(S(\vec{R})-S(\vec{x}))}Bd\vec{R}d\alpha dv_{\|}d\mu,$$

$$\frac{d}{dt}\tilde{f} + i\frac{dS}{dt}\tilde{f} = -\frac{\langle\vec{\tilde{E}}\rangle \times \vec{B}}{B^2}\frac{\partial f_0}{\partial\vec{R}} - \frac{q_i}{m_i}\vec{h}\cdot\langle\vec{\tilde{E}}\rangle\frac{\partial f_0}{\partial v_{\|}} - \left(v_{\|}\frac{\partial f_0}{\partial v_{\|}} + \frac{1}{2}v_{\perp}\frac{\partial f_0}{\partial v_{\perp}}\right)\langle\vec{\tilde{E}}\rangle\cdot\vec{h}\times\frac{\vec{\nabla}B}{B^2},$$

$$\langle \vec{\tilde{E}} \rangle = -\frac{1}{2\pi} \int (i\nabla S + \nabla)\tilde{\phi}(\vec{x}) e^{-i(S(\vec{R})-S(\vec{x}))} dx d\alpha,$$

where the symbols have their usual meaning [1].

The equations governing the ions have been discretized using a Particle-In-Cell scheme, and the gyrokinetic Poisson equation is solved in the PEST-1 magnetic system of coordinates using a finite element approximation for the extracted electrostatic potential $\tilde{\phi}$. We choose quadratic splines as finite element basis [1].The RHS of the discretized Poisson equation is Fourier filtered in the poloidal and toroidal directions, we keep only some modes around (m_0, n_0), the shape and the width of the filter being a function of the magnetic configuration.

As we now solve only the slow spatial variation of the potential, the number of grid points is independent of the toroidal wave number n, usually equal to the number of processors.

Results : We have compared the results obtained with the full 3D code and the helical version of the GYGLES code [3]. The helical GYGLES code is a 2D code aimed at the investigation of ITG modes in helically symmetric configurations. It solves the same system of equations, but in a helical system of coordinates (x', y'), with $x' = r\cos(\zeta)$, $y' = r\sin(\zeta)$, $\zeta = \theta - hz$, where (r, θ, z) are the cylindrical coordinates, and h the helicity. In GYGLES, Poisson's equation is solved in the (s_h, θ_h) magnetic coordinates, s_h is a normalized radial variable $\propto \psi_h^{1/2}$, where ψ_h is the helical flux, and θ_h is equal to $\tan^{-1}(y'/(x' - x'_M))$, $(x'_M, 0)$ is the position of the magnetic axis. The helical code uses an analytical vacuum solution [3] for the magnetic configuration.

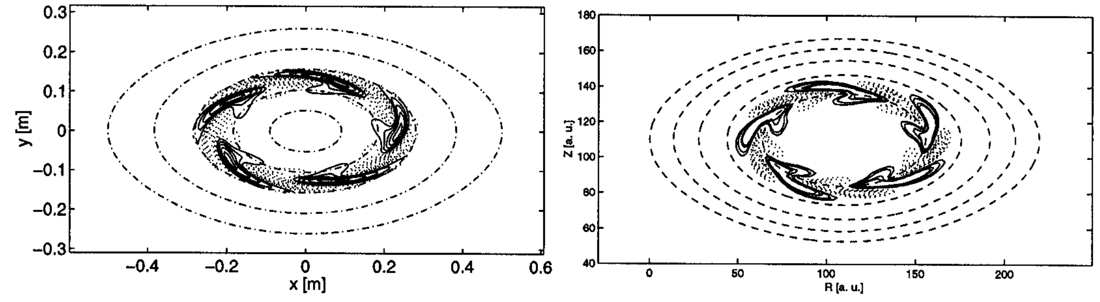

Figure 1: *Level surfaces of the electrostatic potential ϕ in a straight L=2 configuration obtained with the helical GYGLES code in the (x', y') plane (left) and the full 3D code in the (R, Z) plane at $\varphi = 0$ (right). Dashed lines are the magnetic surfaces at $s_h = .2, .4, .6, .8, 1$ (left) and $s = .2, .4, .6, .8, 1$ (right). The ion temperature gradient peaks at $s_{h0} = 0.5 \equiv s_0 = 0.2$.*

For this benchmark, we used the following procedure : for a given helical configuration, we obtained the position of the last magnetic surface ($s_h = 1$), from which we computed the Fourier coefficients $R_{m,n}(s = 1), Z_{m,n}(s = 1)$ required by VMEC as input parameters [4] for the MHD equilibrium. We recomputed the configuration, and provided VMEC's results to the 3D code. Thus we tested also the interface between VMEC and the 3D code for a full 3D problem.

Comparisons were performed with two cases, a straight L=2 stellarator and a straight heliac configuration with a helicity $h = 1\,m^{-1}$ and $B = 1\,T$ at the magnetic axis. The equilibria computed by VMEC were centered at $R_{00} = 100\,m$ with a number of field periods N_{per} equal to R_{00}, simulations were performed over one period. In the helical

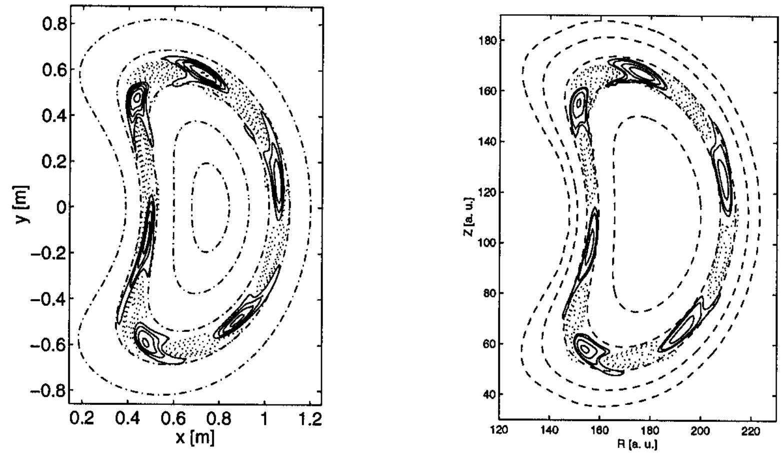

Figure 2: *Electrostatic potential* ϕ *in a straight heliac obtained with GYGLES in the* (x', y') *plane (left) and the full 3D code in the* (R, Z) *plane at* $\varphi = 0$ *(right). The ion temperature gradient peaks at* $s_{h0} = 0.7 \equiv s_0 = 0.5$.

system of coordinates, an ITG mode can be defined by a "helical" mode number n_h [3]. With a helicity $h = 1\,m^{-1}$, we can easily show using the definitions of (x', y') than the toroidal mode number n is related to n_h by : $n/N_{per} = m - n_h$, where m is the poloidal mode number.

For the L=2 case (figure 1), the ion temperature gradient peaks at $s_{h0} = 0.5 \equiv s_0 = 0.2$, $a/L_T = 10$, $T_i(s_0) = 1keV$, $q(s_0) = 5.5$, and the density profile is flat. For a helical wave number $n_h = 4$, GYGLES produces a mode with a dominant poloidal mode number $m = 5$ and a frequency and a growth rate equal to 139.5 kHz and 52 kHz, respectively. With $m_0 = 5$ and $n_0/N_{per} = 1$, the frequency and the growth rate obtained with the 3D code agree well, being equal to 139 kHz and 55 kHz, respectively. The global shape of the mode agrees also for both codes, but the GYGLES code which solves the equations on a small portion of the s_h-axis, here between $s_h = 0.3$ and $s_h = 0.7$, provides a more precise picture of the mode than the 3D code which solves the problem in the whole radial domain $0 \leq s \leq 1$.

Figure 2 shows the comparison for the heliac case, here $n_h = 4.2$, the ion temperature gradient peaks at $s_{h0} = 0.7 \equiv s_0 = 0.5$, $a/L_T = 10$, $T_i(s_0) = 4keV$, $T_e/T_i(s_0) = 0.1 + 0.9(1 - s_h^2)$, the density profiles are flat. We choose $m_0 = 6$ and $n_0/N_{per} = 1.8$ and we keep the following modes by filtering : $(m_0 + i, n_0/N_{per} + i), i = [-4, 4]$. Both codes produce a mode with a $m = 6$ dominant poloidal spectrum. The frequencies and growth rates 138 kHz and 40 kHz with GYGLES and 132 kHz and 34 kHz with the 3D code agree well.

The 3D simulations were performed with 4×10^6 particles, with 64 points in each direction (s, θ^*, φ), they required $\approx$ 180 cpu-seconds per step with 64 processors on a CRAY T3E.

A first result with a 3D configuration is shown in figure 3. We choose a tokamak with an L=2 helical boundary deformation. The positions R, Z of the last magnetic surface $s = 1$ for the computation of VMEC equilibria are given by :

$$\begin{cases} R &= R_{00} + \cos(\theta) + \delta(\cos(\theta) + \cos(\theta - 2N_{per}\varphi)) \\ Z &= \sin(\theta) + \delta(\sin(\theta) - \sin(\theta - 2N_{per}\varphi)) \end{cases}$$

where θ is the geometric poloidal angle, δ is the amplitude of the boundary deformation,

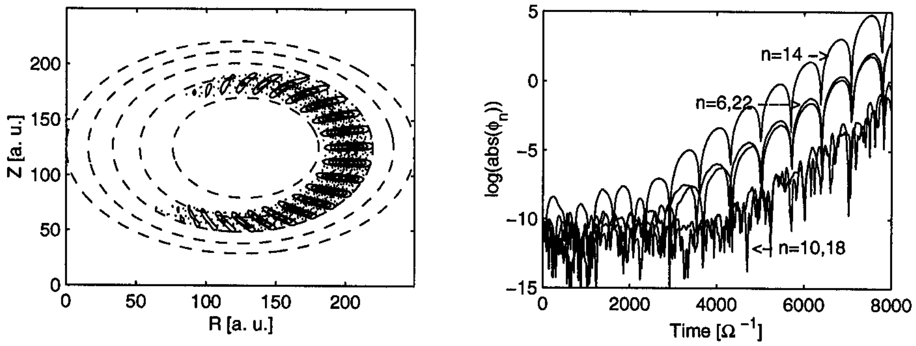

Figure 3: *Level surfaces of the electrostatic potential* ϕ *in* (R, Z) *at* $\varphi = 0$ *and* $t = 6000\,\Omega^{-1}$ *(left) and time evolution of the absolute value of the toroidal spectrum of the potential measured in* $s = s_0$ *and* $\theta^* = 0$ *(right), we show here only the modes* $n = 6, 10, 14, 18, 22$.

$R_{00} = 4\,m$, $N_{per} = 4$, and the helicity of the perturbation is equal to $1\,m^{-1}$. The safety factor is a parabolic function of the poloidal flux, the ion temperature gradient peaks at $s_0 = 0.4$ where $q(s_0) = 2.5$, $a/L_T = 3.6$, and $a/\rho = 96$ with ρ the Larmor radius at s_0. In the tokamak case ($\delta = 0$), with these parameters, the maximum growth rate is obtained with $n = 14$ and is equal to $0.00208\Omega^{-1}$ with a frequency $= 0.0054\Omega^{-1}$. Figure 3 shows the result for a perturbation $\delta = 0.15$, where we keep the following modes by filtering : $(m_i, n_j) = (m_0 + i + j, n_0/N_{per} + j), i = [-6, 6], j = [-8, 8]$ with $(m_0, n_0) = (34, 14)$. The ITG mode is now a 3D mode characterized by several toroidal modes numbers, its spectrum is centered around the mode $(34, 14)$. Figure 3 shows also clearly the effects of such L=2 deformation where only toroidal components satisfying $\mathrm{mod}(n - n_0, 2N_{per}) = 0$ can couple with the component n_0. However the growth rate and frequency of the 3D mode, which are equal to $0.0022\Omega^{-1}$ and $0.005\Omega^{-1}$ are not significantly modified by the helical deformation.

We applied also a L=3 helical boundary deformation to a tokamak, keeping the same equilibrium parameters. We again find that the growth rate and frequency are only slightly modified in comparison with the tokamak case.

Conclusion : The complete 3D model has been successfully validated in straight helical geometry and has permitted the first simulations of unstable global ITG modes in non-axisymmetric toroidal configurations. In these results, the effect of the helical deformation of the boundary on the growth rate and the frequency has, however, turned out to be weak. Further work will investigate the properties of other 3D geometries, particularly in quasi-symmetric configurations.

This work was partly supported by the Swiss National Science Foundation. The computations have been performed on the CRAY T3E of the Joint Computing Center of the Max Planck Gesellschaft and the IPP in Garching.

References

[1] G. Jost *et al*, in Theory of Fusion Plasmas, Proc. Int. Workshop Varenna, (1998).

[2] M. Fivaz *et al*, Comp. Phys. Comm. **111** (1998) 27.

[3] L. Villard *et al*, in Theory of Fusion Plasmas, Proc. Int. Workshop Varenna, (1998).

[4] S. P. Hirshman and D. K. Lee, Comp. Phys. Comm. **39** (1986) 161.

Stability Margins of Elongated Plasmas in TCV and Implications for ITER

J.B. Lister, F. Hofmann, Y. Martin, J-M. Moret, P. Vyas

Centre de Recherches en Physique des Plasmas,
Association EURATOM-Confédération Suisse,
Ecole Polytechnique Fédérale de Lausanne, CH-1015 Lausanne EPFL, Switzerland

ABSTRACT

During the operation of the TCV tokamak an extremely wide variety of plasma shapes has been controlled with elongations up to κ=2.5, beyond the present designs for ITER. The operational regime explored by TCV is summarised in this paper using a representative sample of discharges. The growth rates for these discharges were estimated using a rigid current displacement model. The Poloidal Field coil voltages required for plasma control, using the slow external coils and the fast internal coils have also been inspected.

Introduction: The TCV tokamak has an extremely flexible plasma shaping system [1] allowing a wide range of plasma equilibria to be studied. These equilibria are mostly controlled using the MGAMS algorithm [2]. The operational range exceeds that of the RTO/RC ITER designs. The use of internal coils is also a feature which is being explored for some ITER designs. In view of this interest, we have re-visited the TCV operational space to determine which ranges of plasma parameters are accessible.

Data sampling: During TCV operation, a full plasma equilibrium is reconstructed by the LIUQE algorithm [3] every 50 milliseconds. The complete database of TCV reconstructed equilibria comprises 133991 samples. To generate a representative sample with a manageable size and uniform density, avoiding clusters of "popular" standard equilibria, a novelty filter was defined by the Euclidean distance between the PF current vectors constructed from the 16 PF shaping coil currents at each equilibrium, selecting the equilibria by the PF currents which created them, rather than by the resulting geometry. The discharges were sampled backwards in time to retain preferentially the most recent data. A minimum permitted distance was defined, which reduced the sample to 5139 representative points. A reduced database of these equilibria was then created, including all geometrical information on each equilibrium, the PF coil currents and voltages and the parameters of the RZIP rigid current distribution model [4]. These parameters included the current-averaged vertical field, the current-averaged radial field derivative, the instantaneous stabilising restoring force magnitude (Fs) and destabilising quadrupole field force magnitude (Fd), resulting from a unit vertical displacement. The growth rate and the stability margin, defined by m_s = Fs/Fd-1 are also derived. No outliers were removed.

Operational space and disruptivity: The TCV operational space is rather highly dimensioned and only selected cuts can be shown. Figure 1 illustrates the ranges of elongation of the last closed flux surface, κ, and the triangularity of the same surface, δ. Different symbols correspond to different ranges of the plasma current. The extreme values are not necessarily included by the novelty filter, since they are not explicitly included. The highest elongations have been obtained only for a restricted but rather conventional range of triangularity. Highest currents are obtained for significant elongation. Figure 2 shows the variation of κ with q_{95}, the safety factor at the 95% flux surface, with the plasma current ranges indicated. Higher elongations are only obtained for rather low values of q_{95}, typically 2.5 or below.

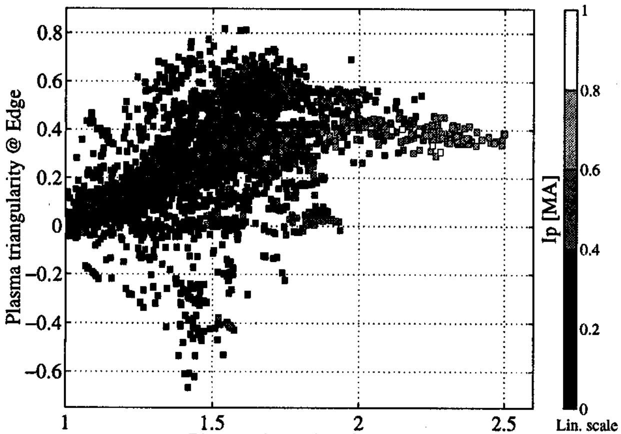

Fig 1 LCFS elongation vs triangularity.

Below an elongation of 1.8, all values of q_{95} are explored. Low elongations are normally not indicated, since the value of q_{95} cannot be estimated for almost circular plasmas. The filtering of the equilibria did not consider whether they disrupted later in the discharge or not; 65% of the discharges were non-disruptive and 95.2% of the equilibria were taken at least 30 milliseconds before a disruption, typically many tens of growth times of the vertical instability. These equilibria can therefore be considered as normally controlled. Figure 3 presents a histogram of q_{95} for the representative equilibria, showing regular operation down to q_{95}=2. More samples are shown between q_{95}=2-3 than for 3-4, corresponding to a greater range of absolute values of plasma current. A minimum around q_{95}=3 is traditional, shown by the lower histogram containing the distribution of the equilibria with a disruption occurring within 30msec of the sample. This latter distribution does not show any pronounced effect close to q_{95}=3 and until q_{95} approaches 2.0.

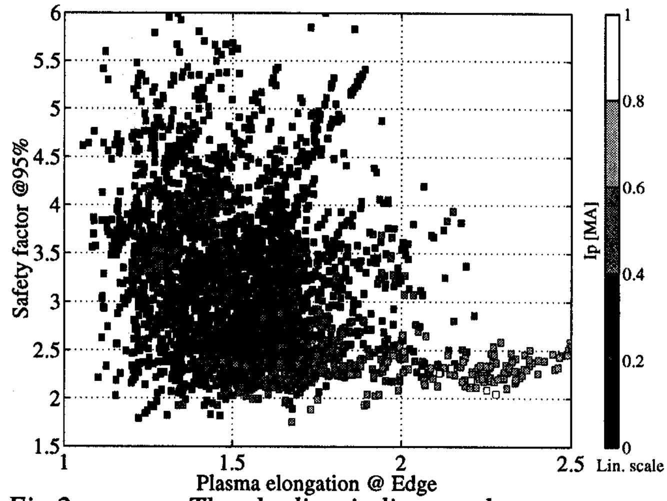

Fig 2 κ vs q_{95}. The shading indicates plasma current.

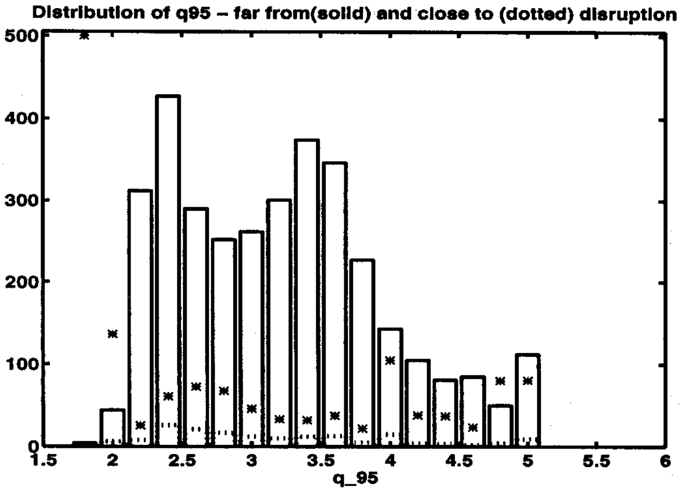

Fig 3 Histogram of q_{95}, showing regular operation down to q_{95}=2. The solid line shows equilibria more than 30 milliseconds from a disruption and the dashed line shows those closer to a disruption. The asterisks show the percentage of samples close to a disruption (x10).

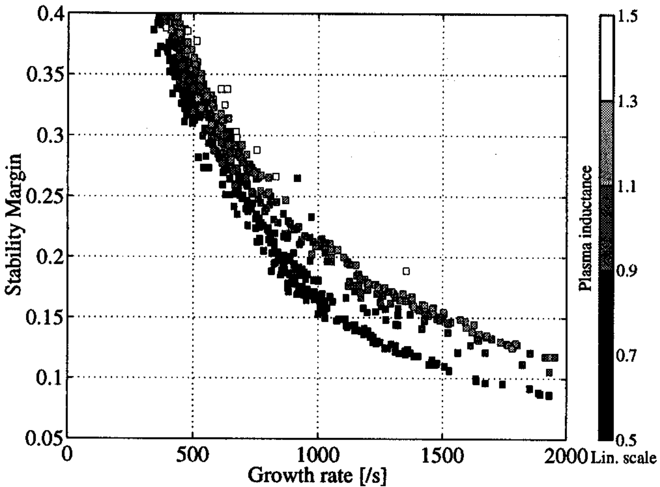

Fig 4 Vertical instability growth rate vs stability margin.

Stability margins: Figure 4 illustrates the variation of the vertical instability growth rate with the stability margin. If the time-constant of the passive structures were fixed, then the growth rate would be a simple function of the stability margin. The thickness of the observed distribution is due to the fact that the restoring force is provided by different parts of the passive structure, depending on the position and on the distribution of the plasma current. The dominant effect is the plasma current distribution, indicated by the symbol variation of Fig. 4, corresponding to different values of the internal inductance, li [5]. The value of the stability margin estimated by the RZIP model drops to around 0.08 at minimum, the estimated restoring force always being calculated as larger than the estimated destabilising force in the model. The fact that m_s does not reach zero can be attributed to the imprecision of the RZIP model, to the finite voltage and bandwidth of the power supplies, or to the controller, or to plasma transients such as sawteeth, provking variations in m_s. Figure 5 illustrates the variation of the same stability margin for different values of κ_{95}. The different symbols correspond to different values of internal inductance. The highest elongations require the lowest internal inductance in order to have reasonable stability margins.

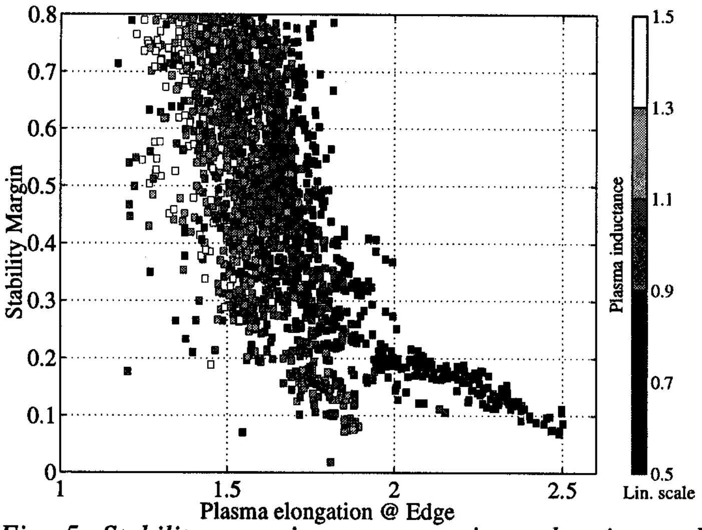

Fig 5 Stability margin vs κ against the internal inductance.

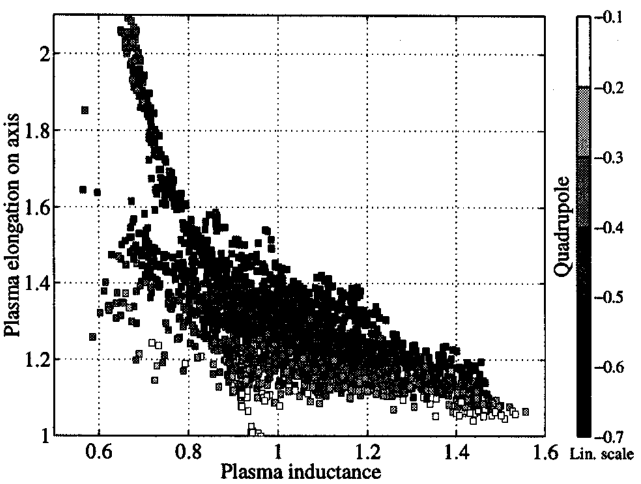

Fig 6 Elongation on axis vs internal inductance against the quadrupole field.

Figure 6 shows the relationship between the elongation on axis, internal inductance and applied quadrupole field averaged over the current distribution and normalised by the plasma current (MA). The tendency is for a drop in inductance to lead to an increase in elongation, however the highest elongations actually have a lower

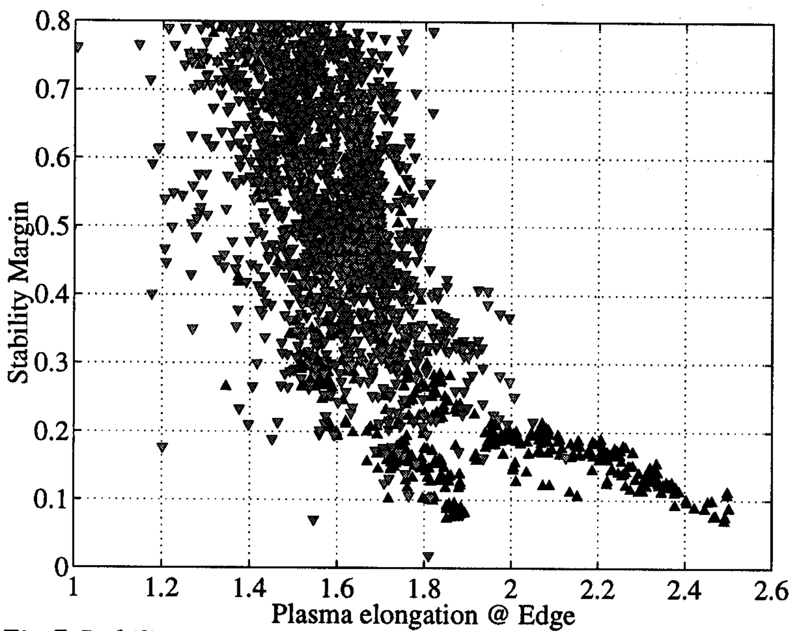

Fig 7 Stability margin vs κ against the RMS voltage on the internal coils. Down grey triangles use only external coils./

averaged quadrupole field. The edge elongation shows a less regular dependence on the two parameters. These effects are probably due to a more important role of higher structural components of the vacuum field and of the precise details of the plasma current distribution as the elongation is increased, under exploration.

The most unstable plasmas in TCV are stabilised using feedback applied to radial field coils placed inside the vacuum vessel [6], to increase the speed of response to vertical movement. Figure 7 shows the same data as Fig. 5, but marking the equilibria according to the root-mean-squared voltage applied to these coils, averaged over the 30 milliseconds preceding the sample. The equilibria with little use of the internal coils (downward triangles) fill the region of lower elongation (κ<2) and higher stability margin (m_s>0.2). The equilibria obtained making use of the internal coils extend the elongation and the stability margin towards 2.5 and 0.08 respectively (upward-triangles).

Conclusions: An implication for ITER is that the reduction of the stability margin for the different reduced cost designs, from above m_S=1.0 for the FDR design to around m_S=0.5 for the current designs, should not correspond to any significant increase in the difficulty of controlling these plasmas, such stability margins being well controlled by the outside coils. There should be no increase in the probability of disruptions due to the problems of control, although disruptions at very low stability margins might become serious. The question of increasing the elongation and the growth rates does not, therefore, only depend on the value of the reduced stability margin.

Acknowledgements: The support of the TCV is warmly acknowledged in this work which was partly supported by the Fonds national suisse de la recherche scientifique.

References:

[1] J.B. Lister et al., Fusion Technology, 32 (1997) 321
[2] F. Hofmann et al., EPS conference, Bournemouth, 1995
[3] F. Hofmann et al.,Nuclear Fusion 28 (1988) 1871
[4] A. Coutlis et al., Nuclear Fusion (1999) in press
[5] D.J. Ward et al., Nuclear Fusion 33 (1993) 821
[6] F. Hofmann et al., Nuclear Fusion 38 (1998) 399

Experimental Determination of the ECH Power Deposition Profile in TCV

A. Manini, J.-M. Moret, I. Furno

Centre de Recherches en Physique des Plasmas
Association EURATOM - Confédération Suisse
Ecole Polytechnique Fédérale de Lausanne, CH-1015 Lausanne EPFL, Switzerland

Introduction

Good knowledge of the ECH power deposition profile is essential for the experimental study of heated plasmas (energy and particle transport, magnetic confinement stability), for profile tailoring, current drive, as well as for the verification ECH ray tracing codes. In TCV this is complicated by the combination of a large variety of plasma shapes (elongation < 2.56, -0.7 < triangularity <+0.5, to date) and a versatile ECH launching system (ultimately 9 beams, 6 at the second harmonic with independent poloidal and toroidal launching angles and 3 at the third harmonic with independent poloidal launching angles). The dynamic response to ECH power perturbations of the electron temperature inferred from soft X-ray emissivity and diamagnetic measurements is used in this paper to examine the ECH deposition. The deposition can be examined with different modulation waveforms: sinusoidal at high frequencies (70Hz to 500Hz) to diminish the effect of transport; random binary signal (RBS) to diminish the effect of coupling with the sawteeth; the response at power turn on and off. The pollution of the X-ray response from the component due to the sawtooth instability, which usually makes analysis difficult, has been treated using a Generalized Singular Value Decomposition (GSVD) technique. This study is thus not restricted to non sawtoothing discharges but covers the whole plasma current capability of TCV.

Experimental set up

The dynamic response of the plasma to ECH power perturbations has been performed in a relatively simple experimental scenario. A "typical" TCV plasma has been chosen with an elongation of 1.6, a triangularity of 0.3 and a density of $\sim 1.5\times10^{19}$ m^{-3} and a single gyrotron was used (P_{max} = 500 kW). The following steps were performed:

- the effectiveness of the sawteeth suppression with the GSVD was tested using discharges with low (Ip = 260 kA, q ~ 4.5) and high plasma current (I_p = 400 kA, q ~ 2.5).
- the dependence of the dynamic response at different ECH deposition locations was examined; the vertical position of the magnetic axis was modified instead of the ECH launching angle to reduce the refraction effects resulting from a small incident angle between the EC waves and the plasma flux surfaces.
- the frequency dependence of the plasma response was investigated using square wave power modulation at 5 frequencies during each plasma discharge.

Description of the analysis procedure

Figure 1 shows an outline schematic of the analysis procedure. The soft X-ray emissivities, integrated along their lines of sight, are analysed with the GSVD to separate the sawteeth and the power modulation contributions (MECH). The GSVD decomposes the signals providing a set of topos (spatial eigenvectors) and their corresponding chronos (temporal eigenvectors). This method involves filtering in phase space, as opposed to regular linear filtering, which only works if the noise and the dynamics of interest have sufficiently different power spectral densities [1]. Discharge periods are chosen in which there are only sawteeth contributions and others with sawtooth and MECH contributions. The GSVD, which has been simultaneously applied to both periods, gives base function common to both which optimises the representation of the MECH whilst diminishing the sawtooth contribution. A frequency analysis of the chronos is used to verify the sawteeth component elimination and the selection of the topos and chronos relevant to the MECH. The selected topos are submitted to a tomographic inversion [2], and the chronos are analysed with a Modified Fourier Transform Method (MFTM). The electron temperature is composed of a modulation contribution superimposed on signals caused by changes in the main plasma parameters. The goal is to simultaneously eliminate the base signal and to extract the complex amplitudes of the harmonics of the modulation frequency through Fourier analysis [3]. A decomposition, using the same procedure, of the reference power signal is used to determine the relative response of each harmonic. The relative responses and the inverted topos are then recombined to obtain the amplitude and phase profiles. Maxima in the amplitude profiles and minima in the phase profile indicate the power deposition location.

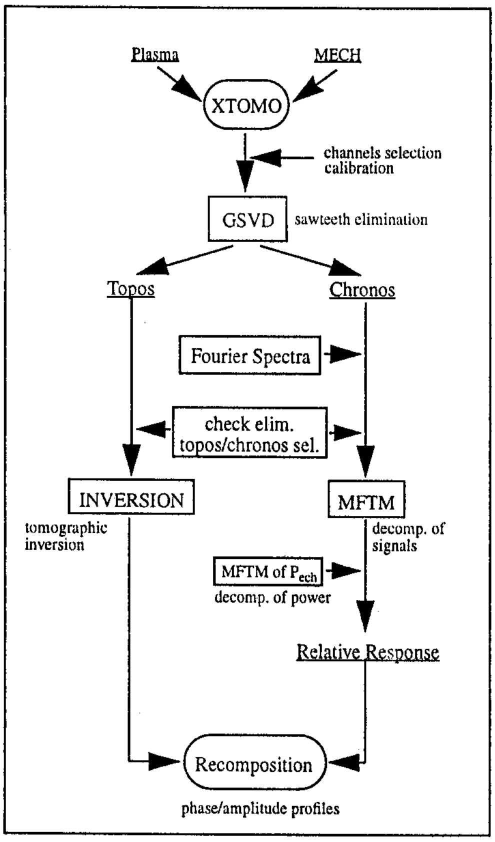

Figure 1: procedure scheme.

Results

The effectiveness of the GSVD was studied using a range of plasma and ECH parameters and different input signal normalisation procedures. A discharge window with 6 to 8 sawteeth periods during the ECH, but before ECH modulation, was chosen as the reference. The best decoupling between the sawteeth and MECH components was obtained with a normalisation where the raw signals were divided by their mean values.

Figures 2 and 3 show an example of the separation that was obtained. Figure 2a shows the Fourier spectrum of a raw signal. The peaks at 71Hz and 214Hz are the 1st and 3rd harmonic of the MECH, at 330Hz the sawteeth, at 400Hz the 1st harmonic coupling between sawteeth and MECH, at 1350Hz the electrical pickup, at 1020Hz the coupling between electrical pickup and sawteeth. Figure 2b shows the spectrum of reconstruction of the same signal using the first 5 topos and chronos of the GSVD. Not only has the sawteeth dependent component been strongly reduced, but the coupling between sawtooth frequency and MECH was also reduced. The first three odd harmonics of the modulation are now evident.

Figure 3 shows signals corresponding to lines of sight passing through three different plasma regions. Figure 3a and 3b show respectively reconstructions using 1 3 5 and 7 topos/chronos for discharges with a square 71.4Hz and 166.7Hz ECH power modulation. At 166.7Hz the number of topos/chronos that can be used in the reconstruction is reduced by the proximity of the sawtooth frequency whereas modulation at lower frequencies has the disadvantage of being more strongly influenced by energy transport. A compromise is required which must be verified for a range of experimental conditions. The GSVD has the advantage of reducing the computation required for tomographic inversion of the reconstructed signals since only a few topos are inverted which cover the whole analysis period.

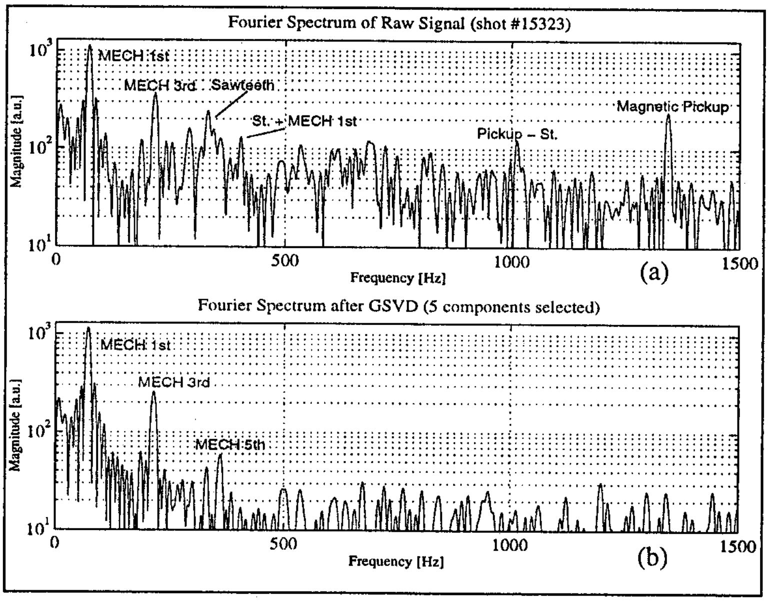

Figure 2: Fourier spectrum before (a) and after (b) GSVD (selected 5 components).

The selected chronos and the reference power signal are then decomposed with a MFTM. The complex relative response is calculated for the first n odd harmonics of the Fourier decomposition of the modulation frequency.

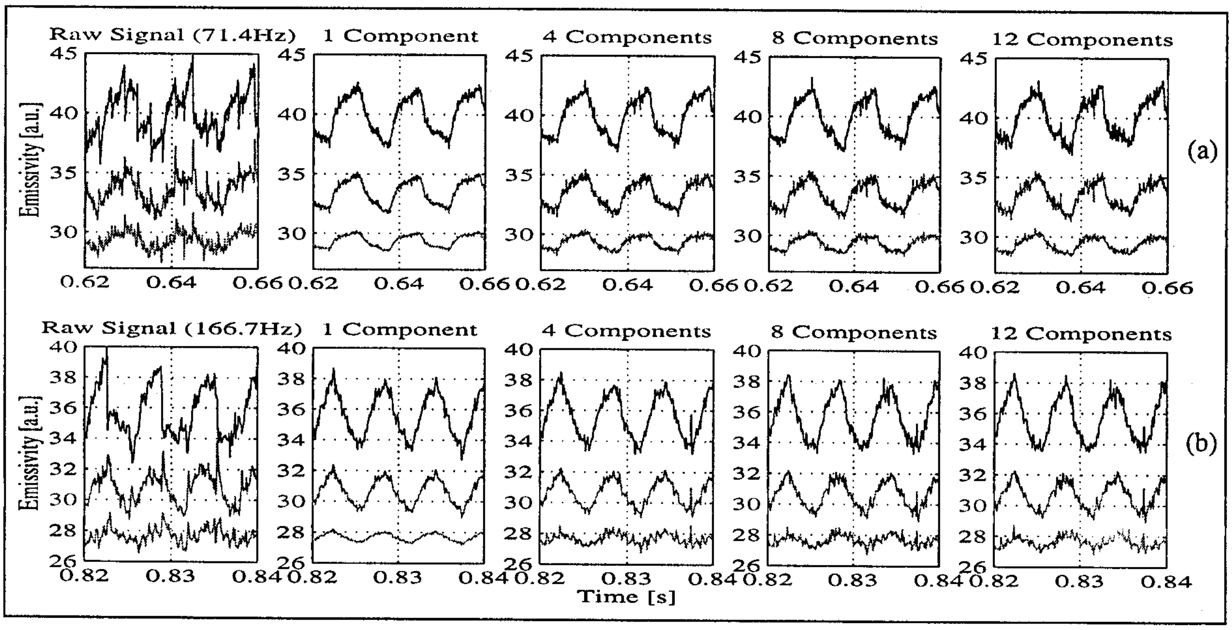

Figure 3: checking the sawtooth elimination for signals at different radii (low (a) and high (b) frequencies modulations, ν_{mech}=71.4Hz and ν_{mech}=166.7Hz).

Finally, the topos are inverted by means of Minimum Fischer Regularization, [2]. Inverted topos and harmonics of the relative response of the chronos are then recomposed to obtain the amplitude and phase profiles of the X-ray intensity response to ECH modulation.

Figures 4a and 4b show an example of results of this procedure for discharge #14990 in which ECH was aimed at the plasma core and the reconstructed X-ray profiles clearly indicate

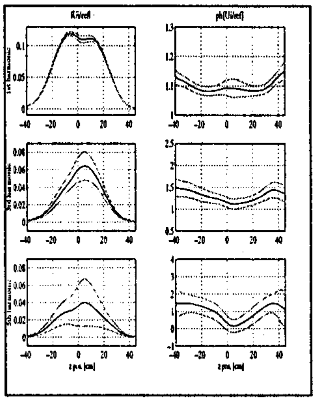

Figure 4a: amplitude and phase profiles.

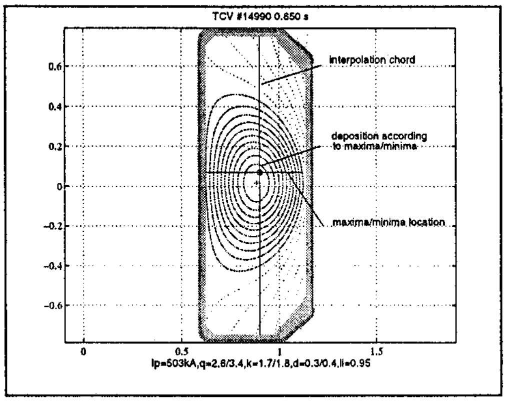

Figure 4b: power deposition according to the profiles.

central power deposition. There are, however, cases in different discharges where there is only partial or sometimes no agreement with the ECH aim. Further studies are required to improve the procedure and interpret the resulting amplitude and phase profiles.

Conclusion

The dynamic response of the plasma of TCV in the presence of modulated ECH has been investigated in order to localise the power deposition profile. Suppression of the coupling between the contributions in the X-ray intensity from the sawtooth instability and the ECH modulation has been achieved using the GSVD method which was otpimised by choosing a mean-subtraction normalisation. The quality of the separation was found to depend on the choice of discharge time windows used in the analysis, the diode viewing chords and the modulation frequency. The MFTM has been successfully used in the frequency decomposition of the selected chronos and has been verified to correctly reconstruct the chronos themselves. The spatial emissivity distribution was shown to be well reconstructed with a tomographic inversion of a limited number of topos terms. The next step will require an optimisation of the MFTM with respect to the modulation frequency for the different types of discharges, in interpreting the results obtained from the amplitude and phase profiles and in applying other ECH power perturbations, in particular RBS.

Acknowledgments

This work was partly supported by the Swiss National Science Foundation.

Bibliography

[1] T. Dudok de Wit et al., Phys. Plasmas **5** (1998) 1360-1370
[2] M. Anton et al., Plasma Phys. Control. Fusion **38** (1996) 1849-1878
[3] J.-M. Moret et al., Nuclear Fusion **32** (1992) 1241-1259

L-mode to H-mode Transitions with ECH in TCV Plasmas - First Results

Y.R. Martin, T.P. Goodman, M.A. Henderson,
J.-P. Hogge, J.-M. Moret and H. Weisen

*Centre de Recherches en Physique des Plasmas,
Association EURATOM - Confédération Suisse,
Ecole Polytechnique Fédérale de Lausanne, CH-1015 Lausanne, Switzerland*

INTRODUCTION

A high power ECH system is currently being installed on TCV ($R=0.88m$, $a\leq0.25m$, $Ip\leq1MA$, $B\leq1.5T$, $1\leq\kappa\leq2.56$, $-0.7\leq\delta\leq0.9$). The heating system now consists of 3 gyrotrons each with a maximum power of 0.5MW. The EC power (82.7GHz) can be launched with any polarisation from X2- to O2-mode and the mirrors at the end of the wave launchers can be adjusted to get the wave power deposition at the requested vertical position. In these experiments, the deposition regions were chosen such as to obtain a smooth power distribution along the plasma minor radius. The radial position of the resonance corresponds to the major radius of the plasma for the nominal field. Therefore, toroidal magnetic field scans are unfortunately not possible, although highly desirable for the LH transitions studies. With this EC frequency and magnetic field, the cut-off density lies at 4.25 $10^{19}m^{-3}$.

Although Ohmic H-modes are regularly obtained in a wide variety of TCV plasmas (limited or diverted, single null or double null, $3<n_e<9\ 10^{19}m^{-3}$, $1.1\leq B\leq1.5$, $1.05\leq\kappa\leq2.05$, $-.2\leq\delta\leq0.7$, $2.05\leq q\leq4$), LH transitions were only rarely observed in low density plasmas ($n_e\leq4\ 10^{19}m^{-3}$). Thus, the first goal of these experiments was to find out whether the H-mode was accessible with a low density ECH target plasma.

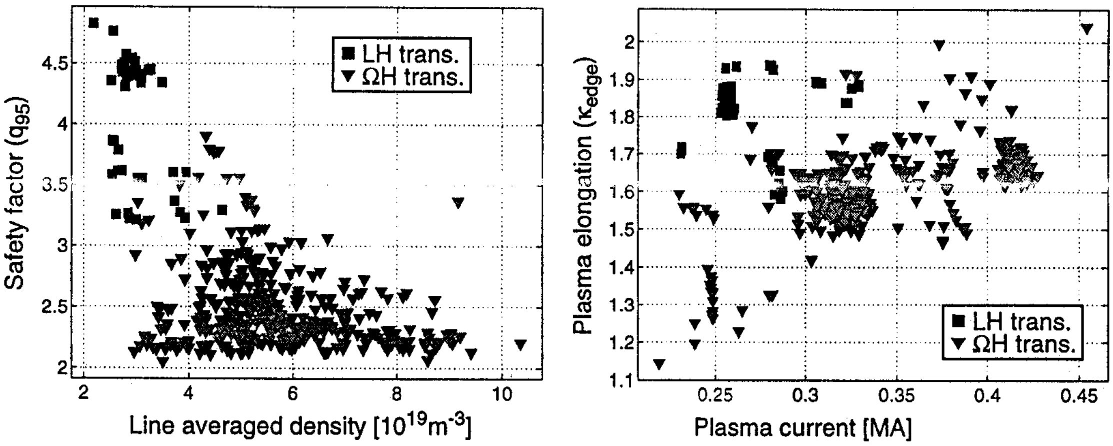

Figure 1: Operational Domain where LH transitions were obtained both for ECRH (■) and Ohmic heating (▼)

OPERATIONAL DOMAIN FOR LH TRANSITIONS IN ECH PLASMAS

The range of stationnary plasma parameters suitable for ECH injection was found to be rather small. The appearance of fatal modes occuring when crossing of $q_{95}=3$ and 4 in low density plasmas implied operation at higher q_{95} which is at the limit for vertical stability of highly elongated plasmas. Nevertheless, LH transitions have been obtained in this region of the operational domain. Moreover, the low density limit for ohmic H-mode accessibility is lowered when ECH power is added. The increased operational domain covered by these transitions is shown in Figure 1, together with the range covered by the ohmic transitions.

These transitions were obtained in discharges with 3 successive ramps of the ECH power while keeping all other plasma parameters constant, as shown on Figure 2. From shot to shot, the transitions occured at different values of injected ECH power, depending on the plasma parameters. In order to determine the relationship between the amount of additional power and the plasma parameters at the LH transition, the estimation of the power absorbed by the plasma must be addressed.

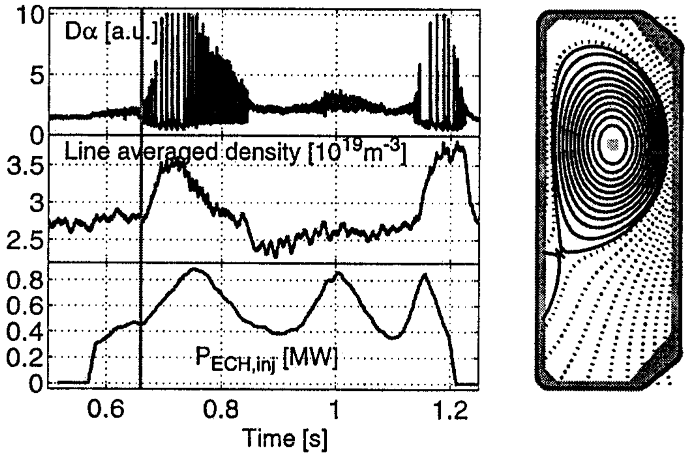

Figure 2: Time evolution of a discharge with a LH transition induced by the ECH power. The poloidal cross section shows the plasma shape at the LH transition indicated by the vertical line.

ESTIMATED ABSORBED ECH POWER INTO THE PLASMA

For all 3 gyrotrons, the ECH power injected in the plasma is measured near the end of the wave guides with 10% accuracy. However, the density profiles measured by Thomson scattering show a central plasma region, up to ρ=0.5, with a local density above the cut-off density for a line average density of 3.5 $10^{19}m^{-3}$. This implies a significant refraction of the beams and possibly the loss of the first pass absorbtion at the resonance location. Power not absorbed on the first pass will either be absorbed in the plasma after many reflections, absorbed by the walls covered by Carbon tiles or leave the torus through the ports.

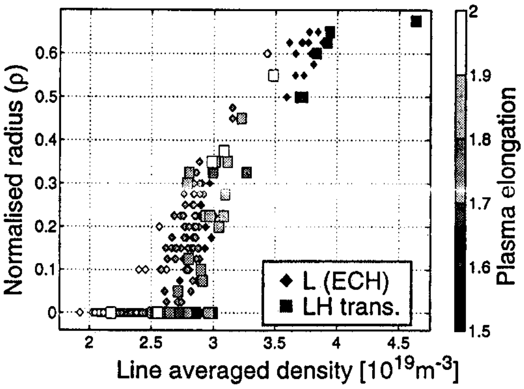

Figure 3: Normalised minor radius (ρ) of the plasma where the density equals the EC cut-off density as a function of the line averaged density.

To estimate the first path absorbtion, a 3D ray tracing code, TORAY, has been used [1]. From the knowledge of the plasma shape, the ECH injection geometry, the density and temperature profile, this code determines the trajectory of the beams in the plasma and calculates the fraction of the power which is deposited at the resonance for each beam.

Although the launcher angles were adjusted to direct the beams mostly to large ρ's, the absorbed power in the first path was as low as 20% (n_e> 3.5 $10^{19}m^{-3}$). It is important to determine what fraction of the power not absorbed on the first pass is absorbed in the plasma. For these first experiments with similar shapes and density profiles, a simple model was used consisting of a simplified ray tracing code where the beam reflects at the wall and the plasma. At each interaction a fraction of the power is absorbed depending on the nature of the reflection: wall, window, absorbing or refracting plasma. The absorbtion coefficient of the wall is based on an empirical value of the reflexion of the wave on Carbon tiles. The effect of a variation of this parameter around the experimental value of 0.95 is more important than the fraction of refracting plasma. By means of this model, the absorbed power after multiple reflections was estimated to be about 50% on average for these shots. Hence, the absorbed ECH power can be expressed, for these experiments, as

$$P_{ECH,abs} = P_{ECH,inj} * A_{toray} + P_{ECH,inj} * (1-A_{toray}) * 0.5$$

In order to test the validity of the models used for the estimation of the absorbed power, the O2 polarisation of the waves was used in two otherwise identical discharges previously heated with the X2 polarisation. LH transitions occured with both polarisations of the waves and, once corrected using the above model, the absorbed ECH power at the LH transitions agreed within 10 %, which is a first confirmation of the modelling.

Figure 4 shows the relationship between the line average plasma density and the absorbed ECH power as defined previously. The ECH power at the LH transition clearly increases as the plasma density falls, although the scatter in the data is quite large. One cause of the scattering in the range of density between 2.5 and 3 $10^{19}m^{-3}$ originates in the dynamics of the ECH power injection: if the transition does not occur in the first 100 ms of the heating phase, it may occasionally happen later but a higher ECH power is needed for the same values of the controllable plasma parameters. In some cases no LH transition is encountered. In these cases as well as at lower densities (n_e<2.5 $10^{19}m^{-3}$), the central electron temperature is found to increase above 1.2keV. Above this temperature, no LH transition was observed. One possible link is a decrease in the coupling of the electron and ion populations. The value of the central plasma temperature could even be used

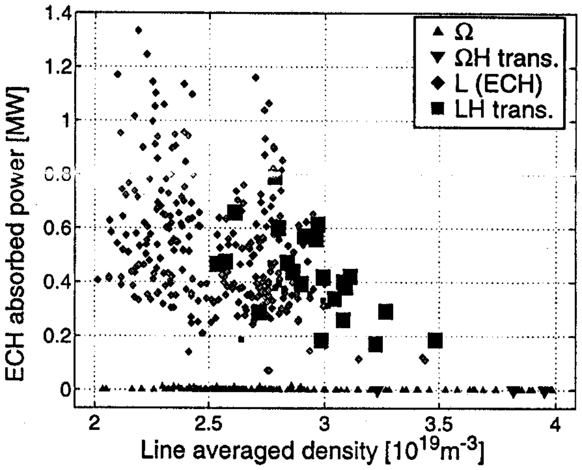

Figure 4: ECH Threshold power as a function of the plasma line averaged density

as an indicator of the possibility to get a LH transition.

Therefore, in order to reduce this scattering in the data, only the LH transitions occuring shortly after the beginning of the heating were selected. With this reduced set of transitions the dependence of the total absorbed power, $P_{OHM} + P_{ECH}$, on the plasma density is even clearer as shown on Figure 5. It is worth noting that this dependence estimated as $P_{thresh} \alpha n_e^{-1.5}$ is in contradiction with the ITER power law scaling where the threshold power increases as the density increases: $P_{thresh} \alpha n_e^{0.67}$ [2]. However, such a negative dependence of the power on the plasma density was already observed on COMPASS, where the LH transitions were obtained with ECH power too [3]. These observations on two different tokamaks tend to confirm the discrepency between heating schemes acting on the ions or on the electrons, in terms of H-mode accessibility.

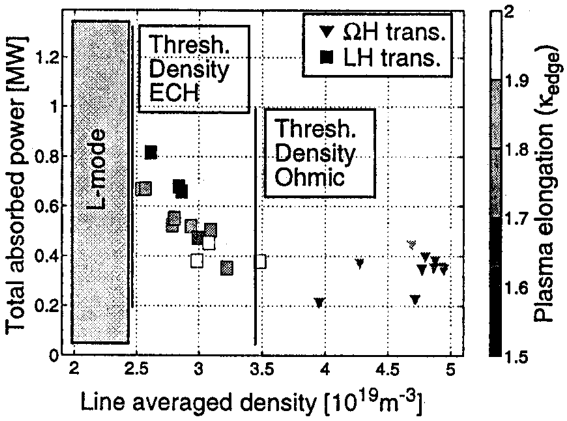

<u>Figure 5</u>: LH transition threshold power in ohmic (▼) and ECRH (■) heated discharges.

In this reduced set of LH transitions, the plasma elongation seems to have a little influence on the threshold power. However, changes in q95 also occured among these discharges. Therefore, more experiments are required to decouple the effect of the elongation from the effect of the current profile.

CONCLUSION

LH transitions have recently been obtained in EC heated plasmas in TCV. They were observed in a range of low density and high q_{95} values where ohmic LH transitions were never achieved. As already noticed in the ohmic case, although at a higher density, a low density threshold was found at approximatively 2.5 $10^{19}m^{-3}$ for the additionally heated discharges. In these experiments the LH threshold power was found to increase as the plasma density decreases. This strong negative dependence is in contradiction with the ITER threshold power scaling [2]. The plasma shape has not show any significant influence on the LH transition with ECH so far.

AKNOWLEDGMENT

This work was partly supported by the Swiss National Science Foundation.

REFERENCES

[1] G. Smith, L.D. Pearlstein, A.H. Kritz, et al. Proc. 9th Joint Workshop on ECE and ECH, Borrego Springs, January 1995,World Scientific (1995) 651.
[2] K. Thomsen et al. IAEA 1998, IAEA-F1-CN-69/ITERP1/07.
[3] A.W. Morris, IAEA 1998, IAEA-F1-CN-69/EXP2/04.

Divertor Detachment in TCV Ohmic Plasmas

R. A. Pitts, B. P. Duval, J.-M. Moret, M. E. Fenstermacher[1], A. Loarte[2],
W. H. Meyer[1], J. Mlynar, A. Refke, J. Rommers

Centre de Recherches en Physique des Plasmas
Association EURATOM - Confédération Suisse
École Polytechnique Fédérale de Lausanne, CH-1015 Lausanne, Switzerland
[1]Lawrence Livermore National Laboratory, P.O.Box 808, Livermore, California 94550, USA
[2]EFDA-CSU, Max-Planck-Institut für Plasmaphysik, D-85748 Garching, Germany

INTRODUCTION

Quantifying the effect of divertor geometry on main plasma performance and its influence on the characteristics of the divertor plasma itself constitutes an important element of current research towards an integrated solution for future reactors based on the tokamak concept. Although it is clearly preferable to perform such research in large machines [1] under conditions as close as possible to those expected in next step devices (high power, long pulse, etc), experiments in smaller, more flexible facilities can offer interesting insights into the basic phenomena occurring. Despite its small size, the possibility for plasma shape variation in TCV permits the creation of magnetic equilibria allowing the detached divertor state to be accessed, even in completely open geometries. This contribution presents selected results from the first experiments of this nature on TCV.

VARIABLE DIVERTOR GEOMETRY

In the present absence on TCV of additional heating suitable for high density operation, all experiments have been performed with ohmic heating alone and have used only D_2 gas fuelling from a single injection point in the vacuum vessel floor. Figure 1 illustrates three from a range of equilibria produced thus far and designed to investigate the effects on detachment, if any, of varying flux expansion for fixed X-point height and varying X-point height at approximately constant flux expansion. The table below describes the differences between the example equilibria of Fig. 1 in terms of magnetic geometry relevant to the divertor. Here, z_{Xpt} refers to the height of the X-point with respect to the lower divertor target tiles, L_{cmp}^{out} is the approximate magnetic connection length from outer midplane to outer divertor strike point and f_e^{out} is the flux expansion at the outer strike point (measurements on TCV are currently available only at the outer strike zone in these types of configuration). Also given are the connection lengths from X-point to

Shot	I_p [kA]	z_{Xpt} [m]	f_e^{out}	L_{cmp}^{out} [m]	L_{cxp}^{out} [m]
15445	340	0.57	6.8	29	21
15448	340	0.57	2.8	20	15
15521	340	0.28	2.2	13	9
15527	380	0.28	2.0	11	7

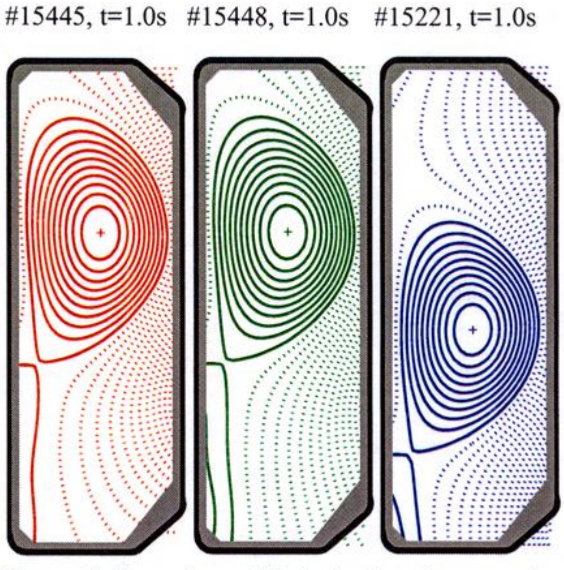

***Figure 1**: Example equilibria for detachment study illustrating large and small X-point height and low and high flux expansion at high poloidal depth. See the table alongside for more details.*

outer target, L^{out}_{cxp} for $t = 1.0$ s. These values highlight an important aspect of these TCV plasmas - a *substantial fraction* of L^{out}_{cmp} occurs in passing from X-point to target - the opposite of what is found in more conventional diverted equilibria. The majority of data obtained to date have been for $I_p = 340$ kA. Currents much lower than 300 kA result in too great a fraction of the input power being radiated inside the separatrix at high $\bar{n}_e$ to sustain the divertor plasma, whilst pushing I_p too high often leads to ohmic H-mode transitions and subsequently uncontrollable density increase. It is interesting to note, however, that configurations with low X-point height tend to remain in L-mode, even at higher current. Most experiments to date have been performed for the ion ∇B drift direction away from the X-point in the equilibria of Fig. 1.

EXPERIMENTAL OBSERVATIONS

The approach to detachment and the detachment itself are studied using density ramp discharges, frequently terminating at the density limit for the chosen value of I_p (maximum value of $n_{GR} = 0.65$). Figure 2 compiles a selection of plasma and divertor signals for similar ramps in main plasma density for the three equilibria of Fig. 1, corresponding to the discharge numbers listed in the accompanying table. One may immediately note the apparent similarity between the two discharges with identical (high) z_{Xpt} but varying flux expansion and the clear differences in behaviour when decreasing X-point height or

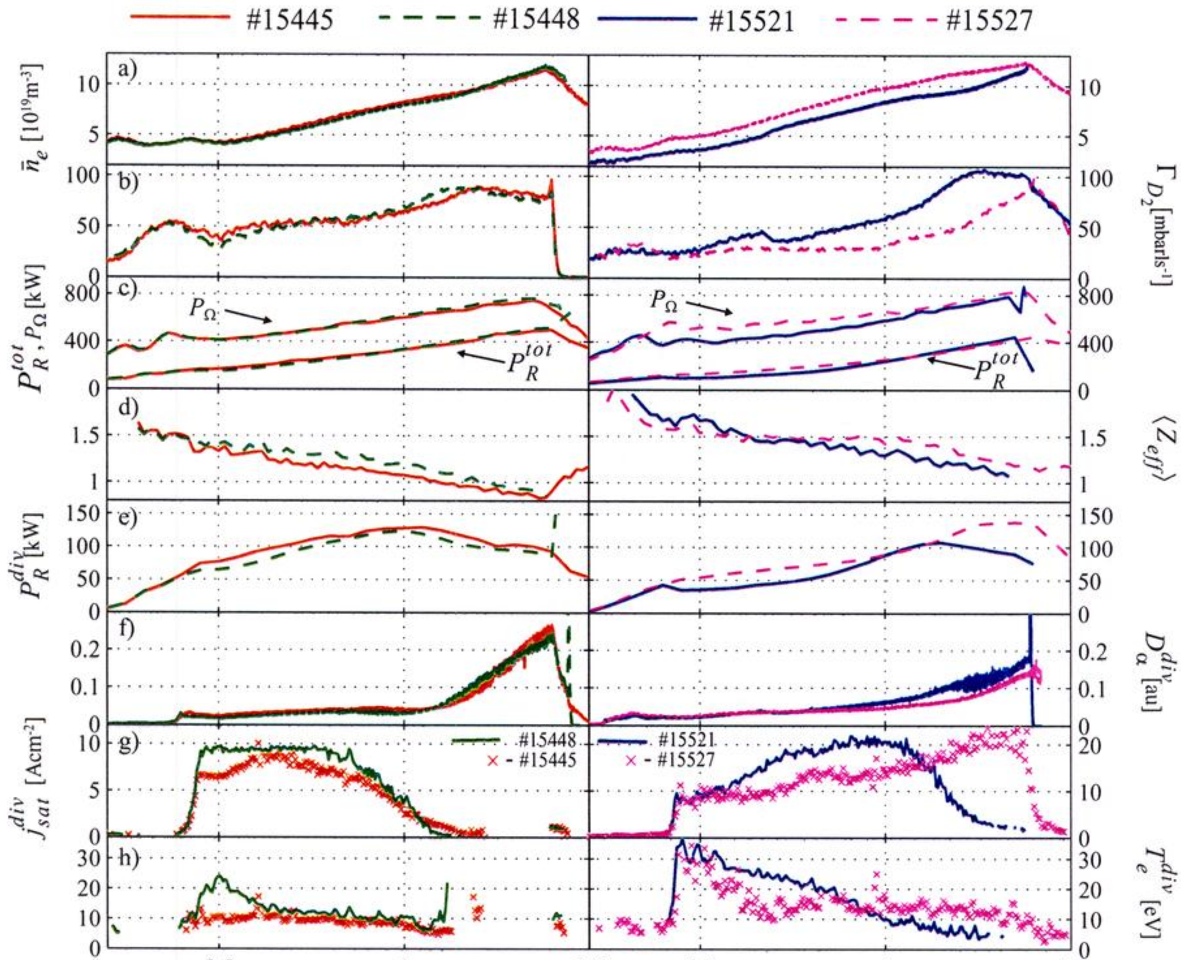

Figure 2: *Evolution of main plasma and selected divertor parameters for the discharges in the Table accompanying Fig. 1 during similar ohmic density ramps. For $z_{Xpt} = 57$ cm, the panels at left show both cases of f_e^{out}. Note the change in scale of the ordinate in the panels containing j_{sat}. The similarity in the D_α traces for shots #15445 and #15448 makes it difficult to discern differences if the figure is not viewed in colour.*

increasing I_p. Independent of divertor geometry, the plasma separatrix shape is approximately constant with κ_{95} and δ_{95} in the range 1.5 → 1.6 and 0.33 → 0.4 respectively with q_{95} in the range 2.2 → 3.2. Earlier studies elsewhere [2] have shown the importance of plasma wall separation in influencing bulk and divertor radiation. Attempts have been made here to minimise such differences, at least in so far as separatrix to wall gaps at the inside and outside midplane are concerned (depending on $\bar{n}_e$, I_p and z_{Xpt}, the distances typically lie in the range 2 → 3 cm). It should also be noted that the interior walls of the TCV vacuum vessel are now almost completely graphite tiled, giving ≈ 90% surface coverage.

In all cases, detachment is clearly observed at the outer strike zone as a decrease in the ion current measured near the strike point by Langmuir probes embedded in the target tiles (Fig. 2g) and an increase in the D_α emission shown, in Fig. 2f, for a chord passing almost horizontally through the divertor leg near the vessel floor. For lower z_{Xpt}, the rollover to detachment occurs at higher plasma density for fixed input power (ie fixed I_p). This is qualitatively expected since increasing L_c^{out} would be expected to facilitate the formation of parallel temperature gradients and hence low T_e in the divertor plasma. For fixed z_{Xpt} but higher I_p, detachment is observed near the strike point only at the highest densities. In all cases, detachment occurs only if $T_e^{div} \approx 5$ eV subject to the usual uncertainty in interpretation of the Langmuir probe characteristic under high recycling conditions. The higher edge T_e at low z_{Xpt} is also reflected in higher values of $\langle Z_{eff} \rangle$ for given $\bar{n}_e$ (Fig. 2d). Of note also are the low values of $\langle Z_{eff} \rangle$ at high $\bar{n}_e$, even when the total radiation reaches ≈ 65% of P_Ω (Fig. 2c) and the divertor plasma detaches. This reflects both the reduced impurity source due to a decrease in divertor temperature and particle flux but also the apparent tendency for $\langle Z_{eff} \rangle$ to depend principally on plasma density and radiation fraction and not the regime of divertor operation [3]. This occurs even when, at detachment, most of the radiation is concentrated at or inside the separatrix at the X-point location. The low $\langle Z_{eff} \rangle$ also indicates that most of the total radiation at high $\bar{n}_e$ originates from deuterium. The traces of T_e and j_{sat} in Figs. 2g,h show that for the discharges at highest z_{Xpt}, the outer divertor plasma has already atttained the high recycling regime, even at low $\bar{n}_e$, whilst as the outer leg shortens, the divertor plasma begins life in the linear regime for the same main plasma density. Figure 3 summarises target plate measurements in terms of the integrated current to the plate surface (accounting for field line angle of incidence) and the peak divertor density, the latter not necessarily occurring in the same flux tube as $\bar{n}_e$ increases. In addition to discharges similar to those of Fig. 2, a few points available

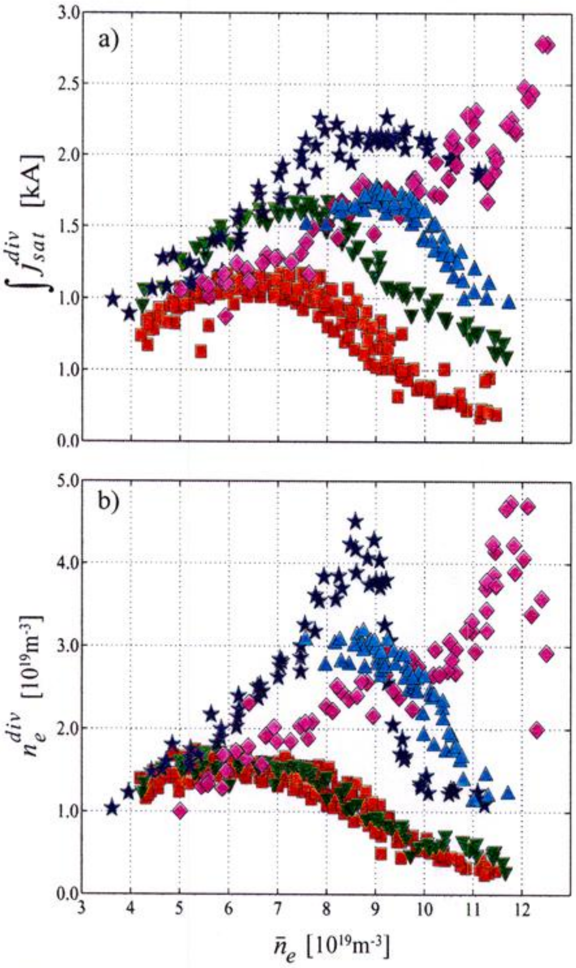

Figure 3:*Density dependence of* ***a)*** *the integrated ion current to the outer divertor target and* ***b)*** *the peak divertor density. Data are compiled from a multi-shot database. Symbols have the following meaning:*
■ $z_{Xpt} = 57$ *cm*, $f_e^{out} \approx 7$, ▼ $z_{Xpt} = 57$ *cm*, $f_e^{out} \approx 3$
▲ $z_{Xpt} = 57$ *cm*, $f_e^{out} \approx 6$, ★, ◆ $z_{Xpt} = 28$ *cm*, $f_e^{out} \approx 2$
■ ▼★, $I_p = 340$ kA, ◆ ▲, $I_p = 380$ kA

at high z_{Xpt} and higher I_p have also been included. For both low and high f_e^{out}, the discharges with high z_{Xpt} show the total ion current decreasing to low values at high density, behaviour typical of complete detachment. The latter is observed at higher $\bar{n}_e$ as L_c^{out} decreases or I_p increases with much higher peak densities being attained in the divertor before detachment as input power increases. At low z_{Xpt}, particularly at $I_p = 380$ kA, the peak divertor density behaves roughly in accordance with the standard two-point model of the SOL [4] in which $n_e^{div} \propto \bar{n}_e$ at first then $n_e^{div} \propto \bar{n}_e^3$ at high density when high recycling is attained. At lower I_p, the maximum divertor density peaks at lower $\bar{n}_e$, as would be expected for lower L_c^{out}, but the density increase with $\bar{n}_e$ is stronger than linear at lower $\bar{n}_e$.

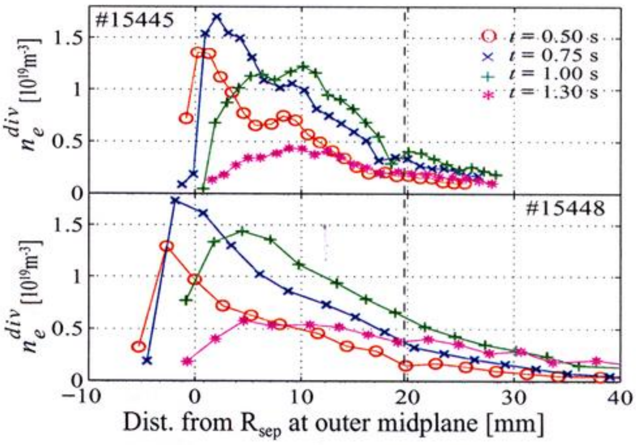

Figure 4: *Time variation of target density profile mapped to the midplane for discharges with* $z_{\text{Xpt}} = 57$ *cm and low and high* f_e^{out}. *The vertical dashed lines indicate the mean position of the outer wall.*

Figure 3 highlights some interesting differences in divertor behaviour for different input power and magnetic geometry. At high z_{Xpt} and I_p =340 kA, the total integrated ion current to the outer target (Fig. 3a) is higher at low f_e^{out}, whilst the peak divertor density (Fig. 3b) appears to be independent of flux expansion (note that the peak n_e^{div} will not always occur on the same flux tube in the divertor). Given the lower values of L_c^{out} for low f_e^{out}, this is not what would be expected from the two point model if the upstream power flow is constant for given $\bar{n}_e$. Target density profiles for the two cases at four times (or values of $\bar{n}_e$) are shown in Fig. 4. The profiles are mapped to the midplane to better illustrate the effects of flux expansion - the latter clearly has a strong effect on the profile shape. Before detachment begins, there is relatively good agreement between magnetically computed strike point and the profile peak. At high f_e^{out}, detachment penetrates further into the divertor fan and there is also faint evidence for some structure in the profile itself, not seen at low f_e^{out}. Profiles of T_e^{div} are remarkably flat and in the range $10 \rightarrow 15$ eV for both flux expansion cases at all but the lowest plasma densities and of course when detachment occurs. The observations at lower I_p are not yet understood. Part of the difficulty is almost certainly associated with low power crossing the separatrix at high density. At $I_p = 380$ kA, Thomson scattering measurements made just inside the separatrix (at a radius corresponding to 95% of poloidal flux) show T_e there to remain roughly fixed with increasing $\bar{n}_e$, except at the very highest densities. In contrast, for $I_p = 340$ kA, the temperature decreases from ≈ 50 eV at low density to only ≈ 20 eV at highest $\bar{n}_e$. This is a consequence of an increasing radiation fraction (Fig. 2c) leading to lower values of upstream conducted power. Under these circumstances, it is unlikely that the condition of $T_e^{up} \gg T_e^{div}$ for electron conduction to dominate parallel heat transport is satisfied and significant convection may occur, leading to departures from the expectations of two-point modelling.

ACKNOWLEDGMENTS

This work was partly supported by the Swiss National Science Foundation.

REFERENCES

[1] L. D. Horton et al., Nuclear Fusion **39** (1999) 1
[2] A. Loarte et al., Nuclear Fusion **38** (1998) 331
[3] G. F. Matthews et al., J. Nucl. Mater. **241-243** (1997) 450
[4] C. S. Pitcher and P. C. Stangeby, Plasma Phys. Control. Fusion **39** (1997) 779

Energy Confinement in Shaped TCV Plasmas with Electron Cyclotron Heating

A. Pochelon, S. Coda, T.P. Goodman, M. Henderson, J-M. Moret,
Ch. Nieswand, Z.A. Pietrzyk, H. Reimerdes, O. Sauter, C. Angioni,
R. Behn, I. Furno, J-P. Hogge, F. Hofmann, B. Joye, N. Kirneva[1],
J.B. Lister, Y. Martin, R.A. Pitts, F. Porcelli[2], J. Rommers, A. Sushkov[1],
M.Q. Tran, H. Weisen

Centre de Recherches en Physique des Plasmas, Ecole Polytechnique Fédérale de Lausanne
Association EURATOM-Confédération Suisse, CH-1015 Lausanne EPFL, Switzerland
[1] *Russian Research Centre Kurchatov, 12182 Moscow, RF*
[2] *Politecnico di Torino, I-10129 Torino, Italy*

Abstract The effects of plasma shape on confinement and sawtooth stability are studied for positive and negative discharge triangularity and for different elongations with 1.5 MW centrally deposited ECH power.

Introduction After extensive studies of Ohmic confinement as a function of plasma shape [1] and initial studies of confinement with additional EC heating at a power level of 0.5-1 MW [2], extensive studies of confinement with ECH started in 1998 at the 1.5 MW power level, using the first cluster of three gyrotrons at second harmonic, 82.7 GHz [3]. During the initial ECH campaign in 1997, the effect of the power deposition location on confinement was studied at low power [4]. The location of the power deposition was obtained from power modulation or power shut-off techniques, from ray tracing and qualitatively from sawtooth shapes [5]. These low power studies confirmed the good confinement properties of power deposited inside the $q = 1$ surface, relative to outside.

Studies of energy confinement time in EC heated discharges have been started as a function of plasma shape in TCV (Tokamak à Configuration Variable, achieved parameters: κ=2.58, $-0.7<\delta<0.9$, I_p=1MA). The elongations and triangularities explored with additional heating to date are in the range $1.1<\kappa<2.15$ and $-0.65\leq\delta\leq0.5$. For these studies, an additional power of 1.5MW ECH is injected at the second harmonic, which typically represents a power ratio of P_{EC}/P_{OH}~2-3 during ECH, up to ten in extreme cases. Central power deposition, well inside the q=1 surface, is used in this campaign as a rule. Two values of the engineering safety factor q_{eng} ($q_{eng} = 5abB/RI_p$= 1.7 and 3) were used ($2.3 < q_a < 6$; $0.2 < I_p < 0.7$ MA). Maintaining q_{eng} constant keeps the normalised radius of $q = 1$ approximately constant while changing the plasma shape [6]. The electron energy content is obtained during stationary periods from repetitive Thomson scattering measurements (~150 Hz), averaged typically over 10 time-slices to reduce the influence of MHD fluctuations.

Confinement Analysis To obtain a simple general power law over the full data set describing the dependence of the electron confinement time τ_{Ee} on average line density n_{e_av}, total power P, edge elongation κ, edge triangularity δ and plasma current I_p, we have applied a multi-variable regression. The dependences on κ and I_p cannot be separately determined, owing to the strong correlation between these quantities in the present data. The power law must therefore contain a free parameter, and takes the following form:

$$\tau_{Ee}[\mathrm{ms}] = 2\; n_{e\_av19}^{\;\alpha_n}\; P^{\alpha_P}\; (6\; I_p)^{\alpha_I}\; \kappa^{\alpha_\kappa}\; (1+\delta)^{\alpha_\delta}\; [\mathrm{m^{-3}, MW, MA}] \qquad (1)$$

with α_n=0.46±0.2, α_P=-0.7±0.1, α_δ=-0.35±0.3, α_κ=1.4(1-α_I)±0.4 and α_I remains undetermined. The uncertainties have been estimated assuming a 25% error on τ_{Ee}. Good fits are obtained with α_I in the range $0 \leq \alpha_I \leq 0.7$, an example at α_I=0.5 is shown in **Fig. 1.**

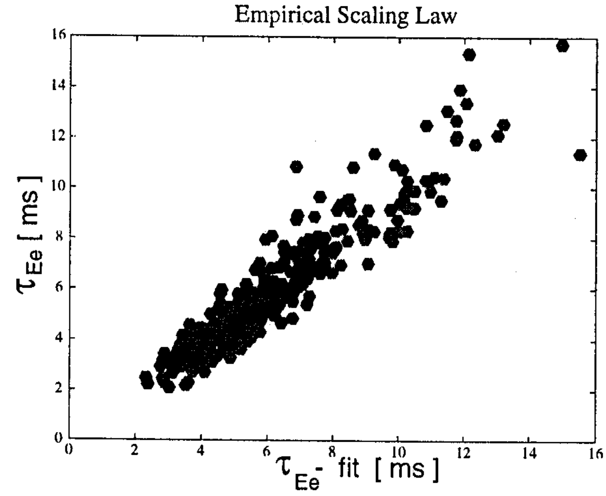

Fig. 1. Empirical scaling law for TCV ECRH data set, see equation (1), in the representative case α_I=0.5.

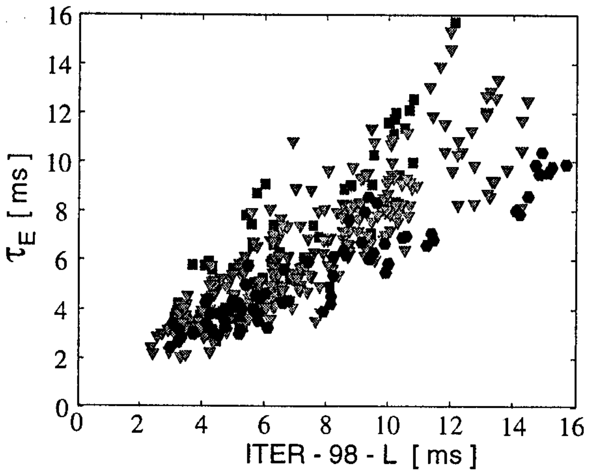

Fig. 2. Fit to ITER-98-L mode scaling law. Since triangularity does not appear in ITER-98-L, it is explicitly indicated by the symbols: negative δ appear favourable (red squares: δ<0, green triangles: 0<δ<0.3, blue hexagons: δ>0.3).

In spite of the unresolved confinement dependence on current and elongation, this scaling appears favourable, as the main motivation for creating elongated discharges is indeed to increase the plasma current with the aim of increasing the energy confinement and pressure limits. Further data are needed at moderate elongation to separate the contributions of plasma current and elongation.

The general scaling (1) displays qualitative similarities with the recent scaling laws found using a multi-tokamak database, such as the ITER-98-L mode scaling, where α_n=0.40, α_P=-0.73, α_I=0.96, α_κ=0.64 [7]. Clearly, the α_n and α_P exponents are in good agreement with our scaling within the uncertainties; however, α_κ and α_I are not both compatible with our scaling. Plotting our data against ITER-98-L highlights the beneficial effect of negative triangularities, particularly at low powers, i.e. at the large confinement times, as shown in **Fig. 2** [3].

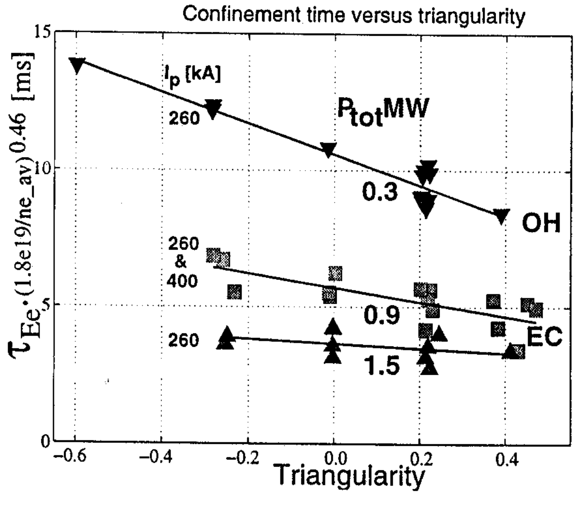

The TCV confinement time in ECRH conditions shows good agreement with the Rebut-Lallia-Watkins critical gradient confinement scaling [3], as already shown earlier for ohmic TCV conditions.

Naturally, the general scaling (1), which is based on the entire data set, overlooks more detailed effects in specific regions of the parameter space.

For instance, in a triangularity scan at κ=1.5 (P_{tot}/P_{OH}~3-9), the confinement time is larger at small or negative triangularities. This effect is particularly visible at low total input power, as shown in **Fig. 3**.

Fig. 3. Triangularity dependence of confinement time for different total power classes with centrally EC deposited power, normalised to $n_{e\_av}=2\times10^{19}\,m^{-3}$ (density range: $1.3<n_{e019}<3$). The power range for the low power 0.3 MW class, the largest, is ±16% wide; the higher confinement at negative triangularity reflects therefore predominantly an effect of plasma shape.

Within the present available power range, it cannot be stated clearly whether the confinement power degradation is more pronounced at negative triangularity than at positive triangularity in these central power deposition conditions. The addition of the second cluster of 1.5 MW will help to see whether the present trend is maintained.

In the same triangularity scan, the β values are also higher at negative triangularities in both ohmic and ECH.

Confinement Transitions In the process of enlarging the database to decouple the I_p and κ dependences in the confinement scaling, we have started to complement the database with elongated low current shots. Very high safety factor discharges (κ~2, I_p~80 kA, q~20) have been successfully produced and are vertically stabilisable. With the gyrotron frequency of 82.7 GHz and the maximal nominal magnetic field of 1.43T, however, the EC resonance is located off-axis on the high field side at mid normalised radius. At the highest injected EC powers, discharges show spontaneous oscillating transitions in confinement, best revealed by changes in the the central soft X-ray emission. Drops in the central soft X-ray emission are associated with a flattening of the density profile reconstructed from the fifteen interferometer channels, presumably triggered by changes in the q-profile with off-axis heating [8].

These transitions raise the issue of the role of high power localised ECH heating in confinement experiments, which can change shear and gradient profiles relative to the ohmic target plasma. Thus, the use of highly localised on-axis heating in these experiments may result in a radial deposition profile very different from its Ohmic counterpart, particularly for highly shaped plasmas, e.g. for strong negative triangularities or high elongations. In negative triangularity discharges, the ohmic power is relatively reduced [1]. The effect of localised/distributed heating needs in fact to be determined experimentally. In the case of counter-ECCD discharges with central deposition, confinement about twice the Rebut-Lallia-Watkins scaling has been measured.

Sawteeth Stability and Plasma Shape The effect of power on the sawtooth period and amplitude was studied in a triangularity scan ($-0.3<\delta<0.5$, q_{eng}~2, $P_{EC}/P_{OH}\leq 3$) and an elongation scan ($1.1<\kappa<2$, q_{eng}~2) while keeping deposition well inside the inversion radius. In these shape scans at constant q_{eng}, the normalised inversion radius measured from soft X-ray tomography varies by less than 5%.

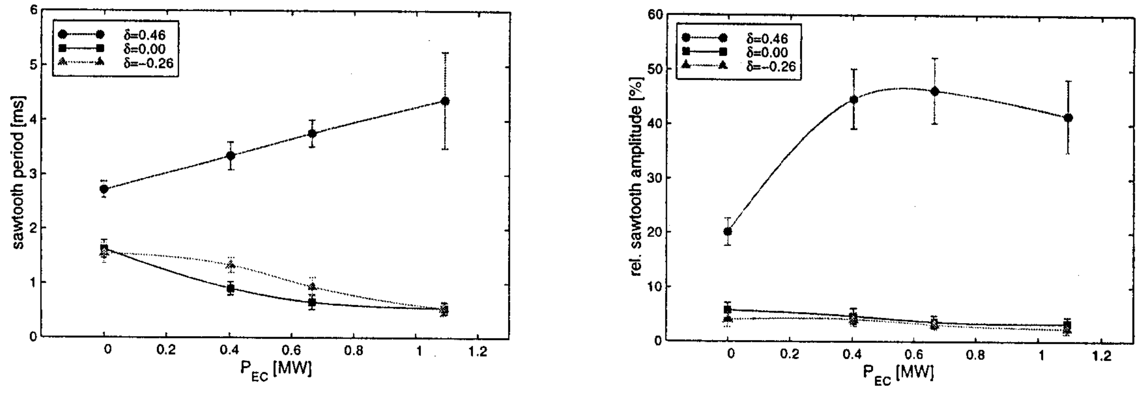

Fig. 4. Sawtooth period (4a) and relative crash amplitude (4b) stabilisation/destabilisation with increasing central power deposition for different triangular plasma shapes ($-0.26<\delta<0.46$, $\kappa=1.5\pm0.05$, q_{eng}~2).

For $\delta>0.2$, the sawtooth period and crash amplitude increase with increasing heating power, whereas for $\delta<0.2$ the sawtooth period decreases with increasing heating power, with a smaller relative crash amplitude, see **Fig. 4a, b**. Therefore, for positive triangularity $\delta>0.2$, heating power shows a sawtooth stabilisation effect, associated however with large crash amplitudes; on the contrary, increasing the power in negative triangularity discharges induces sawtooth destabilisation and relative smaller crash amplitudes. This has two advantages: first of all, negative triangularity discharges reduce the amplitude of the sawtooth heat pulse and can help to reduce the amplitude of a possible seed island.

The effect of increasing the plasma elongation appears very similar to the effect of increasing negative triangularities: when increasing the power for elongations above $\kappa=1.5$, sawteeth are also destabilised, sawtooth periods becoming shorter and of smaller amplitude.

The stabilisation effect of positive triangularity and high elongation seen in the experiment is in qualitative accord with the effect of triangularity and elongation on the Mercier stability of the ideal internal kink mode or on the resistive MHD stability of the $m=1$ mode, both stabilised by positive triangularity and ellipticity (and destabilised at negative triangularity and high elongation [9].

Conclusions The dependence of the electron energy confinement time is studied by varying the density, power, triangularity, elongation and current. The electron energy confinement time is found to increase with a combination of elongation and plasma current, two quantities which are still strongly correlated in the present study. The beneficial effect of triangularity, previously observed in Ohmic discharges, continues to be seen at the power levels used here. However, the benefit of low or slightly negative triangularity on confinement is most effective at low total power and decreases, without disappearing, at the highest powers used so far. The specific power scaling law obtained by regression on the TCV data for constant triangularity very closely fits the Rebut-Lallia-Watkins scaling and, over the parameter range studied, is similar to the ITER-98-L scaling when neglecting the ion contribution. Using these two scaling representations, the beneficial effects of negative triangularity appear clearly.

Sawtooth stability is improved at positive triangularity and at low elongation, producing large sawtooth crashes. High elongation or negative triangularity appear therefore attractive to reduce the amplitude of heat pulses and seed islands which can follow large sawtooth crashes in high power experiments. The strong effect of plasma shape on the sawteeth characteristics and (de-)stabilisation with power could also play a role in the present confinement experiments, since sawteeth are one of the major loss channels in the plasma core of these centrally heated discharges.

The addition of the second cluster of ECRH power sources will be important to determine more clearly the triangularity dependence at high power and will allow the study of confinement in higher elongation discharges at a higher P_{EC}/P_{OH} ratio.

Acknowledgements This work was partly supported by the Fonds national suisse pour la recherche scientifique.

References

[1] J-M Moret, et al., Phys. Rev. Lett. **79** (1997) 2057 and Weisen H. et al., Nucl. Fus. **37** (1997) 1741.

[2] A Pochelon et al., Proc. of Joint ICPP 1998 and 25th EPS Conf. on Contr. Fusion and Plasma Physics, Praha 1998, ECA Vol. **22C** (1998) 1324.

[3] A Pochelon et al., 17th IAEA Fusion Energy Conf. 1998, CN-69/ITER/EX8/3, to appear in Nuclear Fusion, Yokohama Special Issue (1999).

[4] A Pochelon et al., 2nd Eur. Top. Conf. on RF Heating and Current Drive, Brussels, **22A**, (1998) 253.

[5] ZA Pietrzyk. et al., Nuclear Fusion, **39** (1999) 587.

[6] H Weisen et al., Plasma Phys. Control. Fusion **40** (1998) 1803.

[7] K Thomsen et al., 17th IAEA Fusion Energy Conf. 1998, CN-69/ITER/3-ITERP1/07.

[8] KA Razumova et al., Peculiarity of Plasma Behav. in the Vicinity of rat. q Value, this Conf., Or 20.

[9] H Lütjens, A Bondeson and G Vlad, Nuclear Fusion **32** (1992) 1625.

Current and Pressure Profile Control using ECCD and ECH in TCV

O. Sauter, R. Behn, S. Coda, I. Furno, T.P. Goodman, M. Henderson,
F. Hofmann, J.-P. Hogge, C. Nieswand, A. Pietrzyk, A. Pochelon,
H. Reimerdes, J. Rommers

Centre de Recherches en Physique des Plasmas
Association EURATOM-Confédération Suisse
Ecole Polytechnique Fédérale de Lausanne, CH-1015 Lausanne, Switzerland

Abstract

Steerable mirrors allow the change of both the poloidal and toroidal launcher angles in TCV. Both ECH and ECCD experiments have been performed in order to demonstrate the modifications of the electron temperature and current profiles. We have achieved full replacement of 153kA with central co-ECCD using three 0.5MW gyrotrons for 100 ms. However this led to very peaked pressure and current profiles which are unstable and eventually led to a disruption. Using a scenario with simultaneous on and off-axis co-ECCD we have obtained a fully non-inductive steady-state scenario sustaining 123kA, with T_{e0}=3.5keV and n_{e0}=1.5 10^{19} m^{-3} for 1.9s, more than 400 confinement times and about 4 current diffusion times, limited only by the gyrotron pulse length. We also show that a careful choice of the plasma current is needed to exactly replace the ohmic plasma current. Finally we confirm a significant current drive efficiency for far off-axis ECCD.

Results

In the last decade important progress have been achieved towards increasing the plasma confinement time, the plasma density and the value of β in stationary scenarios. In the design work for ITER, it has been shown that it is crucial to be able to keep good confinement while having both the density and β close to their respective limits [1]. This can only be achieved successfully through precise control of both the current and pressure profiles. The TCV tokamak has a powerful and very flexible ECW system [2]. At present we have three launchers of up to 0.5 MW for 2s each, which are used in the X2 mode achieving 100% single pass absorption. Each launcher has a system of four mirrors allowing a large variation of both the poloidal and toroidal angles. The first results of varying these angles are given in Ref. [3], where the formation of high energy tail electrons is demonstrated in ECCD cases. In particular, it is shown that the optimal toroidal angle for co-ECCD is around 35°, which is the angle used in this paper.

The aim of the present study is to obtain a fully non-inductive stationary scenario using three 0.5 MW gyrotrons. In order to achieve this, we need not only to sustain the plasma current by adequate current drive, but also to control the profiles so as to have a stable and quiescent plasma. Therefore one has to distribute the power deposition over the minor radius ρ in order to replace the ohmic profiles by the ones driven by ECCD and ECH. On the other hand the current drive efficiency is much larger near the magnetic axis, because of increased temperature and fraction of passing particles. Moreover, the highest temperatures are obtained when heating inside the q=1 radius [4,5]. Therefore, to obtain the maximum driven current with 1.5 MW of ECCD, one needs to have central deposition, as shown by the rays labelled 'B' in Fig. 1.

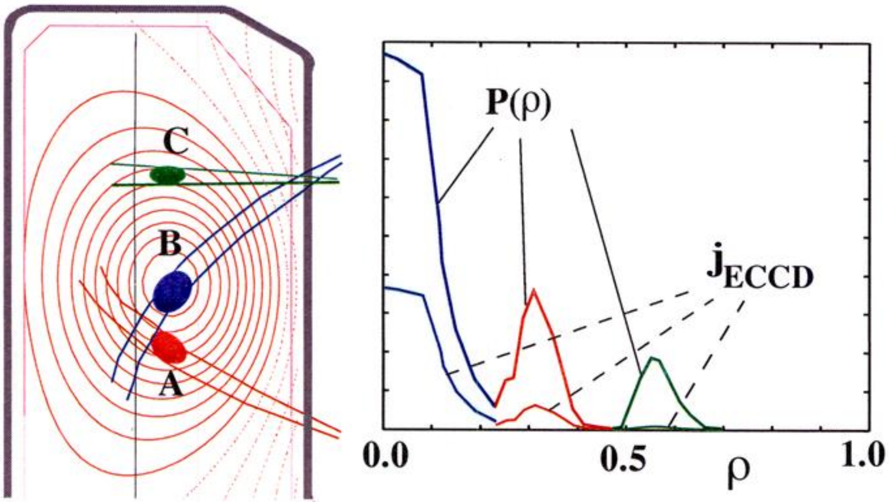

Fig. 1: a) Typical ray paths of the 3 launchers in the poloidal plane.
b) Power and current deposition profiles from Toray calculations when the three launchers are in co-CD mode with $\varphi=35^0$.

A typical result of such a scenario is shown in Fig. 2, where 153kA is fully non-inductively driven for about 100 ms, with $n_{e0}=2\cdot10^{19}$ m^{-3} and T_{e0}=4.5 keV, before it disrupted. In these scenarios the three gyrotrons were in on-axis co-ECCD position. As the width of the ECW power deposition is small, of the order of 10%-20% of the minor radius, it means that the resulting current and pressure profiles are very peaked. Due to these sharp local gradients, MHD modes became unstable which caused a fast disruption as in Fig. 2. Neoclassical tearing modes were also destabilized and degraded the performance of the discharge.

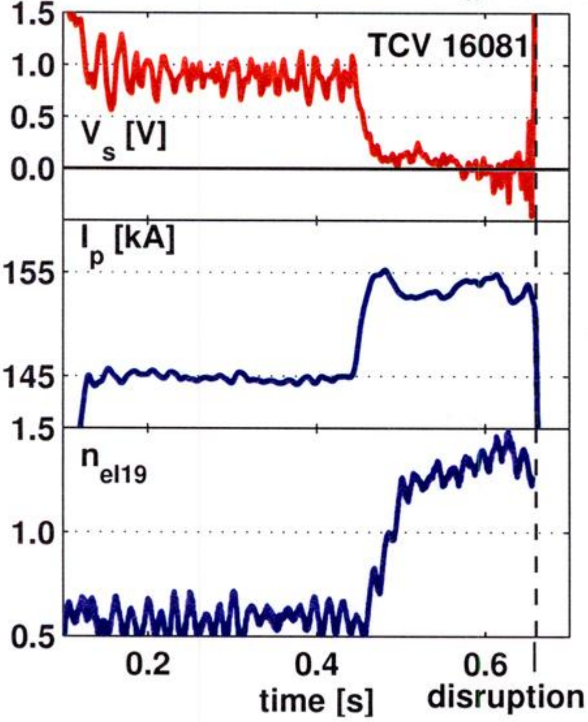

Fig. 2: Complete replacement of 153kA for more than 100 ms with 1.5MW on-axis co-CD. These scenarios disrupted due to very large gradients obtained with very peaked profiles.

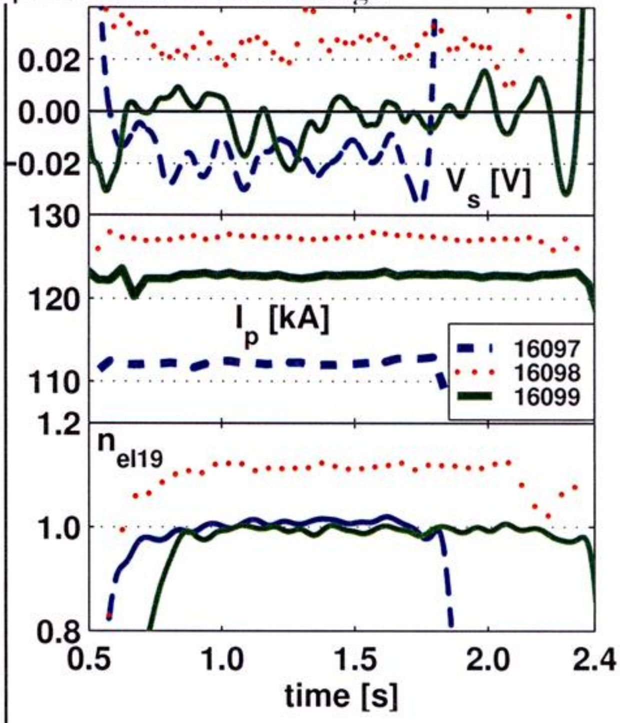

Fig. 3: Scenarios as shown in Fig. 1. The steady-state fully non-inductive scenario was obtained with I_p=123kA (solid line). With I_p set to 112kA (dashed) and 127 kA (dotted), V_s was slightly changed.

In order to avoid these modes, we distributed the power deposition of the three gyrotrons over the minor radius, as shown in Fig. 1, at ρ=0., 0.3 and 0.55. In this case the central temperature and the total driven current are smaller than with central deposition. However both the current and pressure profiles are broader and no MHD modes were generated. In this way we obtained a fully non-inductive discharge of 123kA for 1.9s with $n_{e0}{\approx}1.5{\cdot}10^{19}$ m^{-3} and $T_{e0}{\approx}3.5$ keV, as shown in Fig. 3 (solid line) and detailed in Fig. 4. In particular we show in Fig. 4b that the current in the ohmic transformer was held constant. This is the most sensitive measurement to full current replacement. As seen in Fig. 4b, V_s reached zero very soon after the ECCD was turned on, while the equilibrium profile still evolved for 0.5s (see κ, l_i in Fig. 4). We repeated this discharge with I_p=112kA and 127kA to demonstrate the exact control of the amount of current driven non-inductively (Fig. 3). In the first case (dashed line), the surface loop voltage V_s is slightly negative, indicating an excess of driven current, and in the second case (dotted line) it is positive. Taking into account the ~10% decrease in current drive efficiency in the latter case due to the density increase, these results are consistent with exact replacement at I_p=123kA and I_p-I_{CD}=11kA for $|V_s|$=0.02 V. This is also in agreement with Toray [7] calculations which give I_{CD}=120kA. However the bootstrap current generated by the peaked pressure profile obtained with ECW is non-negligible and is about 25kA, using the formulae in Ref. [8]. Therefore the ECCD is overestimated by about 20% by Toray, which is well within the uncertainties of the density and temperature profiles.

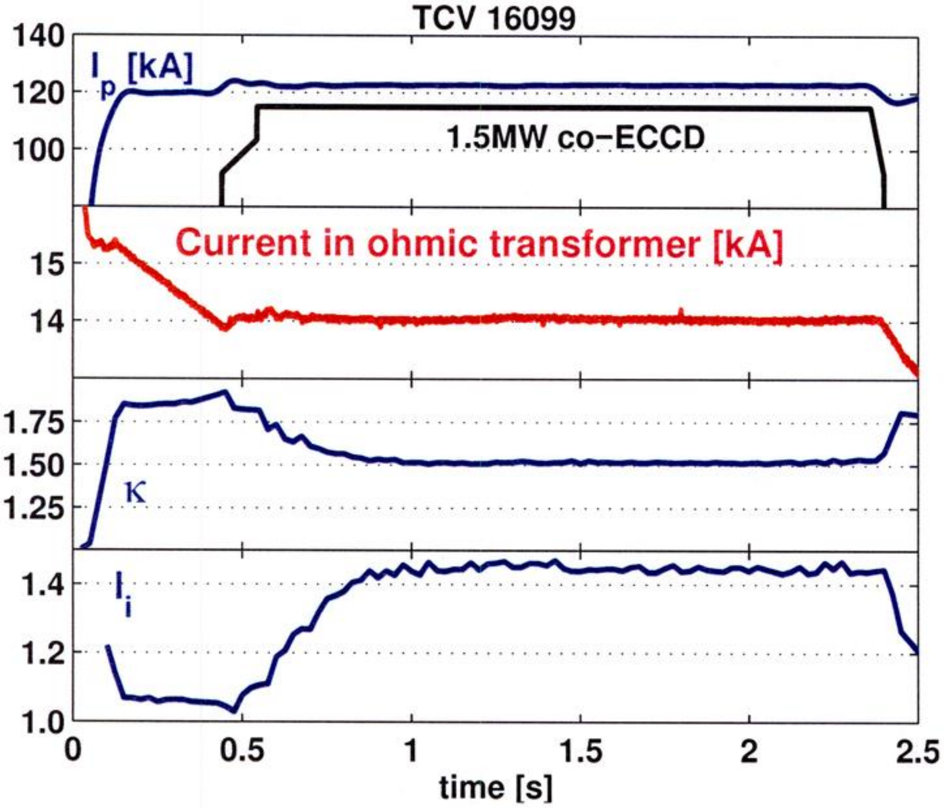

Fig. 4: Steady-state fully non-inductive discharge for 1.9s using 1.5MW of co-CD distributed over the minor radius as shown in Fig. 1. Note that the current in the ohmic transformer is exactly constant, indicating zero inductive current in the plasma. This happens as soon as the ECCD is turned on, while the equilibrium profiles need 0.5s to settle, as indicated by the evolution of κ_{edge} and l_i.

From Toray calculations, Fig. 1b, the current driven by the most off-axis gyrotron, C, is very small, ≈2.5kA, near ρ=0.55. Therefore, this gyrotron seems mainly to be used to broaden the temperature profile, as the power deposited is non-negligible as shown by $P(\rho)$. To test this we have repeated the shot 16099, but with only the two gyrotrons A and B in co-ECCD position and the third in ECH (φ=0°). This scenario is shown in Fig. 5, shot 16150. As the density was 5% higher, we repeated it with all three gyrotrons in co-ECCD, shot 16151 for a better comparison. In the first case, 16150, V_s is non-zero, about 0.02V, whereas the shot 16151 has V_s near zero (≈0.005V). Therefore the current driven by the gyrotron C is important and 7-9kA are driven at $\rho{\approx}0.55$. This confirms the results obtained on DIII-D [9] that more current can be driven off-axis than predicted. In our case, the experimental value is only a factor of 2-3 above the predicted value, even for $\rho\approx0.55$, as Toray predicts a non-zero value. Note that the experimental local efficiency normalized by the local temperature, as in Ref. [9], is about 0.07 corresponding to the lower bound of the DIII-D results. However our results are obtained in a fully non-inductive scenario and in a stationary phase.

Conclusion

The ECH system on TCV has been used to obtain full current replacement in standard (positive magnetic shear) discharges. With on-axis co-CD, up to 153 kA have been fully non-inductively driven with $n_{e0}=2\cdot10^{19}$ m^{-3} and $T_{e0}=4.5$ keV ($\gamma_{20CD}=0.018$ A/W/m^2), 30% of the current is due to the Bootstrap current. However these scenarios lead to very peaked current and pressure profiles and eventually to disruption. With careful profile control by spreading the power deposition across the minor radius, we have obtained a steady-state fully non-inductive scenario for 1.9s, with $I_{NI}=123$kA, $n_{e0}\approx1.5\cdot10^{19}$ m^{-3} and $T_{e0}=3.5$keV ($\gamma_{20CD}=0.01$ A/W/m^2, 20% bootstrap current), limited only by the pulse length of our gyrotrons. Note that this is more than 400 confinement times and about 4 times the current diffusion time.

Finally we have shown in the steady-state scenario that about 7-9kA were driven at $\rho\approx=0.55$, corresponding to $\zeta=0.07$ and 2-3 times the predicted value. This confirms the discrepancy observed by DIII-D, albeit to a lesser degree.

This work was partly supported by the Swiss National Science Foundation.

References

1. ITER Physics Basis, accepted for publication in Nucl. Fus.
2. T.P. Goodman et al, Proc. 19th SOFT, Lisbon (1996), 565.
3. S. Coda et al, this conference.
4. R. Behn et al, this conference.
5. N. J. Lopes-Cardozo et al, Plasma Phys. Contr. Fus. 39 (1997) B303.
6. R. Pitts et al, this conference.
7. G. R. Smith et al, in Proc. of the 9th Joint Workshop on ECE and ECRH at Borrego Springs, California (January, 1995), Editor World Scientific (1995) 651.
8. O. Sauter et al, to appear in Phys. Plasmas, July (1999).
9. T. C. Luce et al, General Atomics Report (1999) GA-A23018.

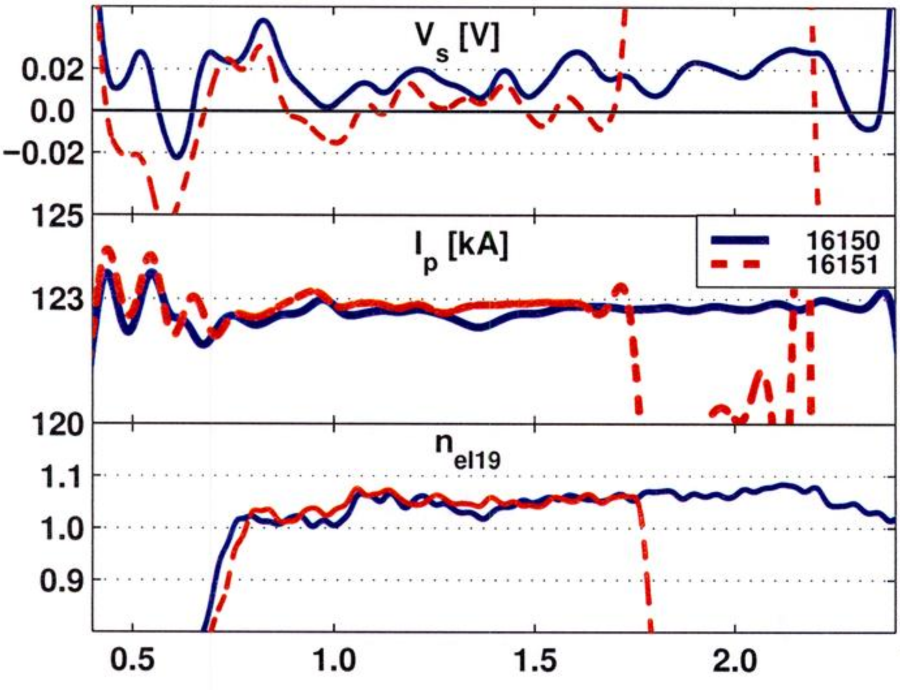

Fig.5: Two discharges with launchers in the same position as in Fig. 1, except for shot 16150 which has launchers A and B in co-CD and the third, C, in heating mode ($\varphi=0$). The shot 16151 has the three launchers in co-CD and is therefore identical to shot 16099 apart for the 5% change in density, to match shot 16150. This clearly shows that the very off-axis gyrotron in position C does drive current (7-9kA) as V_s is more positive for 16150 than 16151.

Analytical and Computational Investigations of Improved-Confinement Stellarators

A.A. Subbotin, W.A. Cooper*, M.Yu. Isaev, M.I. Mikhailov,
J. Nührenberg** V.D. Shafranov

Nuclear Fusion Institute, RRC "Kurchatov Institute", Moscow, Russia
* *Centre de Recherches en Physique de Plasmas, Association Euratom - Confédération Suisse, Ecole Polytechnique Fédérale de Lausanne, Lausanne, Switzerland*
** *Max-Planck-Institut für Plasmaphysik, Teilinstitut Greifswald IPP-EURATOM Association, D-17489, Greifswald, Germany*

1. Introduction

The stellarator configurations with poloidal direction of lines B=constant on magnetic surfaces have been previously shown to possess some attractive features. First of all, zero magnetic-axis curvature at the locations of the longitudinal magnetic field minima provides the possibility to improve the confinement of charged particles: by a corresponding choice of the near-axis magnetic surface cross-sections, it is possible to eliminate locally lost orbits and even to satisfy the condition of quasi-isodynamicity (QI) for reflected particles of deep to moderately-deep trapping condition [1]. Secondly, the choice of the system with poloidal direction of constant B contours on magnetic surfaces was shown to increase the plasma pressure limit with respect to local stability [2] by improving the local stability condition for ballooning modes which are very localised along the magnetic field lines. Despite the possible decrease of the average magnetic well, the Mercier modes could still remain stable under these circumstances.

In the present paper, such configurations are studied both analytically, up to second-order terms in the expression for B in an expansion with respect to the distance from the magnetic axis, and numerically.

2. The strength of the magnetic field in near-axis approximation

Using the method of expansion with respect to the distance from the magnetic axis with curvature k and torsion κ, and the corresponding magnetic surface parameterisation (for detail, see, e.g. [3]), one can obtain the expression for B up to second-order in a. For vacuum systems, when the diamagnetic effect is negligible, this expression has the form:

$$\begin{aligned} B^2 = B_0^2 b^2 \{ 1 + 2a(A_c \cos\theta + A_s \sin\theta) + a^2 [3(A_c \cos\theta + A_s \sin\theta)^2 \\ + A_{20} + A_{2c} \cos 2\theta + f_0 + f_c \cos 2\theta + f_s \sin 2\theta] \} \ . \end{aligned} \tag{1}$$

Here

$$\begin{aligned} f_0 &= \frac{1}{bR^2} \left[-(\kappa_n^2 R^2) \frac{sh^2\eta}{ch^2\eta} + \frac{1}{4} \left(\eta'^2 + \frac{b'^2}{b^2} \right) ch\eta + \frac{\eta''}{2} sh\eta - \frac{b''}{2b} ch\eta \right] \ , \\ f_c &= \frac{1}{bR^2} \left[(\kappa_n^2 R^2) \left(1 + \frac{1}{ch^2\eta} \right) sh\eta - \frac{1}{4} \left(\eta'^2 + \frac{b'^2}{b^2} \right) sh\eta - \frac{\eta''}{2} ch\eta + \frac{b''}{2b} sh\eta \right] \ , \\ f_s &= -\frac{1}{bR^2} \left[(\kappa_n R)' th\eta + (\kappa_n R)\eta' \left(1 + \frac{1}{ch^2\eta} \right) \right] \ , \end{aligned} \tag{2}$$

$$\begin{aligned} \kappa_n &= \kappa - \delta'/R \ , \quad A_c = k \frac{\exp(-\eta/2)}{\sqrt{b}} \cos\delta \ , \quad A_s = k \frac{\exp(\eta/2)}{\sqrt{b}} \sin\delta \ , \\ A_{2c} &= -2(\alpha_1 A_c + \alpha_2 A_s) \ , \quad A_{20} = A_c(\xi_1 + \alpha_1) + A_s(\xi_2 - \alpha_2) \ . \end{aligned} \tag{3}$$

The parameters η and δ describe the elliptical magnetic surface shape, the function b describes the magnetic field inhomogeneity on the magnetic axis, prime denotes the derivative with respect to the longitudinal coordinate ζ, and ξ_i and α_i are the plasma column shifts and triangularities, $2\pi R$ is the magnetic axis length.

For systems with poloidal direction of lines B=constant, the following conditions of particle confinement improvement can be formulated for the region near $\zeta = 0$.

1) The condition of local pseudosymmetry (PS) (there are no islands formed by the constant B lines near the region $\zeta = 0$). To first order in a, this condition requires $k(0) = 0$. If it is fulfilled, the expression for B can be written as

$$\begin{aligned} B^2 &= B_0^2 b^2 \left\{ 1 + a^2 \left[\left(A_{20} - b \left(\frac{A_c^2 + A_s^2}{2b'} \right)' + f_0 \right) \right. \right. \\ &+ \left. \left. \left(A_{2c} - b \left(\frac{A_c^2 - A_s^2}{2b'} \right)' + f_c \right) \cos 2\theta + \left(-b \left(\frac{A_c A_s}{2b'} \right)' + f_s \right) \sin 2\theta \right] \right\} , \end{aligned} \tag{4}$$

and to fulfill this condition in the second approximation, the coefficients of the $\cos 2\theta$ and the $\sin 2\theta$ terms in Eq. (4) should be zero for $\zeta = 0$.

2) To diminish the particle radial excursion, one can try in addition to fulfill the QI condition [1] which requires $J_{||} = \oint V_{||} dl = J_{||}(a)$. In the flux coordinate system with straight magnetic field lines a, θ^*, ζ^* with $B = B(a, \zeta^*)$, it can be formulated as the independence of the combination

$$\Delta\varphi = \varphi(a, \theta_0^* + \iota\zeta_0^*, \zeta_0^*) - \varphi(a, \theta_0^* - \iota\zeta_0^*, -\zeta_0^*) \tag{5}$$

on θ_0^*. Here $\varphi(a, \theta_0^*, \zeta_0^*)$ is the potential part of $\mathbf{B}$ in the covariant representation in a, θ_0^*, ζ_0^* flux coordinates. In a linear approximation with respect to a, the expression for φ acquires the form (for simplicity superscripts (*) are omitted for θ, ζ):

$$\begin{aligned} \varphi &= \varphi_0(\zeta) + \frac{akb^{3/2}}{b'} \{ [\exp(-\eta/2) \cos\delta \cos(\iota\zeta - \eta_0^*) + \exp(\eta/2) \sin\delta \sin(\iota\zeta - \eta_0^*)] \cos\theta_0 \\ &+ [-\exp(\eta/2) \cos\delta \sin(\iota\zeta - \eta_0^*) + \exp(\eta/2) \sin\delta \cos(\iota\zeta - \eta_0^*)] \sin\theta_0 \} . \end{aligned} \tag{6}$$

Here the parameter η_0^* describes the slope of the magnetic field lines. It can be extracted from the equation: $-\iota + \partial\eta_0^*/\partial\zeta = \kappa_n R / ch\eta$.

Different possibilities to fulfill the QI condition can be considered. For example, for $b' \sim \zeta$, $k \sim \zeta$, $\delta \sim \zeta$, $\eta = \eta(0) + \eta''(0)\zeta^2/2$, $\kappa = \kappa(0) + \kappa''(0)\zeta^2/2$, the term with $\cos\theta_0$ is even and drops out from the expression for $\Delta\varphi$. The term with $\sin\theta_0$ is odd. If its component that is linear with respect to ζ vanishes, that is if

$$\kappa_n R / ch\eta = -\delta' \exp(\eta) , \tag{7}$$

the longitudinal invariant acquires the form $J_{||} \sim \zeta_0^2 (1 + \gamma a \zeta_0^2 \sin\theta_0)$. It is worth to emphasize that condition (7) is local, i.e. it depends on the magnetic surface structure near the region $\zeta = 0$ only. The region in which $J_{||}$ does not depend on θ_0 can be expanded if the terms of higher order in ζ can be eliminated too. In principle, it can be done up to any given order. Nevertheless, the requirement to fulfill this condition on the whole magnetic surface in general is incompatible with the periodicity conditions. If the curvature of the magnetic axis is proportional to ζ^2, then for the ordering used above, it is impossible to fulfill the QI condition even at lowest order. In this case we can consider another condition.

3) The condition of the existence of closed B=constant surfaces near the region $\zeta = 0$. This condition requires the coefficient of a^2 in the expression (4) for B to be positive for all θ near the region $\zeta = 0$. It can be considered in combination with the condition of

local PS also. If it is fulfilled, the deeply-trapped particles are confined inside the closed surface B=constant and cannot drift out of the plasma column.

3. Some examples of numerical investigations

The possibilities to fulfill some of the conditions of particle confinement improvement discussed above have been verified numerically. The results are presented in the Table and in Figs. 1-4. Two different cases were considered in the near-axis approximation for 8-periods systems.

Case (1) corresponds to a system with $k \sim \zeta^2$. Here the parameters were found for a system which possesses a vacuum magnetic well, an absolute minimum of B near the region $\zeta = 0$ and in which the constant B contours on a flux surface do not form islands in this region to first and second order in a (Fig.1). The QI condition is not satisfied here. Case (2) correspond to a system with $k \sim \zeta$ (Fig. 2). For the parameters shown in the Table, this system displays a vacuum magnetic well, the B=constant lines do not show islands and is QI to leading order (condition (7) is fulfilled). The surfaces B=constant in this system are open.

3D equilibrium numerical calculations for a 5-periods Helias system were produced using the VMEC and TERPSICHORE codes. It was shown that there exist equilibria without islands of lines B=constant in the middle of the system period. Magnetic flux surface cross-sections and contours of B=constant on a boundary magnetic surface are presented in Figs. 3 and 4.

Parameters of magnetic configurations with a vacuum magnetic well and no islands of lines B=constant near the region $\zeta = 0$. The functions $k, \kappa, \eta, ...$ have the form: $k(\zeta) = \sum_n (k_{cn} \cos nN\zeta + k_{sn} \sin nN\zeta)$.

	k_{c0}	k_{c1}	k_{c2}	k_{s1}	κ_{c0}	κ_{c1}	η_{c0}	η_{c1}	b_{c0}	b_{c1}	δ_{s1}	α_{1c0}	α_{1c1}
1	1.20	-1.2	0	0	0.07	6.57	0.33	-0.28	1.014	-0.014	0	0.02	0.07
2	0.95	0	-0.95	2.4	0	3.0	0.75	-0.25	1.05	-0.05	-0.45	0.05	0.08

4. Conclusions

The results of both analytical and numerical investigations of different possibilities to control the behaviour of the B=constant lines (on flux contours) and the B=constant surfaces are presented. The conditions of local PS and QI are obtained and investigated in a near-axis approximation as well as the condition for the existence of an absolute minimum of B. It is shown that the conditions of local PS, QI and magnetic well existence can be satisfied simultaneously in the near-axis approximation. Configurations were found also that possess an absolute minimum of B, a vacuum magnetic well and no island formation in the B=constant contours. The condition of QI is not fulfilled, however, in such type of configurations.

Acknowledgements

We thank Prof. M.Q. Tran for supporting this work. This work is partially sponsored by the Fonds National Suisse de la Recherche Scientifique and by EURATOM, and by Russian Foundation for Fundamental Research, project No 97-02-17695. One of the authors (M.I.M) made a part of this work during his visit to the Institute of Advanced Energy (Kyoto University). He would like to thank the Administrations of the Institute and Prof. T. Obiki for invitation and supporting of these investigations.

References

[1] S. Gori, W. Lotz, J. Nührenberg, Theory of Fusion Plasmas (Varenna 1996), Editrice Compositori, Bologna (1996), p.335.

[2] M.Yu. Isaev, W.A. Cooper, V.D. Shafranov, Proc. 25th EPS Conf. on Controlled Fusion and Plasma Phys., Prague, 1998, p.1738.

[3] M. Yu. Isaev, V.D. Shafranov, Sov. J. Plasma Phys. **16** (1990) 419.

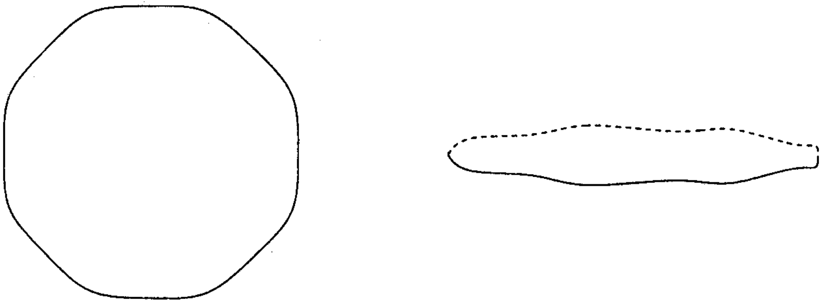

Fig. 1. Two projections of magnetic axis for the case that corresponds to a system with $k \sim \zeta^2$. For the parameters shown in the Table, this system possesses a vacuum magnetic well, an absolute minimum of B near the region $\zeta = 0$ and the lines B=constant display no islands in this region to first and second order in a. The condition of quasi-isodynamicity is not satisfied here.

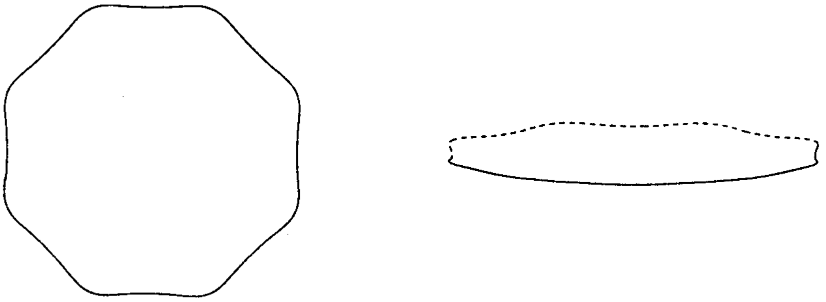

Fig. 2. Two projections of magnetic axis for the case that corresponds to a system with $k \sim \zeta$ near the region $\zeta = 0$. For the parameters shown in the Table, this system has a vacuum magnetic well, no islands formed by the lines B=constant to first and second order in a and is quasi-isodynamical to leading order.

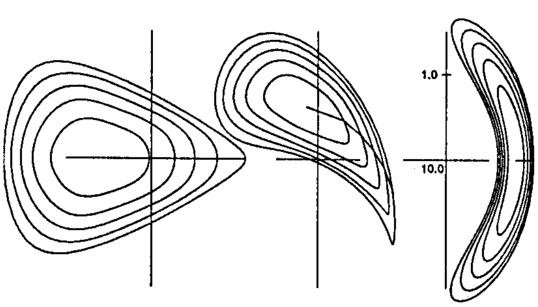

Fig. 3. Magnetic flux surface cross-sections at the beginning, at one quarter and at the middle of the period for a 5-period Helias with B=constant islands absent near midperiod of the system.

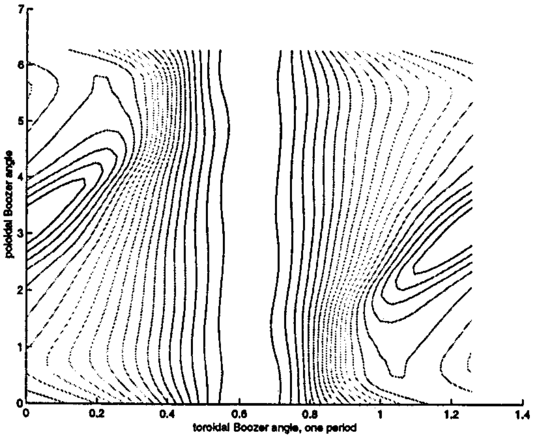

Fig. 4. Contours of B=constant on a boundary magnetic surface for a 5-period Helias without islands of lines B=constant at the middle of the system period.

β_p-Collapse-Induced VDE and its Underlying Mechanism in the TCV Tokamak

Y. Nakamura[1], J.B. Lister[2], F. Hofmann[2], Y.R. Martin[2], J.-M. Moret[2], P. Vyas[2]
[1]*Japan Atomic Energy Research Institute, Naka-machi, Naka-gun, Ibaraki 311-0193, Japan*
[2]*Centre de Recherches en Physique des Plasmas*
Association EURATOM-Confederation Suisse
Ecole Polytechnique Federale de Lausanne, CH-1015 Lausanne, Switzerland

1. Introduction

It is well known that the interaction between a disruptive tokamak plasma and a surrounding resistive shell plays an important role in the dynamics of a Vertical Displacement Event (VDE) [1]. This paper describes onset mechanisms of VDEs induced by a strong plasma pressure drop (β_p-collapse) in disruptive discharges of the Tokamak Configuration Variable (TCV). Many aspects of the TCV vertical instability have been investigated [2-7]. In this paper, we first compute open-loop growth rates of VDEs in TCV using the Tokamak Simulation Code (TSC) [8], and compare the results with JT-60U. We then investigated the eddy current effects due to a β_p-collapse for disruptive and non-disruptive TCV discharges in nonlinear TSC simulations.

2. TCV Vertical Stability

Since TCV is specifically designed to explore the operational benefits of plasma shaping over a wide variety of plasma shapes [4], it can generate a great variety of vertical instabilities. Vertical growth rates as a function of the magnetic field decay n-index $(n = R/B_Z\,(\partial B_R/\partial Z) = -R/B_Z\,(\partial B_Z/\partial R))$, defined at a magnetic axis, were evaluated by the TSC, as shown in Fig. 1. Major plasma parameters are the following : plasma current I_p = 352 kA, toroidal magnetic field B_t = 1.38 T, internal inductance ℓ_i = 1.1. Poloidal beta was taken as a range of β_p = 1.0, 0.5 and 0.0 to clarify the plasma pressure effect on the vertical instability. Figure 1 indicates that the growth rate increases as the magnitude of the n-index increases. The low β_p plasmas are more stable than the high β_p plasmas for a given n-index. Cases with similar shape, indicated by the groups of symbols in Fig. 1, show a decrease in the growth rate for increasing β_p, due to the reduction of the n-index required to produce the given shape.

A simple model of rigid shifts of circular-shaped plasmas states that the linear growth rate is a function of the n-index and the stability index n_s, defined by

$$n + n_s \frac{\gamma \tau_s}{1 + \gamma \tau_s} = 0 \quad . \qquad (1)$$

Here, τ_s is the effective skin time of the resistive shell. The stability index n_s depends on the shell-geometry and the plasma equilibrium.

By means of a least squares fit of Fig. 1 using Eq. (1), the TCV stability indices n_s were evaluated to be 2.41 for low β_p (= 0.0), 2.16 for β_p = 0.5 and 1.91 for β_p = 1.0, respectively. Although the decay time of the antisymmetric eddy current mode is 8.1 msec [4], τ_s was about 2.5 msec, reflecting a reduced coupling between the plasma and the vacuum vessel. The stability index of the JT-60U, where no β_p-collapse-induced VDE has been observed, was as high as $n_s = 3.4$ for $\beta_p = 0.0$ [9], because that the oval JT-60U vacuum vessel with a height-to-wide ratio of 1.3 is close to the plasma. In the TCV, the vacuum vessel has a large height-to-wide ratio, 3.0, and is consequently further from the plasma. As a result, the stability margin given by the definition of $|n_s/n|$ is as low as 1.5 for these equilibria, below 1.1 for extreme equilibria [10], while 2.1 in the JT-60U, providing $n = -1.6$. This implies that the TCV is more close to the absolute stability limit than the JT-60U, and hence, VDEs might more easily occur under a change of equilibrium state such as β_p-collapse.

3. β_p-Collapse-Induced VDE

3.1 TCV Experiments

Figure 2 shows the TCV disruptive discharge #10890 during the period 310.0 msec - 335.0 msec. The poloidal beta and the internal inductance before the β_p-collapse were $\beta_p = 0.46$ and $\ell_i = 1.0$, respectively. The plasma elongation κ at the boundary was as high as 1.8. A β_p-collapse of $\Delta\beta_p = -0.46$ had set in at 327.0 msec and was assumed to last for about 4.0 msec. Some oscillatory behavior of the vertical position can be seen before the β_p-collapse, indicating that the feedback system was already marginally stabilizing the vertical position. A plasma current quench following the β_p-collapse had occurred at 331 msec. While the radial shift of the plasma magnetic axis was observed to be $\Delta R = -2.0$ cm during the period of the β_p-collapse, the vertical position moved upward to around $Z = 40$ cm at 4 msec after the onset of the β_p-collapse. The experiment of Fig. 2 consequently shows that the strong β_p-collapse has provoked a significant change in the vertical stabilization which could trigger a VDE.

On the contrary, a less elongated discharge #10606 ($\kappa = 1.35$) with lower β_p (= 0.38) survived after a small β_p-collapse ($\Delta\beta_p \sim -0.2$), as shown in Fig. 3. Although the radial shift of the plasma magnetic axis was observed to be $\Delta R = -1.0$ cm, the small β_p-collapse of $\Delta\beta_p = -0.2$ at 711.0 msec did not result in a VDE.

3.2 TSC Simulation

The TSC simulation was carried out to reproduce the β_p-collapse behavior of the TCV discharge #10890 by introducing a rapid plasma pressure drop of $\Delta\beta_p = -0.46$ at 327 msec. In the simulation, the vertical feedback control was turned off at 327 msec on the assumption that due to the β_p-collapse the active feedback failed to keep the plasma at a desired vertical position. Figure 4 shows the comparison between the plasma configurations of the experiment and the simulation. The TSC nicely reproduces every equilibrium of the TCV discharge #10890.

Figure 5 shows TSC time-evolutions of the plasma current and the position of the magnetic axis. The β_p-collapse led to the coincident radial shift of the magnetic axis by $\Delta R = -2.0$ cm, as in the experiment. Simultaneously, the n-index, evaluated at the magnetic axis, degraded from $n = -1.6$ to -1.9 ($\Delta n = -0.3$) due to eddy current effects. As in the experiment, a fast VDE occurred, and a large vertical displacement of $Z = 40$ cm was observed at 4.0 msec after the β_p-collapse. The vertical growth rate at the beginning phase of 327 msec - 329 msec was estimated to be 1300 sec^{-1}. After 329 msec, the magnetic axis moves vertically into a region of a better n-index, and hence, the VDE should be slowed down due to lower absolute value of the n-index, as in Fig. 2.

Figure 1 implies that the pure vertical growth rate before the β_p-collapse was 1000 $\sec^{-1}$, indicating that (a) the loss of plasma β_p improved the vertical instability, and that (b) the degradation of n-index leads to a destabilization [9]. The degradation arises from an additional quadrupole moment of magnetic field produced by eddy currents flowing to suppress the inward radial shift of the magnetic axis. The mechanism (b) competes with the improvement (a) during disruptions. When the destabilizing mechanism (b) overcomes the improvement (a), the vertical instability should be enhanced compared with its value before the β_p-collapse. In the case of the discharge #10890, the initial growth rate of 1000 $\sec^{-1}$ is reduced to 750 $\sec^{-1}$ by the mechanism (a), and then, by the destabilization (b) due to the degradation of Δn = -0.3 the vertical instability is increased up to 1500 $\sec^{-1}$, which is nearly same as the TSC growth rate of 1300 $\sec^{-1}$ just after the β_p-collapse. On the contrary, the vertical growth rate of the less elongated discharge #10606 remained much smaller even after the β_p-collapse of $\Delta\beta_p$ = -0.2.

4. Conclusion

The effect on vertical stability of a strong β_p-collapse in the highly elongated TCV tokamak was investigated computationally and experimentally. Disruptive and non-disruptive discharges were classified into those which appeared to have a β_p-collapse-induced VDE and those which survived without a VDE, according to the magnitude of the β_p-collapse and the plasma elongation (the n-index) just before the β_p-collapse occurs. One particular disruptive discharge of a highly elongated, rather high β_p plasma presents the typical behavior of the β_p-collapse-induced VDE after a full β_p-collapse. The essential mechanism of the β_p-collapse-induced VDE was confirmed to be an intense enhancement of the vertical instability due to a large and sudden degradation of the n-index produced by eddy currents.

Since the destabilizing mechanism due to a β_p-collapse depends on the operational regime of the plasma configuration in addition to the specifics of the shell-geometry, further experiments of higher β_p and elongation are required. These are now under way in the TCV with high power ECH. The authors would like to express their gratitudes to Drs. O. Sauter, B. Duval and I. Bandyopadhyay for the support of our computational studies and the useful discussions. They also wish to thank Professors F. Troyon and M.Q. Tran and Drs. T. Ozeki and R. Yoshino for their continuous encouragement.

References

[1] Nakamura Y *et al* 1996 *Nucl. Fusion* **36** 643

[2] Hofmann F, Moret J-M and Ward D J 1998 *Nucl. Fusion* **38** 1767

[3] Hofmann F, Dutch M J, Favre A *et al* 1998 *Nucl. Fusion* **38** 399

[4] Hofmann F, Dutch M J, Ward D J *et al* 1997 *Nucl. Fusion* **37** 681

[5] Ward D J and Hofmann F 1994 *Nucl. Fusion* **34** 401

[6] Ward D J, Bondeson A and Hofmann F 1993 *Nucl. Fusion* **33** 821

[7] Hofmann F and Jardin S C 1990 *Nucl. Fusion* **30** 2013

[8] Jardin S C, Pomphrey N and Delucia J 1986 *J. Comput. Phys.* **66** 481

[9] Nakamura Y, Yoshino R *et al* 1996 *Plasma Phys. Contr. Fusion* **38** 1791

[10] Lister J B : This conference

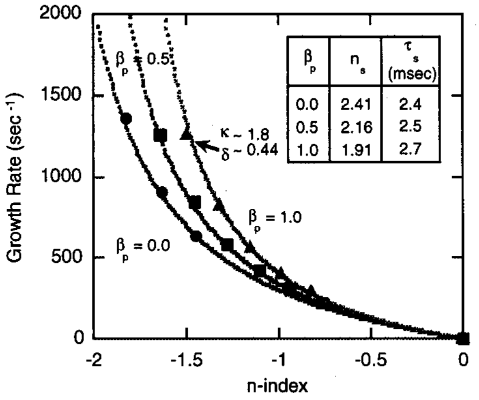

Fig. 1 Vertical growth rates of TCV as a function of decay n-index.

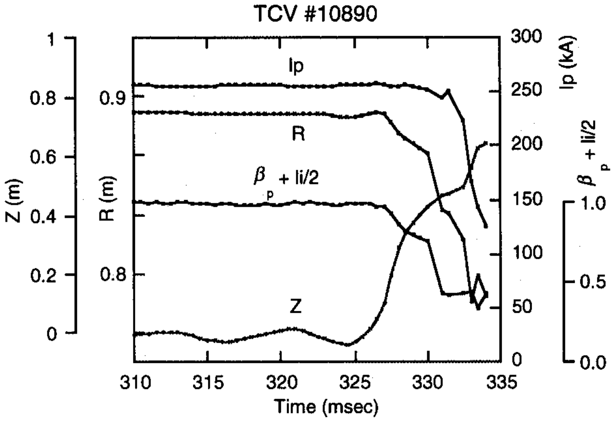

Fig. 2 TCV disruptive discharge #10890 (κ = 1.8) due to full βp-collapse of Δβp = -0.46, which had set in at 327.0 msec. βp-collapse could trigger a VDE.

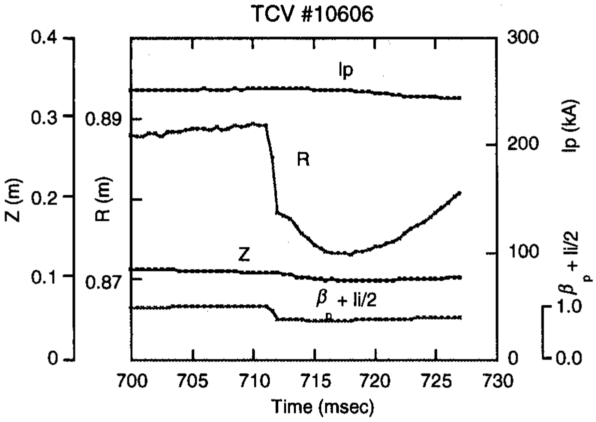

Fig. 3 TCV discharge #10606 (κ = 1.35) with small βp-collapse (Δβp ~ -0.2), which had set in at 711.0 msec.

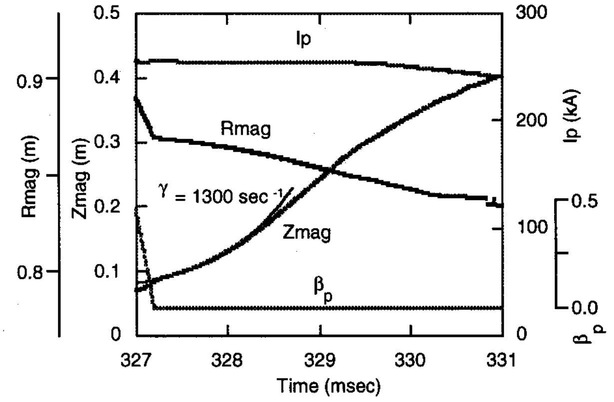

Fig. 5 TSC simulation of TCV disruptive discharge #10890. Vertical growth rate was estimated to be 1300 sec^{-1}.

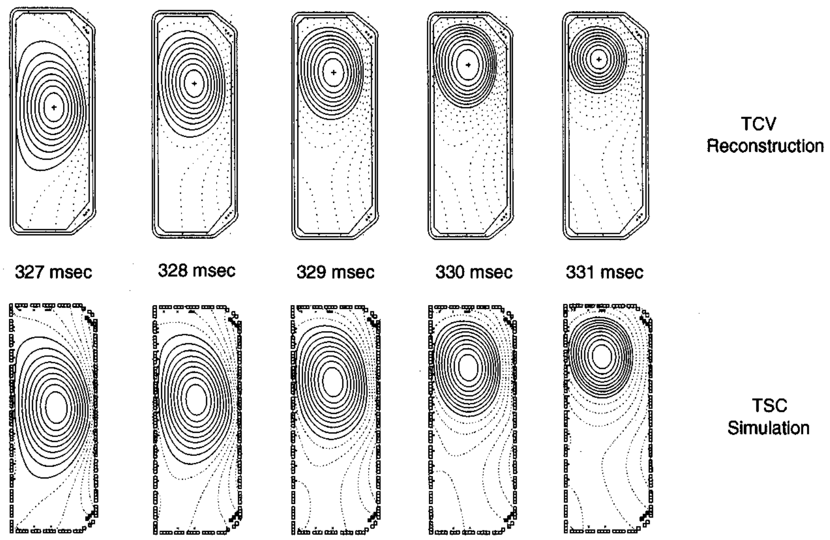

Fig. 4 Comparison of experimental (upper row) and numerical (lower row) configurations of TCV discharge #10890.

Vertical and Kink Mode Stability Calculations for Current Carrying Quasiaxial Stellarators

M. H. Redi[1], C. Nuehrenberg[2], W. A. Cooper[3], G-Y. Fu[1], C. Kessel[1], L.P.Ku[1], D. A. Monticello[1], A. Reiman[1], M. C. Zarnstorff[1]

[1]Princeton Plasma Physics Laboratory, Princeton University, Princeton, NJ 08543
[2]IPP, Greifswald, Germany
[3]CRPP-PPB, Lausanne, Switzerland

1. Introduction

Vertical and kink mode stability are essential for strongly shaped tokamaks, to preclude disruptive plasma termination. Similarly, the design of stellarators with significant current, such as quasiaxial stellarators (QAS) must be carefully examined to ensure adequate vertical and kink stability. The CAS3D [1] and TERPSICHORE [2] MHD stability code packages are being used to evaluate the stability of QAS configurations. CAS3D has previously been applied to predict stability of the W7-X stellarator, under construction at IPP, Greifswald, Germany. As part of a multifaceted effort to develop an interesting compact quasiaxial stellarator configuration for a modest sized experiment at PPPL, these two code packages are being used for three dimensional calculations of internal and external MHD stability, including extensive benchmarking of MHD stability for axisymmetric and nonaxisymmetric cases.

2. Global MHD Stability Code Packages: CAS3D and TERPSICHORE

CAS3D is a code package for the analysis of the stability of three dimensional magnetohydrodynamic equilibria which makes use of finite element Fourier decomposition in Boozer coordinates. From the several versions of this code package, CAS3D2vac is used here for calculations of the kink mode and the periodicity-preserving mode (known as the axisymmetric or vertical mode in tokamaks). Version CAS3D2MN, with a phase factor transform, was used for the fixed boundary two field period QAS benchmarking calculations. TERPSICHORE has many similar features and has recently been extended to calculations of the periodicity-preserving mode. It has been written for efficient computation and is being used in configuration optimization of the compact stellarator design.

3. Calculations for Internal Mode Stability of a Quasiaxially Symmetric Stellarator

During 1997-1998 we carried out benchmarking studies with CAS3D and TERPSICHORE which examined Mercier unstable modes for a compact two field period QAS with 20% external transform. These modes, which are resonant modes of the fixed boundary equilibrium, exhibit relatively delocalized, but not globally unstable, displacements (see Fig. 1). The radial shape and relative ordering of the largest amplitude Fourier components of unstable modes have been compared for coarse (49 surfaces) and fine grid (129 flux surfaces), as well as at values of $\beta = 6.7, 6.5, 6.4, 6.3, 6.0, 5.0\%$ with CAS3D and TERPSICHORE. Good agreement was found in every case. For example as shown in Fig. 1, at 6.7% beta and 48 flux surfaces CAS3D identified the five largest amplitude (m,n) components of the most unstable mode as (11,-5) (9,-3) (16,-7) (14,-5) (6,-3) while TERPSICHORE identified them as (11,5) (6,3) (9,3) (16,7) (14,5). The opposite signs in the toroidal Fourier indices originate from the different notations used in the Fourier representations. CAS3D uses $\cos(2\pi(m\theta+n\phi))$, while TERPSICHORE uses $\cos(2\pi(m\theta-n\phi))$. The poloidal and toroidal grids were not matched and are expected to account for the differences in ordering. Results from the two stability code packages for the marginal beta in fixed boundary equilibria (Fig. 2) are also in good agreement for this two field period QAS.

4. Calculations of Stability of the Kink and Periodicity-preserving Modes for Axisymmetric and Quasiaxisymmetric Configurations

The NCSX stellarator configuration [3] has been optimized for the stability of ballooning, kink and periodicity-preserving modes. TERPSICHORE has been used to show that high edge magnetic shear and appropriate boundary shaping can stabilize the kink mode in high bootstrap current QAS [4]. CAS3D has confirmed TERPSICHORE calculations [5] of stability for the kink and periodicity-preserving modes for the three field period, 50% external transform stellarator and extended them, finding stability even without a conducting wall.

TERPSICHORE has been benchmarked against an analytical solution for the critical wall position for vertical stability in a large aspect ratio tokamak with good agreement. In addition the vertical stability has been calculated for a series of zero beta equilibria interpolated between the present design and a tokamak equilibrium. The tokamak (terms with $n = 0$) is unstable. As nonaxisymmetric terms are added, the growth rate decreases, reaching zero about halfway to the present design. The periodicity-preserving mode stability thus appears robust. Calculations at zero beta were carried out because of difficulty converging the high beta, low transform tokamak equilibrium. Finite beta is found to stabilize this mode for the nonaxisymmetric equilibrium with the wall at $r = 4.5a$. (See Ref. 5).

CAS3D has calculated stability in NCSX for the kink ($N = 1$) and the periodicity-preserving ($N = 0$) modes, with a conducting wall at infinite distance from the plasma boundary. Figure 3 shows an analysis of local stability criteria for an equlibrium with a locally reduced pressure gradient. Pressure and iota profiles are shown, as well as the criteria for the local Mercier resonance instabilities. Most of these resonances are narrow, so that in their vicinity the Mercier term in the global stability can recover. However at the outside edge of the plasma, for $s > 0.6$, broad resonances occur and the Mercier term is unstable. Clearly the singular resonant currents are unphysical and improved physics models are needed to handle them properly. One approach to this is flattening of the pressure profile at the resonances. This reduces their width and stabilizes them. Without this pressure flattening, including the Mercier resonances in the global stability calculations leads to predictions of instability for both the kink and periodicity-preserving modes (Fig. 4).

CAS3D benchmarking calculations in two dimensions for the stability of the external kink for ARIES are in good agreement with predictions of TERPSICHORE and the PEST [6] codes. Table I shows the PEST comparisions with CAS3D and TERPSICHORE for kink stability for this axisymmetric equilibrium. The CAS3D vertical stability calculations of the axisymmetric case show instability for elongated tokamaks, and stability for circular tokamaks (Table II). The most unstable harmonics of the vertical instability for the ARIES axisymmetric tokamak at 7.5% beta for $m > 1$ are suppressed at lower beta (2.1%).

There remain questions concerning the best current and pressure profiles to use for design optimizaton. Most stellarator density profiles are broader than the ARIES profiles assumed in initial studies for NCSX. Also the current profile was assumed to be similar to a low collisionality reactor bootstrap current profile, to enable rapid reactor performance scaling. Work is ongoing to address flexible performance in a modest-sized experiment.

5. Conclusion

Optimized configurations have been identified for the proposed NCSX experiment which are stable to ballooning, kink and the periodicity-preserving modes and have acceptable confinement. Neoclassical particle transport is being studied and optimized for good confinement [7]. The three dimensional global ideal MHD stability code packages CAS3D and TERPSICHORE are found in agreement in numerous benchmarking studies and both predict global stability for the NCSX design point configuration. CAS3D has extended TERPSICHORE calculations for NCSX showing stability of the kink and periodicity-preserving modes for this stellarator even without a conducting wall. There is still a need for comprehensive comparisons of detailed measurements of MHD instabilities to results of global stability calculations for both rippled tokamak and stellarator experiments.

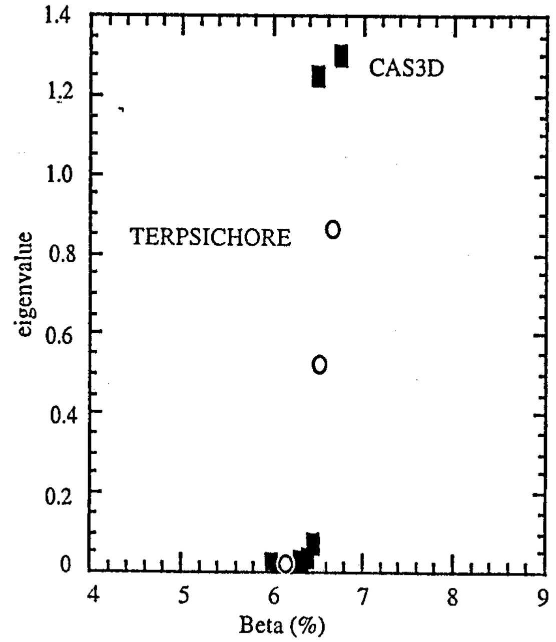

Fig. 2. Marginal beta point for QAS2_20 found by CAS3D (solid squares) and TERPSICHORE (open circles) is 6.5% beta. TERPSICHORE eigenvalues are multiplied by 20; the two codes are normallized differently.

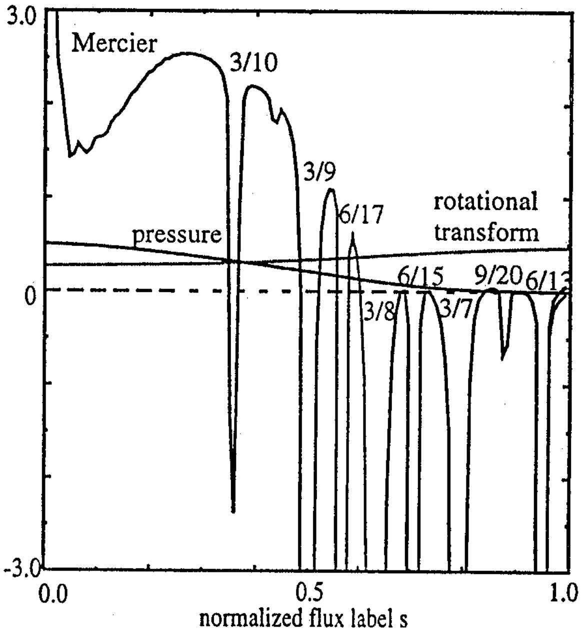

Fig. 3 Local stability profiles for QAS3_C82, showing pressure (10x),rotational transform, and Mercier stability (positive for stability).

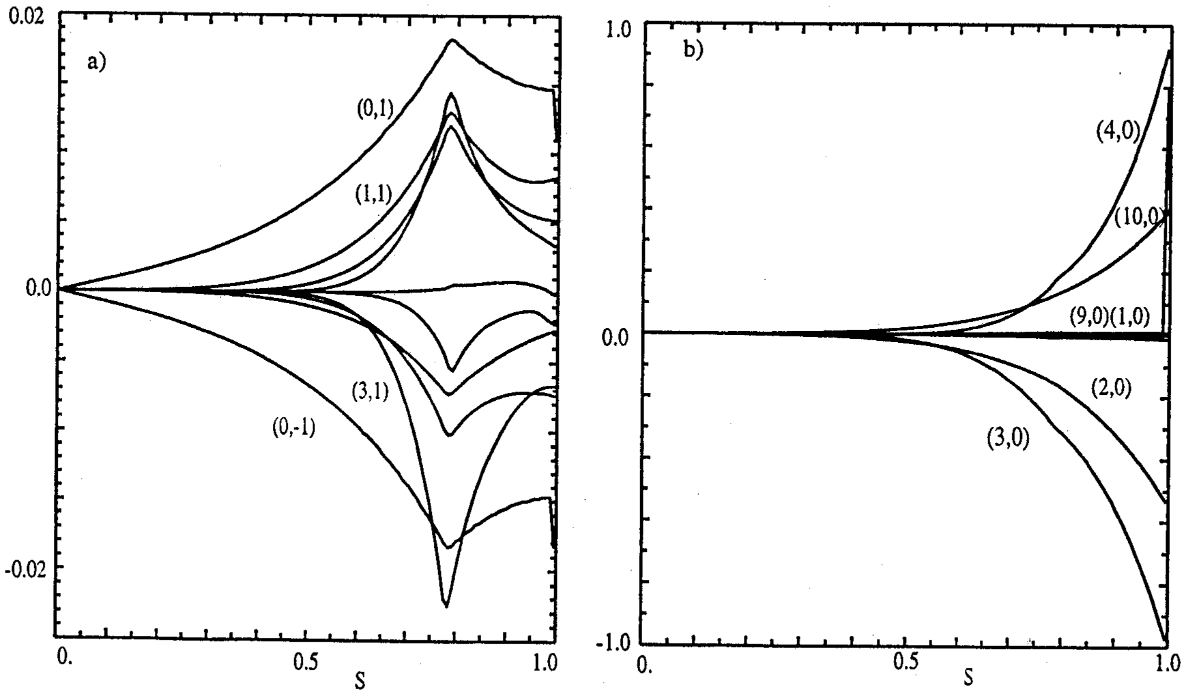

Fig. 4. Largest Fourier components of a) the N=1, kink mode instability and b) the N=0, vertical or axisymmetric mode instability for QAS3_C82 as calculated from CAS3D if natural resonances, Mercier instabilities, are not eliminated. Simulation parameters: 25 modes, 128 flux surfaces.

* Supported by the US Dept. of Energy Contract DE-AC02-76CH03073.

[1] C. Nuehrenberg, Phys. Plas. **3**, 2401 (1996). C, Schwab Phys.Fluids B **5**, 3195 (1993).
[2] W. A. Cooper, *et al.*, Phys. Plas. **3**, 275, (1996).
[3] A. H. Reiman, "Physics Design of a High Beta Quasi-axisymmetric Stellarator", this conference, paper TL18.
[4] G. Y. Fu, *et al*, IAEA-CN-69/THP1/07, 17th IAEA Fusion Energy Conf., Yokahama, 1998.
[5] G. Y. Fu, *et al*, "Ideal MHD Stability in High Beta Current-Carrying Quasi-axisymmetric Stellarators", in preparation.
[6] R. C. Grimm, *et al.*, Meth. in Comput. Phys. **16**, 273 (1975).
[7] M. H. Redi, *et al*, Phys. Plas. in press (Sept., 1999).

Table I ARIES Kink Stability

β	CAS3D	PEST	TERPSICHORE	PEST
(%)	(wall at infinity)		(wall at r=2a)	
7.5	unstable	unstable	unstable	unstable
3.6	unstable	unstable	unstable	unstable
2.5	unstable	unstable	stable	stable
2.1	stable	stable	stable	stable

Table II ARIES Vertical Stability

β	eigenvalue
elongated	
7.5%	-0.041
3.5	-0.076
2.5	-0.089
2.1	-0.094
circular	
0.7	-3.10^{-12}

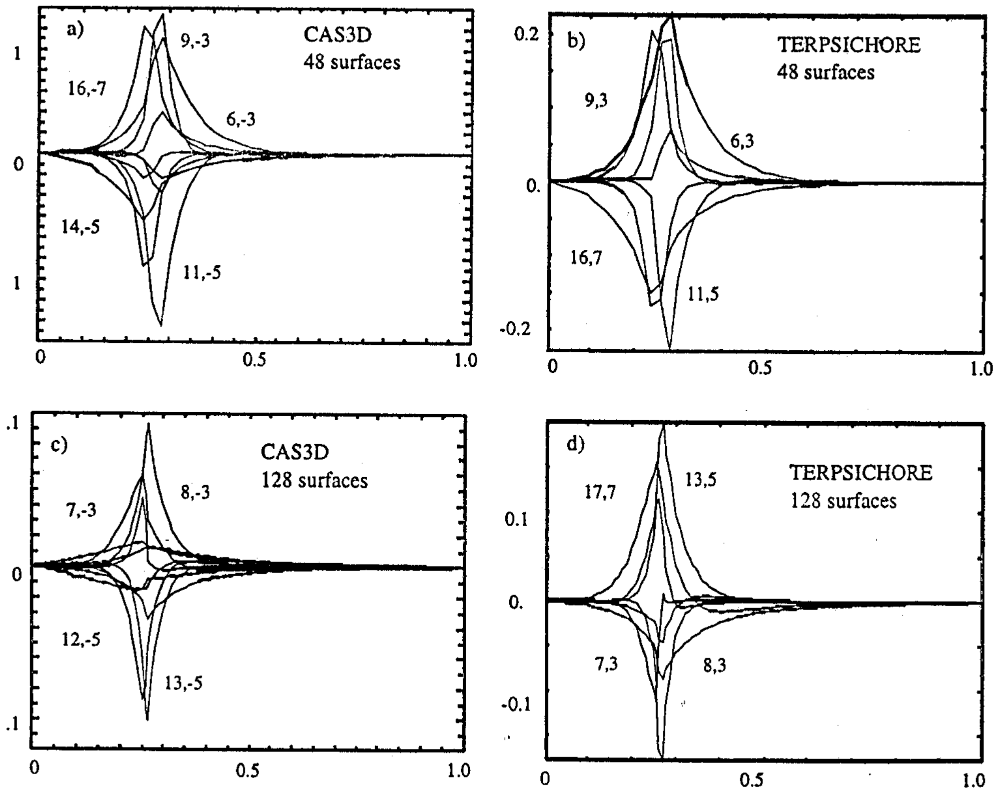

Fig. 1 Largest Fourier components of most unstable mode calculated for QAS2_20 at 6.7% beta, for 48 flux surfaces (a)$\lambda = -1.3$) and 129 flux surfaces (c)$\lambda = -0.35$) by CAS3D, and foı 48 flux surfaces, (b)$\lambda = -0.02$ and for 129 flux surfaces (d)$\lambda = -0.007$ by TERPSICHORE .

Physics Design of a High β Quasi-Axisymmetric Stellarator

A. Reiman[1], G. Fu[1], S. Hirshman[4], L. Ku[1], D. Monticello[1], H. Mynick[1], M. Redi[1], D. Spong[4], B. Blackwell[8], A. Boozer[5], A. Brooks[1], W. A. Cooper[2], M. Drevlak[3], R. Goldston[1], J. Harris[8], M. Isaev[9], Z. Lin[1], J.F. Lyon[4], P. Merkel[3], M. Mikhailov[9], W. Miner[6], N. Nakajima[7], G. Neilson[1], C. Nührenberg[3], M. Okamoto[7], N. Pomphrey[1], W. Reiersen[1], R. Sanchez[4], J. Schmidt[1], A. Subbotin[9], P. Valanju[6], K. Y. Watanabe[7], R. White[1], M. Zarnstorff[1]

[1]*Princeton Plasma Physics Laboratory, Princeton NJ 08543, USA*
[2]*CRPP-PPB, CH-1015 Lausanne, Switzerland*
[3]*IPP-Euratom Association, D-17491 Greifswald, Germany*
[4]*Oak Ridge National Laboratory, Oak Ridge, Tennessee 37831-8070, USA*
[5]*Dept. of Applied Physics, Columbia University, New York, NY 10027, USA*
[6]*University of Texas at Austin, Austin, TX 78712-1081, USA*
[7]*National Institute for Fusion Science, Nagoya, Japan*
[8]*Plasma Research Laboratory, Australian National University, Canberra, Australia*
[9]*Kurchatov Institute, Moscow, Russia*

Abstract

Key physics issues in the design of a high β quasi-axisymmetric stellarator configuration are discussed. The goal of the design study is a compact stellarator configuration with aspect ratio comparable to that of tokamaks and good transport and stability properties. Quasi-axisymmetry has been used to provide good drift trajectories. Ballooning stability has been produced by strong axisymmetric shaping. A combination of externally generated shear and nonaxisymmetric corrugation of the plasma boundary provides stability to external kink modes even in the absence of a conducting wall. The resulting configuration is also found to be robustly stable to vertical modes, increasing the freedom to do axisymmetric shaping. Stability to neoclassical tearing modes is conferred by a monotonically increasing ι profile. A gyrokinetic δf code has been used to confirm the adequacy of the neoclassical confinement. Neutral beam losses have been evaluated with Monte Carlo codes.

1. Introduction

We have been pursuing the design of a compact stellarator configuration with aspect ratio comparable to that of tokamaks ($R/\langle a\rangle \approx 3.5$) and good transport and stability properties. To provide good drift trajectories, we have focused on configurations that are close to quasi-axisymmetric (QA).[1, 2] This paper discusses key physics issues that have been addressed in our study.

The QA configurations being studied have drift trajectories similar to those of tokamaks, aspect ratios comparable to those of tokamaks, and bootstrap current as well as $n = 0$ components of ellipticity and triangularity comparable to that of advanced tokamaks. They therefore can be considered to be hybrids between drift-optimized stellarators and advanced tokamaks. Relative to unoptimized stellarators, they have improved predicted neoclassical confinement. They have a much smaller aspect ratio than the drift-optimized stellarators under construction. Strong axisymmetric components of shaping provide good ballooning stability properties at the lower aspect ratio. The bootstrap current, large relative to that of other drift-optimized stellarators, is used to advantage in suppressing magnetic islands and providing a substantial fraction of the rotational transform. An experimental study of the potential benefits and disadvantages of bootstrap currents would be a key focus of a proposed QA stellarator experiment.

Relative to advanced tokamaks, QA configurations have the potential advantage that the externally generated transform reduces or eliminates the need for rf current drive and provides control over MHD stability properties. Unlike the tokamak, it is possible to have a monotonically-increasing ι profile (monotonically decreasing q profile), avoiding problems associated with MHD stability at the shear reversal layer, and conferring stability to neoclassical tearing modes across the entire cross section. A combination of externally generated shear and nonaxisymmetric corrugation of the plasma boundary provides stability to external kink modes even in the absence of a conducting wall. The resulting configuration is found to be robustly stable to vertical modes. Experiments on hybrid tokamak-stellarator configurations on W7A and CLEO found that even a modest level of externally generated transform was sufficient to suppress disruptions.[3, 4].

Section 2 of this paper describes an approximately quasi-axisymmetric configuration that we call Configuration C82, and discusses some of its properties. Section 3 discusses the issues of kink, vertical, and ballooning stability. Section 4 discusses neoclassical confinement of thermal and energetic particles.

2. An Approximately Quasi-Axisymmetric Configuration

Figure 1 shows the plasma boundary of an approximately quasi-axisymmetric, three-period configuration that we call Configuration C82. The choice of aspect ratio ($R/\langle a\rangle \approx 3.4$) has been constrained by the desire to fit the configuration inside the PBX-M tokamak toroidal field (TF) coils. We envision constructing a device that would reuse the PBX TF coils to produce the main component of the toroidal field, and would have an additional set of saddle coils inside the TF coils to produce the residual three-dimensional field. Configuration C82 is the most recent of a set of configurations that have been generated through a design procedure that uses an optimizer to adjust the values of about 40 parameters specifying the shape of the plasma boundary to target desired configuration properties.

The configuration optimization is performed using a Levenberg-Marquardt scheme to minimize a target function, χ^2, which is a sum of squares of desired targets.[5] Targets incorporated in the optimizer include: a measure of quasi-axisymmetry (the sum of the squares of the non-axisymmetric Fourier components of B in Boozer coordinates, with an adjustable weighting of contributions from different flux surfaces); a measure of secondary ripple wells along the field lines[6]; the eigenvalue of the most unstable external kink mode; ballooning eigenvalues; the deviation of major radii of inner and outer boundaries from those prescribed by the PBX geometry; the deviation of the rotational transform from prescribed values at on one or two flux surfaces. Configurational properties (MHD equilibria) are completely determined by the current and pressure profiles, as well as the plasma boundary, which is represented as a finite sum of Fourier harmonics for R and Z. Varying these as independent variables in the optimizer allows us to seek stellarator configurations which minimize χ^2 and thereby approach a state in which the various criteria are satisfied as well as possible. The VMEC code[7] is used to calculate the MHD equilibria needed to evaluate the physics targets for arbitrary values of the independent variables. The attainment of an optimized state has been accelerated by introducing a condensed spectrum for the boundary. For configuration C82, 6 poloidal modes and 3 toroidal modes were used in the plasma boundary description, resulting in 39 independent variables adjusted by the optimizer. The optimization process typically used 94 modes and 33 radial grid surfaces for its VMEC calculations. Kink eigenvalue calculations in the optimizer use the TERPSICHORE code.[8]

A tokamak equilibrium from the Aries reactor study[9] was used as the starting point of the optimization procedure. This starting point has an advantage that it has good ballooning stability properties. Also, we initially retain the bootstrap-like current profile as well as the pressure profile of the Aries equilibrium. The β limit for the Aries configuration is 4.5%, and we fix β at 4% for the purposes of our optimization study. We assume a broader density profile than that used in the Aries study, and the magnitude of the bootstrap current is consequently reduced. The pressure and current profiles are held fixed in the optimization process, along with the total toroidal flux. The initially axisymmetric equilibrium is of course quasi-axisymmetric, and we use the optimizer to maintain approximate quasi-axisymmetry as we deform the boundary to introduce an externally generated rotational transform. In order to avoid difficulties associated with local optima in the optimizer target function, the modification of the Aries equilibrium to produce configuration c82 was done in four stages. In the initial stage, the value of ι at the magnetic axis and and the plasma edge were targeted, as well as the quasi-axisymmetry. By this means, an approximately uniform external transform was added to the axisymmetric configuration until, on average, it accounted for about 30% of the total. Only the $n \neq 0$ terms were varied at this stage. The weight placed on the ripple measure in the target function was adjusted to reduce the magnitude of individual Fourier components of B to less than a few percent. The resulting ι profile was non-monotonic, with a region near the edge where $\iota' < 0$. In the second stage of the optimization procedure, the value of ι was constrained at a point in the plasma interior and at the plasma edge, and the value at the edge was raised to make the profile monotonic. The value of ι at the axis was not constrained during this second stage of optimization, and it decreased somewhat. The non-axisymmetric magnetic field components were also further reduced at this stage. For the third stage of the procedure, the kink stabilization was turned on in the optimizer target function, retaining the constraints on quasi-axisymmetry and on the value of ι at the edge. The $n = 0$ terms now were allowed to vary (with the aspect ratio being constrained). The reduction of secondary ripple wells was also done at this stage. Finally, after kink stabilization, we find that the ballooning beta limit has been lowered, and is now exceeded locally by the pressure gradient in a narrow region near the outside. This requires a local reduction in p' in that region. (The initially adopted Aries profile has a relatively large pressure gradient near the edge.) The final pressure profile is shown in Figure 2. The coordinate s is the toroidal flux normalized to its value at the boundary.

The sign of the shear in configuration C82 has been chosen such that the perturbed bootstrap currents suppress magnetic islands. This stabilizing effect is the inverse of the neoclassical tearing instability that has been seen in tokamak experiments. The rotational transform profile of configuration C82 is shown in figure 3. It ranges from about 0.25 on the axis to about 0.47 at the edge. Also shown is the vacuum transform generated by the three-dimensional shaping alone. In the absence of this externally generated transform, ι would be decreasing in a region outside the current density peak. The externally generated transform allows us to generate a monotonically increasing ι. In tokamak parlance, $q' < 0$ ($\iota' > 0$) is known as "reverse shear". Reversed shear tokamaks have a shear reversal layer which tends to be associated with MHD stability problems, and outside of which neoclassical tearing modes are unstable.

Figure 4 shows the nonaxisymmetric Fourier components of B in Boozer coordinates, as a function of the radial coordinate, for configuration C82. In the quasi-axisymmetric limit, these Fourier modes would vanish. In our design process, we have used an optimizer to suppress these mode amplitudes. The boundary prescription of configuration c82 has an m=2, n=1 Fourier

2

mode of amplitude 0.126. This term helps to produce the desired externally generated shear. Its amplitude may be compared with that of the m=2, n=1 Fourier component of B (the largest nonaxisymmetric component), which is only 0.7% at s=0.5 (relative to the $m = 0$, $n = 0$ component), rising to 3.5% at the edge.

In the remainder of this paper we discuss some key physics issues in more detail. Section 3 discusses ideal MHD stability issues. Section 4 discusses confinement issues.

3. Ideal MHD Stability

As discussed in the previous section, the sign of ι' in configuration C82 confers stability to neoclassical tearing modes. In this section we discuss ballooning, kink and vertical stability. These three issues are not independent. We use a combination of externally generated shear and an appropriate corrugation of the plasma boundary to stabilize external kink modes. We have found that the resulting configurations are also robustly stable to vertical modes. The vertical stabilization, in turn, extends our freedom to use axisymmetric shaping to stabilize ballooning modes. The stability of ballooning, external kink, and vertical modes has been calculated using the TERPSICHORE[8] suite of codes. More details on the kink and vertical stability calculations will be reported in [15].

As previously reported[10, 11], we have found that ballooning modes can be stabilized in quasi-axisymmetric stellarators by appropriate axisymmetric shaping. The resulting strong axisymmetric component of shaping is a unique feature of our configurations relative to other stellarators, and is visible in fig. 1. (Note that the average of the ellipticity and triangularity as a function of the toroidal angle does not vanish.) The ARIES tokamak equilibrium that serves as the starting point for the design procedure provides initial $n = 0$ components of shaping that are strongly stabilizing for ballooning.

The ARIES tokamak equilibrium that serves as our starting point for the design of configuration c82 requires a conducting wall at $1.3a$, where a is the minor radius, to stabilize the external kink. The external kink has been stabilized in configuration c82 with the wall at infinity. To accomplish this, we have used a combination of externally generated shear and a three-dimensional corrugation of the boundary with little associated shear.

The potential use of externally generated shear to stabilize kink modes was suggested in several early papers.[12, 13] Our calculations confirm that the external kink in our quasi-axisymmetric configurations can be stabilized by this method.[14] However, we find that when externally generated shear alone is used to stabilize the kink this forces the value of ι in the plasma interior to undesirably low values. This is particularly an issue for a reverse shear configuration of the size we could like to construct, where the axisymmetric neoclassical confinement time does not exceed the total confinement time by a large margin, so that a reduction in the total poloidal flux poses confinement problems. The development of a second kink stabilization scheme to augment the effect of the externally generated shear has therefore been key in allowing us to generate attractive kink stable configurations. The second method of stabilization employs a three-dimensional corrugation of the plasma boundary with little associated shear. The corrugation is generated using the optimizer, with the kink growth rate calculated by TERPSICHORE incorporated in the target function. The optimizer adjusts the shape of the plasma boundary to suppress the kink.

For calculating global ideal MHD stability, the TERPSICHORE code uses finite elements in the radial direction and Fourier decomposition in the poloidal and toroidal angles. For our kink calculations, the typical numerical resolutions used are 48 radial grid surfaces, 264 equilibrium Fourier modes in Boozer coordinates and 91 stability Fourier modes. Systematic convergence studies show that this resolution is sufficient for accurate prediction of beta limit due to external kink modes. Up to 96 radial grid surfaces and 131 stability Fourier modes have been used.

With the ARIES pressure and current profiles, as described in Section 2, configuration c82 is marginally stable to external kink modes at $\beta = 3.9\%$. Figure 5 shows the dependence of the kink stability on the magnitude of the current. The configuration becomes increasingly stable to the external kink at lower current, and less stable at higher current. This is in contrast to the conventional tokamak, in which the kink β limit increases with increasing current. This can be understood in terms of the shear. In our configuration, the externally generated shear is fighting that due to the current near the edge. Increasing the current decreases the net shear near the edge. In a conventional tokamak equilibrium, on the other hand, the shear increases with increasing current. When the plasma current in configuration C82 is sufficiently large, an $\iota = .5$ surface moves into the plasma, and the configuration becomes unstable to a current driven mode at zero β, as can be seen in Figure 5.

The "vertical instability" in our configuration is nonaxisymmetric, unlike that in a tokamak, because of the mode coupling through the nonaxisymmetric equilibrium Fourier modes. We distinguish this type of instability from the external kink by its preservation of the periodicity of the equilibrium. Kink modes, in contrast, preserve the stellarator symmetry, but not the periodicity. The two types of modes do not couple in δW, so that their stability can be calculated independently.

The vertical mode is calculated to be stable in configuration c82 at the reference β value of 3.9%. The calculation was done with a wall at $3.5a$, where we believe it is has virtually no effect on stability. A tokamak having the same $n = 0$ components of boundary shape is unstable. We interpret the stabilization as due to the nonaxisymmetric shaping. To study this effect, the vertical stability has been calculated for a sequence of zero β equilibria interpolating between the tokamak and C82. The $n \neq 0$ components of the shape are linearly interpolated between the tokamak (zero amplitude) and their full value in configuration C82. The results are shown in Figure 6. About 60% of the three-dimensional shaping is adequate to stabilize the vertical mode. Finite β effects are found to be stabilizing. We conclude that the vertical mode is robustly stable.

The robust stability of the vertical mode allows us to further increase the elongation of our configuration. This provides additional flexibility in shaping the configuration to maintain ballooning stability. The potential usefulness of this is being explored.

The corrugation introduced to stabilize the kink mode causes a deterioration in the ballooning stability. As described in Section 2, this requires a modest reduction of p' in the region $0.8 < s < 0.9$ relative to the initially adopted ARIES profile, with the resulting pressure profile shown in figure 2. The corresponding ballooning eigenvalues for this pressure profile are plotted in figure 7 as a function of the radial coordinate. In the narrow region near the edge where the pressure profile has been modified, the ballooning eigenvalues approach marginal stability. Away from this region, the ballooning mode is robustly stable.

4. Neoclassical Confinement

Our numerically generated configurations are only approximately quasi-axisymmetric. In designing the configurations, it is necessary to monitor the neoclassical transport to confirm that the degree of quasi-axisymmetry is adequate. In this section we discuss calculations of neoclassical confinement of thermal particles and of neutral beams. The parameters are chosen to be appropriate for a device constructed in the PBX facility, $R \approx 1.45$ m.

Thermal neoclassical transport evaluations have been done using the GTC code[16] running on the T3E. GTC can do both full-f and δf calculations in general toroidal geometry, and can run in either turbulence mode (self–consistent electrostatic fluctuations computed) or neoclassical mode (only specified magnetic and electrical fields), with like–particle collisions for ions, and like-particle plus electron-ion collisions for electrons. Calculations for NCSX thus far have used only the neoclassical mode.

The simulations used for these assessments of thermal transport used 40×10^3 Deuterium ions, loaded according to temperature and density profiles drawn from the PBX database, with $T_{i0} = 2.14$ keV, $n_{e0} = .67 \times 10^{14}$, and B=1.26 Tesla. A model ambipolar potential Φ is used, given by $e\Phi/T_{i0} = \alpha\psi/\psi_{\rm edge}$, with $2\pi\psi$ the toroidal flux, and α an adjustable amplitude. These runs used $\alpha = 1$, hence $e\Phi \approx T_i$. GTC was run in neoclassical, full-f mode, and the confinement time τ_E computed from $\tau_E(r) = W(r)/[-d_tW(r) + S_E(r)]$, with $W(r)$ the ion energy contained inside flux surface r, and $S_E(r)$ the energy source/sink, computed from the energy exchange of the test ions off the fixed–profile background.

At $r = a$ ($\psi = \psi_{\rm edge}$), we find $\tau_{Ei} = 16.9$ msec for configuration c82. Since the electron heat loss channel is negligible, the neoclassical energy confinement time is $\tau_{\rm E}^{nc} \approx (1 + W_e/W_i)\tau_{\rm Ei}^{nc}$. For $Z_{\rm eff} = 2$, this gives $\tau_{\rm E}^{nc} \approx 2.3\tau_{\rm Ei}^{nc} \approx 39$ ms. For these parameters, $\tau_{\rm ISS} \simeq 7.6$ msec. An enhancement factor of 2.3 would give a confinement time of 17.5 ms. This is still well below the neoclassical confinement time, so the neoclassical losses are predicted to be sufficiently small to not have a significant deleterious effect on the energy confinement.

Neutral beam heating efficiency has been calculated by following a collection of simulation particles through several slowing-down times with the DELTA5D code[17]. These particles are initially distributed in space according to a deposition profile calculated by TRANSP[18] for an equivalent axisymmetric configuration; the initial pitch angle distribution is determined based on the ratio of the tangency radius to the birth major radius (pencil beam approximation). The Hamiltonian guiding center beam particle orbits are then followed in the presence of collisions with electrons and two background ion species (a main ion and one impurity component). As the beam ions slow down to $3/2kT_{\rm ion}$ with $T_{\rm ion}$ the background field ion temperature, they are removed from the fast ion distribution and counted as part of the field plasma. Beam heating efficiencies are calculated by recording the losses of particles and energy out of the outer magnetic flux surface that occur during the slowing-down process. The DELTA5D code runs groups of beam particles on different processors in parallel on the Cray T3E using the MPI language for inter-processor communication. A variety of diagnostics of the escaping particles, such as pitch angle, energy and particle lifetime distributions, are retained to aid in understanding the loss mechanisms. These generally show a prompt loss peak at the beam injection energy and pitch angle, followed by a more gradual loss centered around $v_{\|}/v = 0$ and at around 1/5 of the injection energy as the beam particles scatter onto trapped orbits. We also have made studies of the dependence of these losses on the magnetic field and find non-monotonic behavior in beam energy losses with increasing magnetic field strength. This type of behavior is to be expected with the presence of stochastic loss regions. Contours of the longitudinal adiabatic invariant J indicate that such loss regions can be present for barely passing particles near the plasma edge.

This model has been applied to the calculation of neutral beam energy losses for the c82 configuration, with the background plasma taken to have a central electron density of 6.5×10^{13} cm^{-3}, and central temperatures of 1.9 keV for the ions, and 2.1 keV for the electrons. The background impurity species was oxygen ($Z = 8$, mass/proton mass= 16) with $n_{\text{impurity}}/n_{\text{electron}} = 0.014$ leading to a Z_{eff} of 1.8. The beam consisted of 50 keV hydrogen ions injected on the midplane at $\theta = 0$, $\phi = 0$. This resulted in saturated (over several slowing-down times) beam energy losses of 34% for $\langle B_0 \rangle = 1$T and 28% for $\langle B_0 \rangle = 1.5$T.

Energetic ion losses have also been calculated using the ORBITMN code, a modification of the ORBIT code[19] which is capable of handling three-dimensional equilibria. Simulations of α particle confinement using the ORBIT code show good agreement with detailed experimental measurements on TFTR.[20] The predictions of ORBITMN are consistent with those of DELTA5D.

5. Conclusions

The design of an attractive quasi-axisymmetric stellarator has required the development of novel techniques for stabilizing ballooning and kink modes. Ballooning modes have been stabilized through axisymmetric shaping, not previously applied to stellarators. Kink modes have been stabilized through a combination of externally generated shear and a three-dimensional corrugation of the boundary. The solution of these problems opens up a promising new region of configuration design space. MHD stabilized quasi-axisymmetric stellarators combine some of the most attractive features of drift-optimized stellarators and advanced tokamaks.

The confinement predictions of Section 4 suggest that an $R = 1.45$ m device based on the c82 configuration would require about 5.5 MW of neutral beam power to access 4% β with $B = 1.2$ T, $n = 10^{20}$m^{-3}, $T_0 = 1.4$ keV. The PBX facility has 6 MW of neutral beam power available. Such a device would therefore be capable of testing the novel schemes for stabilizing ballooning, kink, and vertical modes described in Section 3. The experiment would more generally provide information on MHD stability, disruption immunity, and confinement in a compact quasi-axisymmetric stellarator operating near the β limit, including the potentially stabilizing effects of bootstrap currents on magnetic islands.

Acknowledgments

This research was partially sponsored by the US Department of Energy under contract No. DE–AC02–76–CHO–3073, by the Fonds National Suisse de la Recherche Scientifique and by Euratom.

References

[1] J. Nührenberg, W. Lotz, and S. Gori, in *Theory of Fusion Plasmas*, E. Sindoni, F. Troyon and J. Vaclavik eds., SIF, Bologna, 1994

[2] P.R. Garabedian, *Phys. Plasmas* 3, 2483 (1996).

[3] W VII-A Team, Nucl. Fusion 20, 1093 (1980).

[4] D. C. Robinson and T. N. Todd, Phys. Rev. Letters 48, 1359 (1982).

[5] D. A. Spong, S. P. Hirshman, J. C. Whitson, et. al., Phys. Plasmas 5, 1752 (1998)

[6] M. Yu. Isaev, M. I. Mikhailov, D. A. Monticello, H. E. Mynick, A. A. Subbotin, L. P. Ku , A. H. Reiman, accepted for pulication in Phys. Plasmas.

[7] S. P Hirshman, W. I. van Rij, and P. Merkel, Comput. Phys. Commun. 43, 143 (1986).

[8] D.V. Anderson, A. Cooper, U. Schwenn and R. Gruber, *Linear MHD Stability Analysis of Toroidal 3D equilibria with TERPSICHORE* in "Theory of Fusion Plasmas," J. Vaclavik, F. Troyon and E. Sindoni eds. (Soc. Ital. Fisica – Editrice Compositori, Bologna, 1988) pp. 93–102

[9] S.C. Jardin, C. E. Kessel, C.G. Bathke, D.A. Ehst, T.K. Mau, F. Najmabadi, T.W. Petrie, "Physics Basis for a Reversed Shear Tokamak Power Plant", Fusion Engr. and Design, vol. 38, (1997), 27.

[10] A. Reiman, R. Goldston, L. Ku, D. Monticello, H. Mynick, G. Neilson, M. Zarnstorff, I. Zatz, W. Cooper, and A. Boozer, J. Plasma Fusion Res. SERIES **1**, 429 (1998).

[11] A. Reiman, L. Ku, D. Monticello, H. Mynick, and the NCSX Configuration Design Team, 1999 Fusion Energy Proc. 17th Int. Conf. (Yokohama, 1998) (Vienna: IAEA)

[12] V. V. Drozdov, M. Yu. Isaev, M. I. Mikhailov, V. D. Pustovitiov, and V. D. Shafranov, in Plasma Physics and Controlled Nuclear Fusion Research 1988 (Proc. 12th Int. Conf. Nice, 1988), Vol. 2, IAEA, Vienna (1989) 611.

[13] J. L. Johnson et al, Phys. Fluids **1**, 281 (1958); R. M. Sinclair et al, Phys. Fluids **8**, 118 (1965); K. Matsuoka et al, Nuclear Fusion **17**, 1123 (1977).

[14] G. Fu, L. Ku, N. Pomphrey, M. Redi, C. Kessel, D. Monticello, A. Reiman, M. Hughes, W. Cooper and C. Nuehrenberg, 1999 Fusion Energy Proc. 17th Int. Conf. (Yokohama, 1998) (Vienna: IAEA)

[15] G.Y. Fu et al,Ideal MHD stability in high beta current-carrying quasi-axisymmetric stellarators, in preparation.

[16] Z. Lin, T.S. Hahm, W.W. Lee, W.M. Tang, R.B. White, *Science* **281**, 1835 (1998).

[17] D.A. Spong, S.P. Hirshman, D.B. Batchelor, J.F. Lyon, "Plasma Transport and Energetic Particle Confinement Studies in Low Aspect Ratio Quasi-Omnigenous (QO) Stellarators"Bulletin of the American Physical Society, Abstract KP01.45, March 20-26, 1999, Atlanta, GA.

[18] R.J. Hawryluk in Physics of Plasmas Close to Thermonuclear Conditions, ed. by B. Coppi, et al., (CEC, Brussels, 1980), Vol. 1, p. 19.; R.J. Goldston et al., J. Comp. Phys. 43 (1981) 61.

[19] R. White and M. Chance, Phys Fluids 25, 575 (1982); R. White, Phys Fluids B 2, 575 (1990).

[20] "Neoclassical Simulations of Fusion Alpha Particles in Pellet Charge Exchange Experiments on the Tokamak Fusion Test Reactor", M. H. Redi S. H. Batha, R. V. Budny, D. S. Darrow, F. M. Levinton, D. C. McCune, S. S. Medley, M. P. Petrov, S. vonGoeler, R. B. White, M. C. Zarnstorff, S. J. Zweben, Phys. Plas., in press (1999).

[21] "Energetic Particle Confinement in Compact Quasiaxial Stellarators" M. H. Redi, H. E. Mynick, M. Suewattana, R. B. White, M. C. Zarnstorff, Phys. Plas, in press (1999).

Figures

Fig. 1 Plasma boundary of Configuration C82.

Fig. 2 Pressure profile. The coordinate s is the toroidal flux normalized to its value at the boundary.

Fig. 3 Rotational transform profile of Configuration C82.

Fig. 4 Largest nonaxisymmetric Fourier coefficients of B for Configuration C82, normalized to $n = 0$, $m = 0$ Fourier component.

Fig. 5 Kink stability of Configuration C82 with varying β and current. Open circles correspond to stable equilibria, filled circles to unstable equilibria.

Fig. 6 Vertical stability eigenvalues calculated by TERPSICHORE for a sequence of equilibria interpolating between Configuration C82 and a corresponding tokamak.

Fig. 7 Ballooning eigenvalues as a function of radial coordinate for the modified pressure profile.

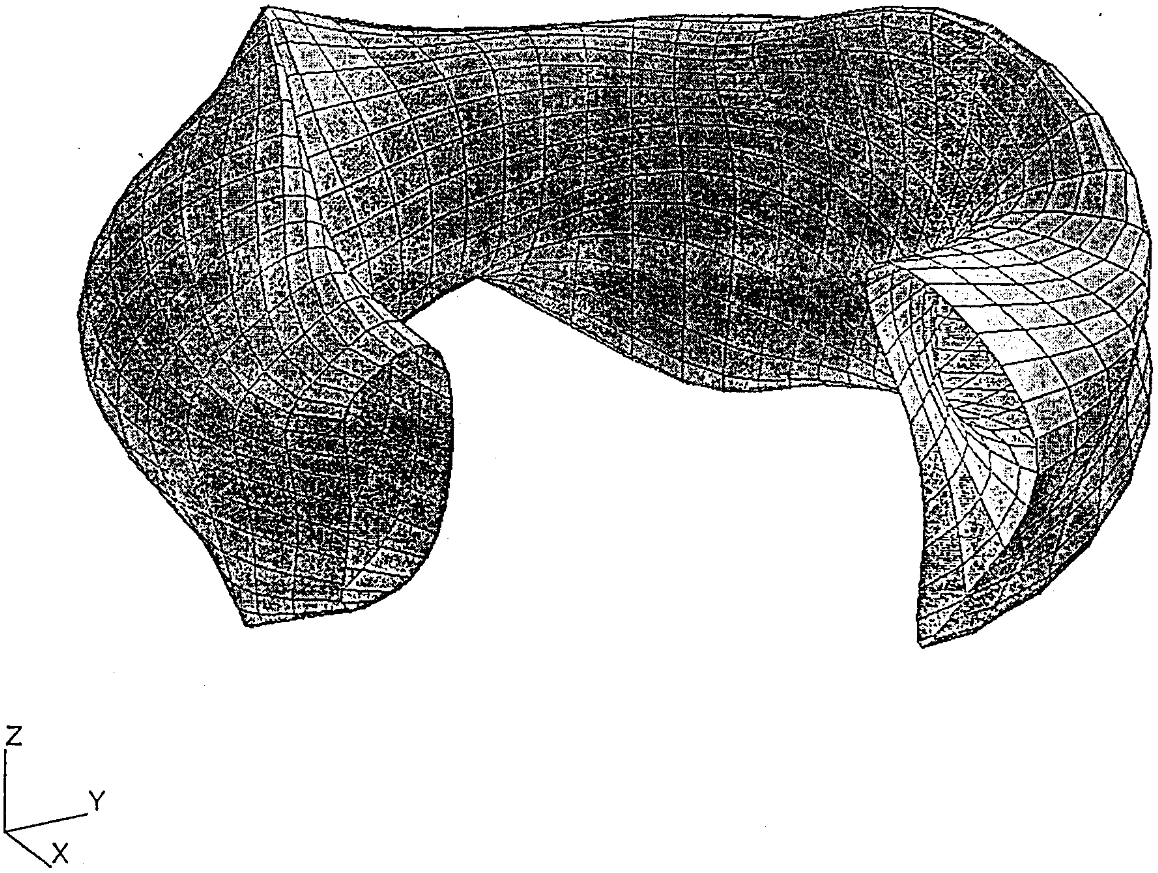

Figure 1:

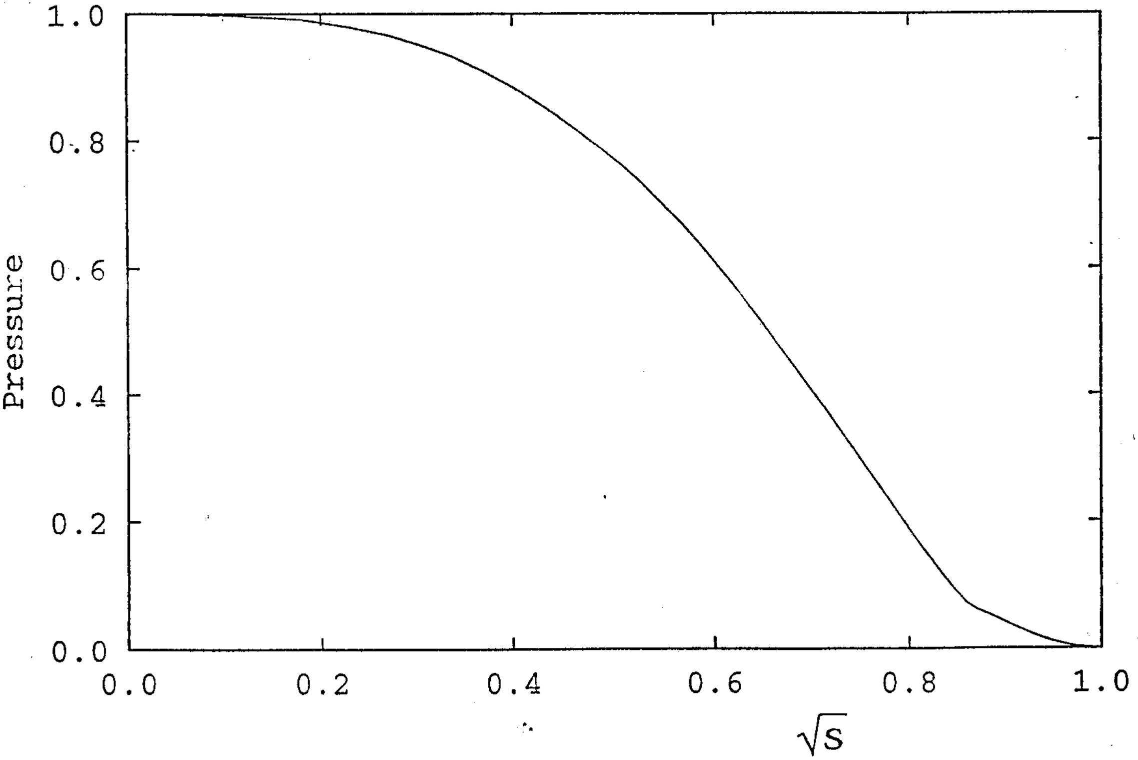

Figure 2:

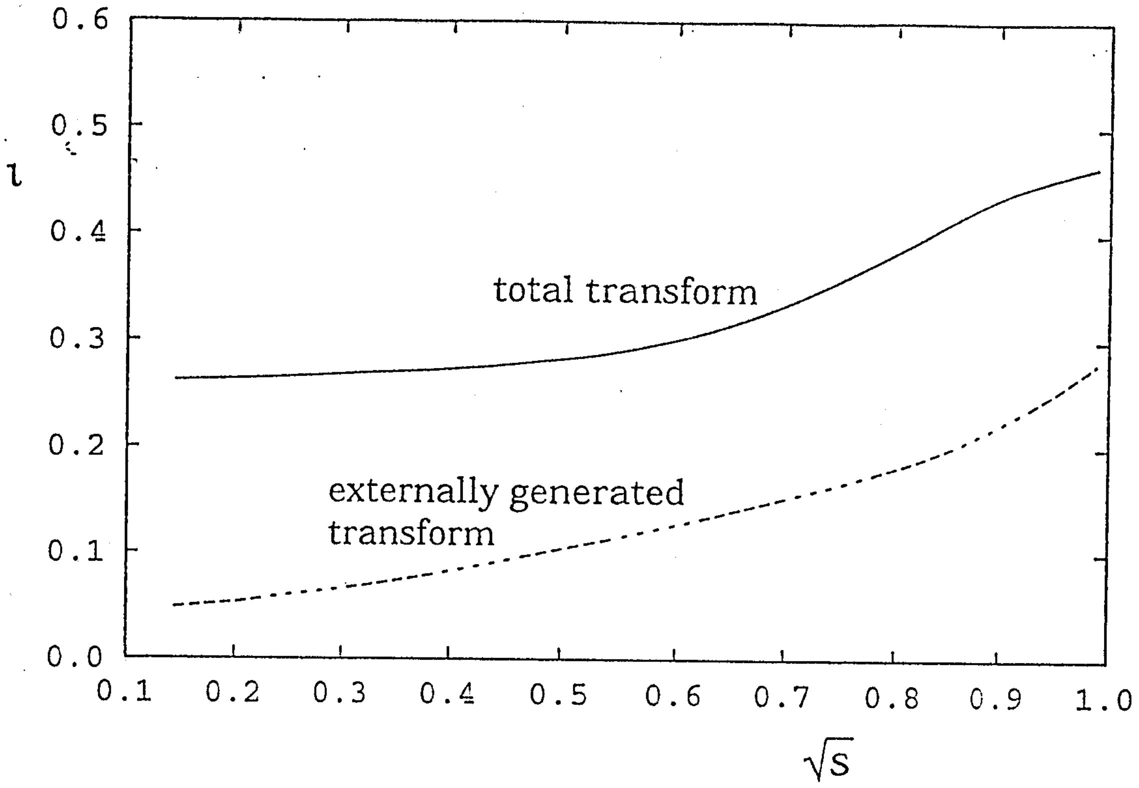

Figure 3:

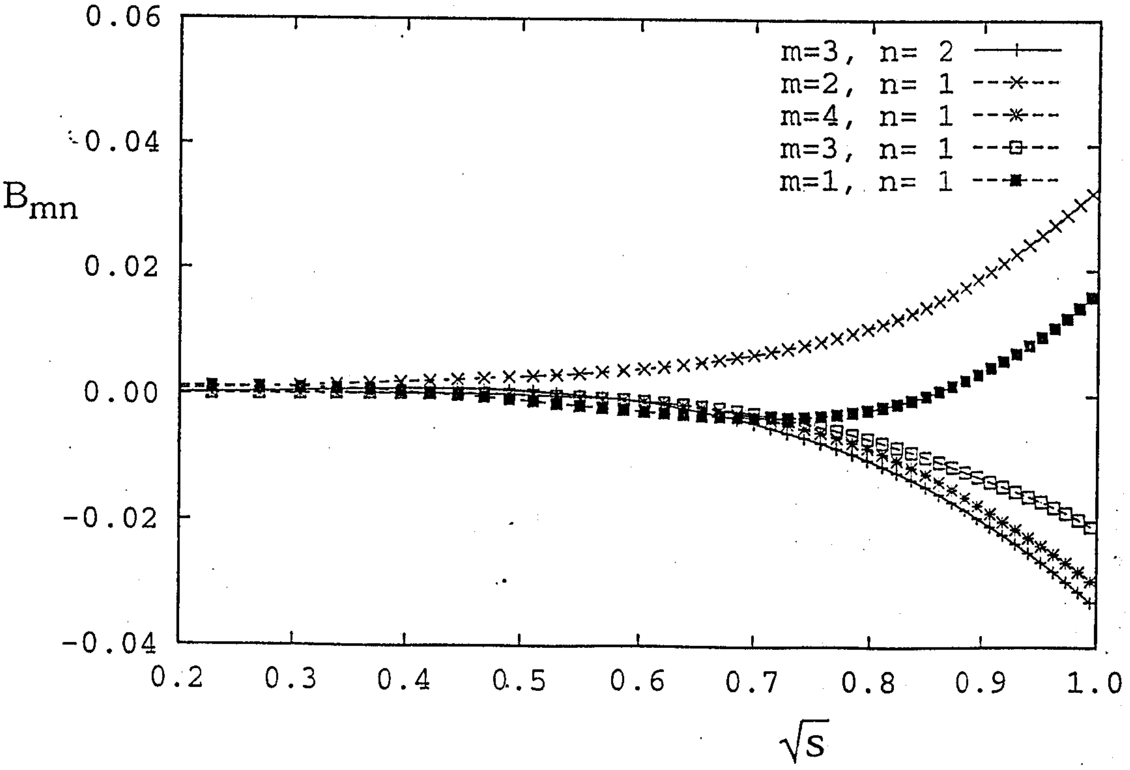

Figure 4:

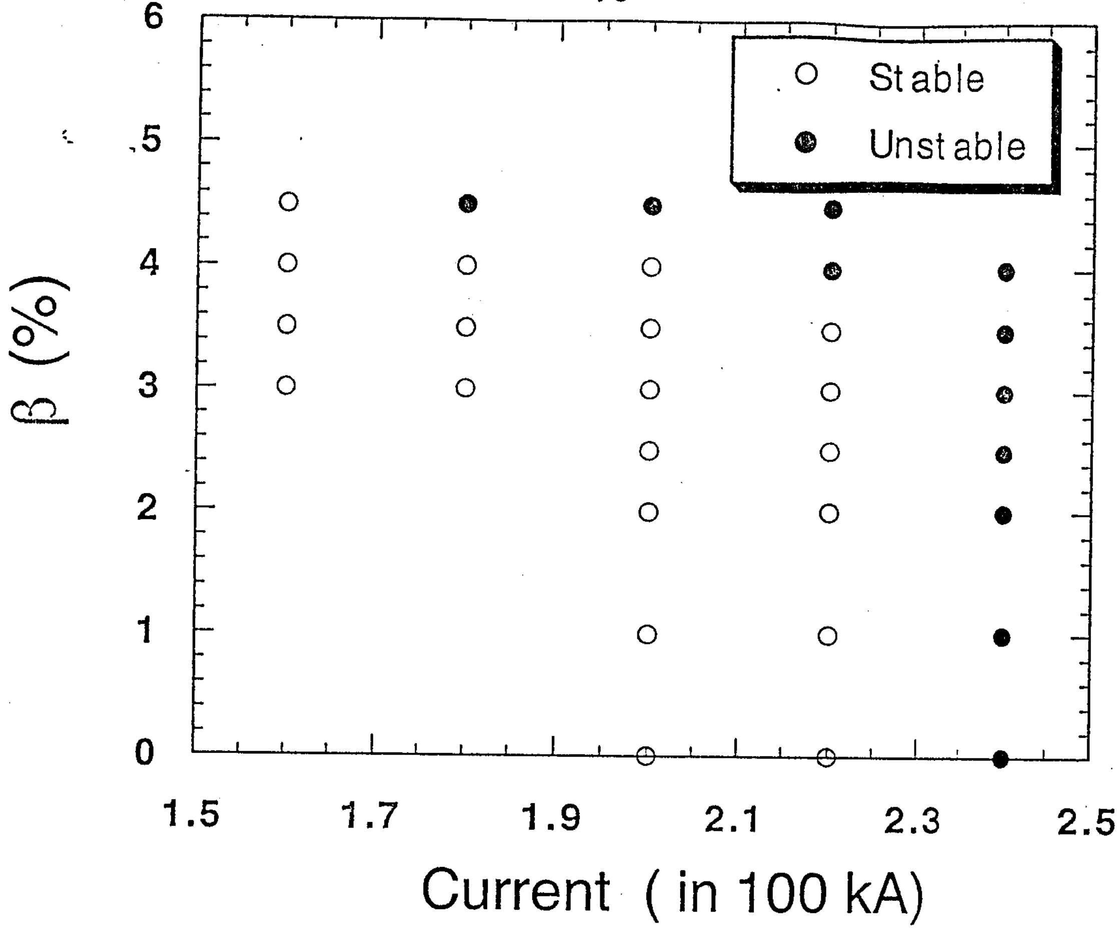

Figure 5:

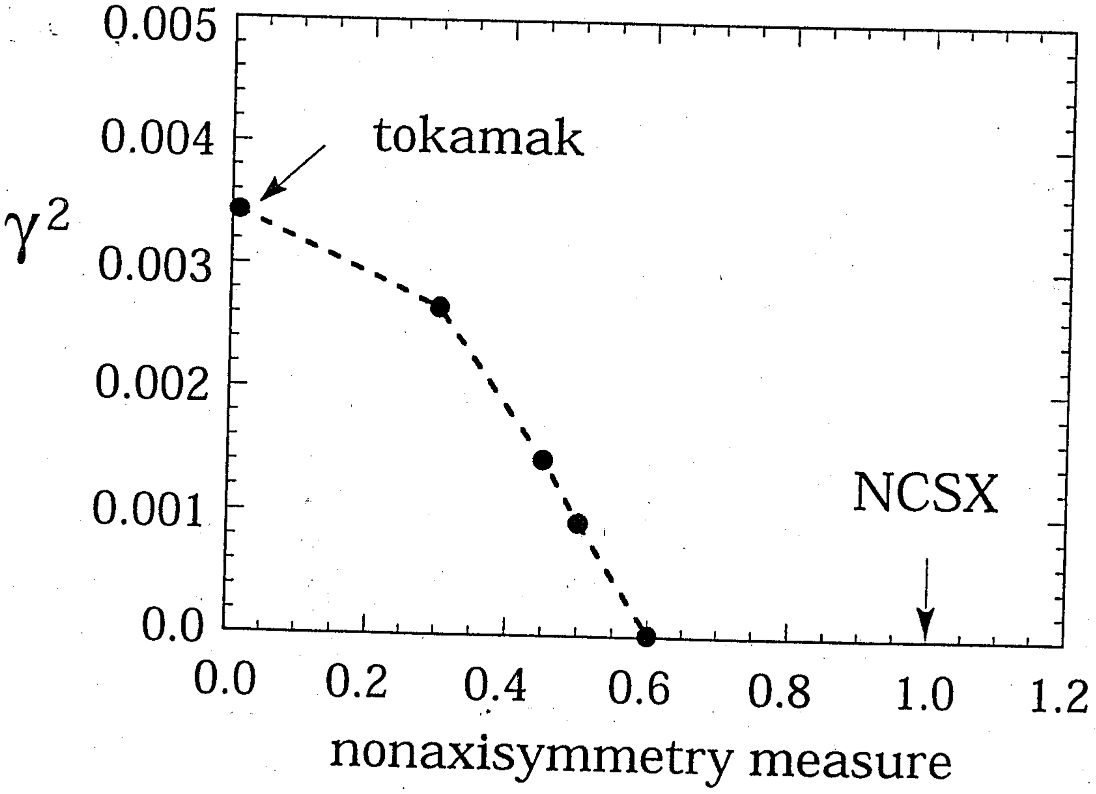

Figure 6:

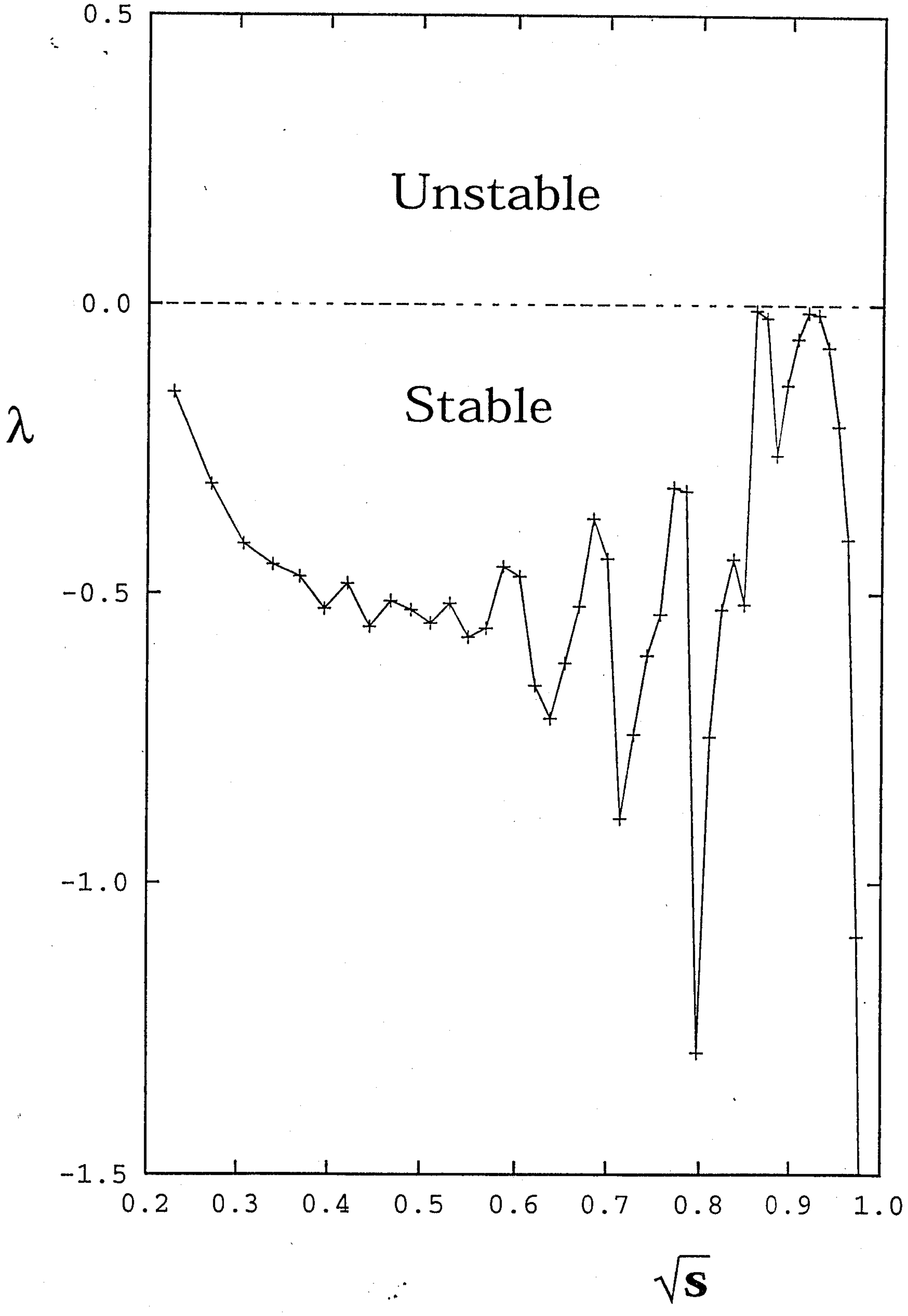

Figure 7: